The Thesis Committee for Elton Luiz Diniz Ferreira
Certifies that this is the approved version of the following thesis:

Improved Estimation of Pore Connectivity and Permeability in Deepwater Carbonates with the Construction of Multi-Layer Static and Dynamic Petrophysical Models

APPROVED BY
SUPERVISING COMMITTEE:

Supervisor:

Carlos Torres-Verdín

Steve Bryant

Improved Estimation of Pore Connectivity and Permeability in Deepwater Carbonates with the Construction of Multi-Layer Static and Dynamic Petrophysical Models

by

Elton Luiz Diniz Ferreira, B.S.P.

Thesis

Presented to the Faculty of the Graduate School of

The University of Texas at Austin

in Partial Fulfillment

of the Requirements

for the Degree of

Master of Science in Engineering

The University of Texas at Austin

May 2014

Dedication

To my lovely daughter, Helena, a blessing who arrived in our lives; the last three months of work were enlightened by her smile.

To my beloved wife, Amanda, for her love, partnership, patience, and encouragement.

To my dear parents, Celso and Bernadete, for their unconditional love, support, and guidance.

Acknowledgements

First and foremost I would like to express my profound gratitude to my supervisor, Dr. Carlos Torres-Verdín, for his support and encouragement throughout the duration of my research. In particular, his tenets guided me in providing petrophysical evaluations based on multidisciplinary principles. It has been my privilege to complete my graduate studies under his supervision. I would also like to extend my thanks to Dr. Steven Bryant for his advice and comments, which helped me to complete this thesis.

I would also like to thank Petrobras for providing the data set used in this research. Special thanks go to Carlos Francisco Beneduzi and to Paulo Sérgio Denicol for their encouragement and guidance. The work presented in this thesis would not have been possible without their continuous support. I am also grateful to Bernardo Coutinho and Ronaldo Freire for collecting and sharing some of the data used in this research.

I would like to thank the faculty of the Petroleum and Geosystems Engineering Department at The University of Texas at Austin for teaching me interesting and useful subjects. A special word of gratitude goes to staff members Ben Voss and Roger Terzian for their technical support and to Rey Casanova for his administrative support of the Formation Evaluation research group. I am also grateful to Frankie Hart for providing help and support.

Additionally, I thank my friends, colleagues, and office-mates in Petroleum and Geosystems Engineering for the memorable experiences we shared, including the many hours we spent studying together. Special thanks go to Rodolfo Victor and Sergio Cavalcante for the incredible amount of time we spent together preparing for the Ph.D.

qualification exam and for the coffee breaks we took together to brighten the difficult times.

Finally, I am immensely grateful to my family for their support and patience throughout my overseas journey. Special words of gratitude go to my wife, Amanda; my parents, Celso and Bernadete; my brother, Wellington; my parents-in-law, Valmor and Juçara; and my sisters-in law and brothers-in-law, Aline, Wellington, Bárbara, Matheus, and Camila: thank you all so much for all your love, support, prayers, and hopes for my success.

Abstract

Improved Estimation of Pore Connectivity and Permeability in Deepwater Carbonates with the Construction of Multi-Layer Static and Dynamic Petrophysical Models

Elton Luiz Diniz Ferreira, M.S.E.

The University of Texas at Austin, 2014

Supervisor: Carlos Torres-Verdín

A new method is presented here for petrophysical interpretation of heterogeneous carbonates using well logs and core data. Developing this new method was necessary because conventional evaluation methods tend to yield inaccurate predictions of pore connectivity and permeability in the studied field. Difficulties in the petrophysical evaluation of this field are related to shoulder-bed effects, presence of non-connected porosity, rock layers that are thinner than the vertical resolution of well-logging tools, and the effect of oil-base mud (OBM) invasion in the measurements. These problems give rise to uncommon measurements and rock properties, such as: (a) reservoir units contained within thinly bedded and laminated sequences, (b) very high apparent resistivity readings in the oil-bearing zone, (c) separation of apparent resistivity logs with different depths of investigation, (d) complex unimodal and bimodal transverse relaxation distributions of nuclear magnetic resonance (NMR) measurements, (e) reservoir units having total porosity of 0.02 to 0.26 and permeability between 0.001mD to 4.2D, (f)

significant differences between total and sonic porosity, and (g) low and constant gamma-ray values.

The interpretation method introduced in this thesis is based on the detection of layer boundaries and rock types from high-resolution well logs and on the estimation of layer-by-layer properties using numerical simulation of resistivity, nuclear, and NMR logs. Layer properties were iteratively adjusted until the available well logs were reproduced by numerical simulations. This method honors the reservoir geology and physics of the measurements while adjusting the layer properties; it reduces shoulder-bed effects on well logs, especially across thinly bedded and laminated sequences, thereby yielding improved estimates of interconnected porosity and permeability in rocks that have null mobile water saturation and that were invaded with OBM. Additionally, dynamic simulations of OBM invasion in free-water depth intervals were necessary to estimate permeability.

It is found that NMR transverse relaxation measurements are effective for determining rock and fluid properties but are unreliable in the accurate calculation of porosity and permeability in thinly bedded and highly laminated depth sections. In addition, this thesis shows that low resistivity values are associated with the presence of microporosity, and high resistivity values are associated with the presence of interconnected and vuggy porosity. In some layers, a fraction of the vuggy porosity is associated with isolated pores, which does not contribute to fluid flow. An integrated evaluation using multiple measurements, including sonic logs, is therefore necessary to detect isolated porosity. After the correction and simulation, results show, on average, a 34% improvement between estimated and core-measured permeability. Closer agreement was not possible because of limitations in tool resolution and difficulty in obtaining a precise depth match between core and well-log measurements.

Table of Contents

List of Tables

List of Figures

Figure 5.1: Results of static simulations in Well **H** across the oil-bearing zone. The well was drilled with OBM. Dashed curves identify numerical simulations. Track 1: gamma-ray log (green), caliper log (blue), and simulated gamma-ray log (dashed red). Track 2: depth. Track 3: apparent resistivities acquired with different depths of investigation (red and blue), and simulated apparent resistivities with different depths of investigation (dashed dark red and dashed dark blue). Track 4: density (red), neutron porosity in sandstone units (green), PEF (purple), compressional slowness (teal), simulated density (dashed dark red), and simulated neutron porosity in sandstone units (dashed purple). Track 5: computed total porosity from mineral inversion (blue), computed sonic (Wyllie) porosity (orange), core porosity (green and red dots), and interconnected porosity used in the numerical simulations (purple). Track 6: total water saturation computed from Archie's equation (blue), irreducible water saturation used in the numerical simulations (green), total water saturation used in the numerical simulations (purple), and petrophysical bed boundaries (red). Track 7: core permeability (black and red dots), and estimated permeability from Timur-Tixier's equation using earth model results (purple). Track 8: NMR *T2* distribution. .35

Figure 6.2: Results of dynamic simulations in Well **X** across a short depth section fully saturated with water. The well was drilled with OBM. Measurements were acquired after 9 days of OBM invading the formation. Dashed curves identify numerical simulations. Track 1: gamma-ray of the intermediate phase (green) and gamma-ray of the final phase (blue). Track 2: depth. Track 3: apparent resistivities with different depths of investigation (red, blue, aqua, dark blue and black), and simulated apparent resistivities (dashed red, dashed blue, dashed aqua, dashed dark blue and dashed black). Track 4: density (red), neutron porosity in sandstone units (green), sonic (light pink), PEF (purple), simulated density (dashed red), and simulated neutron porosity in sandstone units (dashed dark green). Track 5: computed sonic (Wyllie) porosity (red), porosity and porosity fractions estimated with NMR *T2* distributions (light blue, olive, and brown), interconnected porosity used in the simulations (blue), and core porosity (black dots). Track 6: NMR *T2* distributions. Track 7: numerical simulations of NMR *T2* distributions. Track 8: radial distribution of electrical resistivity from the simulations of mud-filtrate invasion. Track 9: core permeability (black dots), permeability used to perform dynamic simulations (blue), permeability estimated with Timur-Tixier's equation (dashed red), and permeability estimated with Timur-Coates' equation (dashed purple).61

Chapter 1: Introduction

Most of the proven hydrocarbon reserves worldwide are in carbonate reservoirs. Formation evaluation of carbonate fields is challenging due to both large spatial heterogeneity and complex pore structure. Due to the complexity of the evaluated reservoir rocks, conventional well log interpretations incorrectly estimate porosity, water saturation, and permeability. This thesis focuses on an advanced petrophysical evaluation method, based on the reduction of shoulder-bed effects, on the physical interpretation of mud-filtrate-invasion, and on the layer-by-layer estimation of interconnected porosity, irreducible water saturation, and permeability. The approach provides improved estimations of petrophysical properties of the evaluated deepwater carbonate formations located in the Santos Basin, offshore of Brazil.

1.1 Reservoir Geology

The hydrocarbon reservoir under consideration consists of a lacustrine rift-sag carbonate setting (Wright, 2012). It originated from rift phase between South America and Africa, which started in the Hauterivian and continued until the beginning of the Aptian age. The sag phase (post-rift) of the Santos Basin corresponds to the Aptian age and comprises the reservoir evaluated in this thesis (Moreira *et al*., 2007). Due to the fact that the basin was formed in a divergent boundary, the studied reservoir does not contain complex tectonic features.

The main facies of the sedimentary sequence are composed of microbiolites, stromatolites, and laminites formed in a hypersaline lacustrine/restricted-lagoonal environment (Wright, 2012). Dunham (1962) classified these facies as boundstone, which is a limestone deposit that was originally bound by algae, bacteria, or other unicellular

organisms. The binding process generated growth-framework porosity, where the rigid skeleton constructed by the microorganisms during the binding process provides mechanical support to large pores (**Figure 1.1c**). Grainstone, packstone, and mudstone also occur in this sequence. Such facies are associated with sedimentary depositional processes; the primary porosity of these layers tends to be intergranular. Subsequent geologic events, such as dolomitization and differential dissolution, gave rise to rocks exhibiting a highly complex and heterogeneous pore topology. Dissolution is also responsible for the presence of large pores. Many depth sections of the reservoir consist of thinly bedded and highly laminated sequences that are difficult, if not impossible, to interpret with conventional well logs.

1.2 Problem Statement and Method of Evaluation

Estimating petrophysical properties of carbonate sedimentary sequences has been a challenge for many years. Chombart (1960) noted that carbonates reservoirs exhibit significant variations in pore structure, pore size distribution, and fluid content, within very short distances and in any direction. The large spatial heterogeneity produces shoulder-bed effects on well-logs measurements. Biehle and Crocker (1987) proposed the use of cross plots in carbonate reservoir evaluation. These authors used Pickett plots to determine Archie's porosity exponent (m) and multivariable cluster analysis to group porosity types. Aguilera (2004) pointed out that the straight line in the Pickett plot is related to the porosity exponent (m), the water saturation exponent (n), and the size of the particles forming the interparticle porosity. The adjustment of Archie's exponents (m and n) necessary to improve the estimates of petrophysical properties is common in the petrophysical evaluation of carbonate fields. Olesen *et al.* (2000) cautioned that over-optimistic hydrocarbon saturation estimation may occur unless the porosity exponent (m)

is appropriately adjusted to account for secondary porosity. Better results have been obtained with the integration of different logs in carbonate reservoir interpretation. Olesen *et al.* (2000) used an integrated interpretation of NMR, and sonic logs, and pressure pre-tests to estimate permeability, hydrocarbon saturation, and irreducible water saturation. Babadagli and Al-Salmi (2002) also used NMR measurements to improve permeability estimations, mainly in mudstone and grainstone units.

One of the most important steps in carbonate reservoir evaluation is the classification of reservoir units into rock types. Lucia (2007) stated that the pore space must be defined and classified in terms of rock fabrics and petrophysical properties in order to integrate geological and engineering information. The first attempt to relate rock fabrics to petrophysical rock properties in carbonate rocks was made by Archie (1952). The Archie method is difficult to use because rock descriptions cannot be defined in depositional or diagenetic terms. In 1999, Lucia (1999) proposed a division of pore types that differentiates interparticle and vuggy porosity. Vuggy porosity was also subdivided into separate and touching vugs. Presence of vuggy porosity alters the manner in which the pore space is connected. According to Lucia (2007) characterizing the pore system is difficult in touching-vug reservoirs, because the system is not related to a precursor depositional fabric, it is usually wholly diagenetic in nature. The classification and interpretation of micro, interparticle, touching, and isolated vuggy porosity was one of the principal obstacles in the petrophysical evaluation of the studied carbonate reservoir in this thesis.

Because of the complexity of the pore space, the high spatial heterogeneity of the rocks under consideration, and the presence of vuggy porosity, petrophysical properties estimated using conventional well-log evaluation methods rarely reproduce core laboratory measurements (**Figures 2.1** and **2.2)**. Additionally, presence of laminations

and fluid flow units thinner than the vertical resolution of the available well logs is common in the reservoir under consideration (**Figure 1.2**). To improve petrophysical estimations, a new rock typing method was developed, which correlates well-log signatures with geological information. The new rock typing method was applied and an earth model was constructed using the predominant type of porosity in each layer. This rock type model considers three principal types of porosity: intergranular porosity, microporosity, and vuggy porosity; where the last type was further subdivided into touching-vug and isolated-vug porosity. Non-connected porosity does not contribute to fluid flow, hence, this type of porosity should not be included in permeability estimations. Rock typing was used to construct multi-layer petrophysical models that account for shoulder-bed effects and for mud filtrate invasion on well logs. Using a geologically consistent earth model, we performed static and dynamic well-log simulations to match the available resistivity, nuclear, and NMR logs.

In this thesis, we evaluated three wells, referred to as Wells **H**, **Γ,** and **X.** The studied sections of these wells were drilled with OBM. **Figure 1.3** is an overview of the evaluated wells. The evaluated intervals of Wells **H** and **Γ** are in the upper sections of the reservoir which exhibit no mobile water saturation. In contrast, the evaluated interval of Well **X** is fully saturated with water. The interval in Well **X** was chosen to analyze the process of OBM invasion into the formation. Petrophysical property estimations made using this new method were superior to those obtained with conventional interpretation methods.

1.3 Outline of the Thesis

Chapter 2 of this thesis describes the conventional petrophysical evaluation performed in the studied wells and compares conventional petrophysical estimations to

core data. Chapter 3 discusses conventional rock typing methods applied to the data and explains in detail the rock typing method developed for this field. Chapter 4 describes the construction of the earth model and the static and dynamic simulations that were conducted to numerically reproduce the available well logs. Examples of the new evaluation method and a discussion of results are presented in Chapters 5 and 6. Chapter 5 describes the application of the new method in the oil-bearing zone of the reservoir and Chapter 6 describes the application of the method in the free-water level. Finally, Chapter 7 summarizes the conclusions of the thesis, pointing out the advantages obtained when using the described method, and emphasizing its limitations; recommendations are also made for future research.

Figure 1.1: Examples of rocks formed from stromatolites. (a) Stromatolite fossil from upper Precambrian rocks in Montana; the cut slab is a cross section perpendicular to the original water surface. Flat layers are fossilized microbial mats, whereas curved layers are fossilized mounds analogous to those living today in Shark Bay (http://www.lpi.usra.edu/education/EPO/yellowstone2002/workshop/stromatolite/index.html). (b) 3D view of microbial mat mounds (Museum of the Rockies) modeled after the microbial mounds in Shark Bay, Australia (http://www.lpi.usra.edu/education/EPO/yellowstone2002/workshop/stromatolite/index.html). (c) Cross section of the type of rock present in the field of study. (d) Outcrop showing some impressively large domal stromatolites.

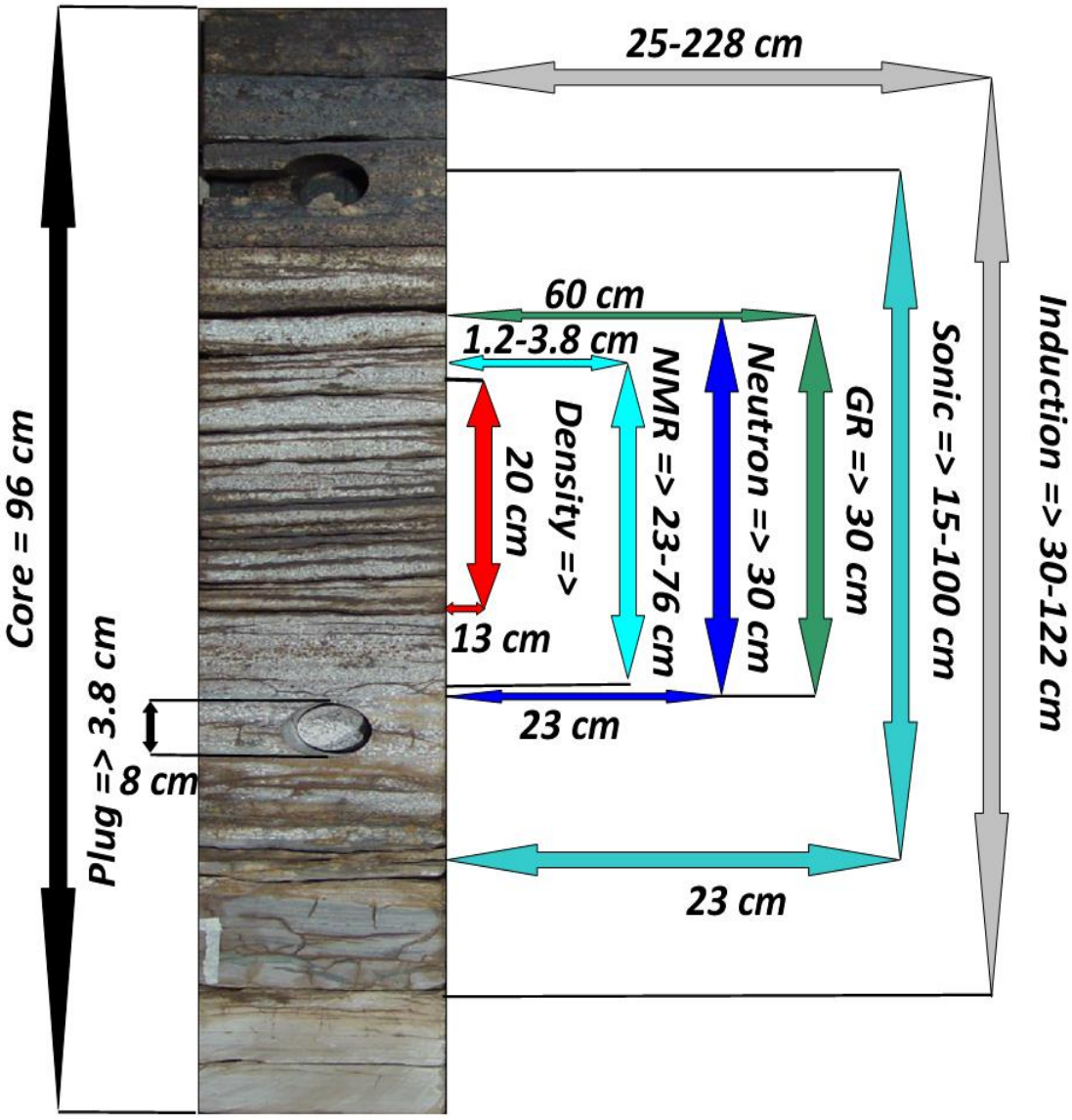

Figure 1.2: Comparison of vertical resolution (vertical arrows) and radial depth of investigation (horizontal arrows) of whole core, core, plugs, and well logs. Photograph of a core segment retrieved from a laminated zone in the reservoir under analysis. The numbers associated with each arrow represent approximate values of vertical or radial resolution. None of the available well logs have enough vertical resolution to detect and resolve the thin laminations present in this core.

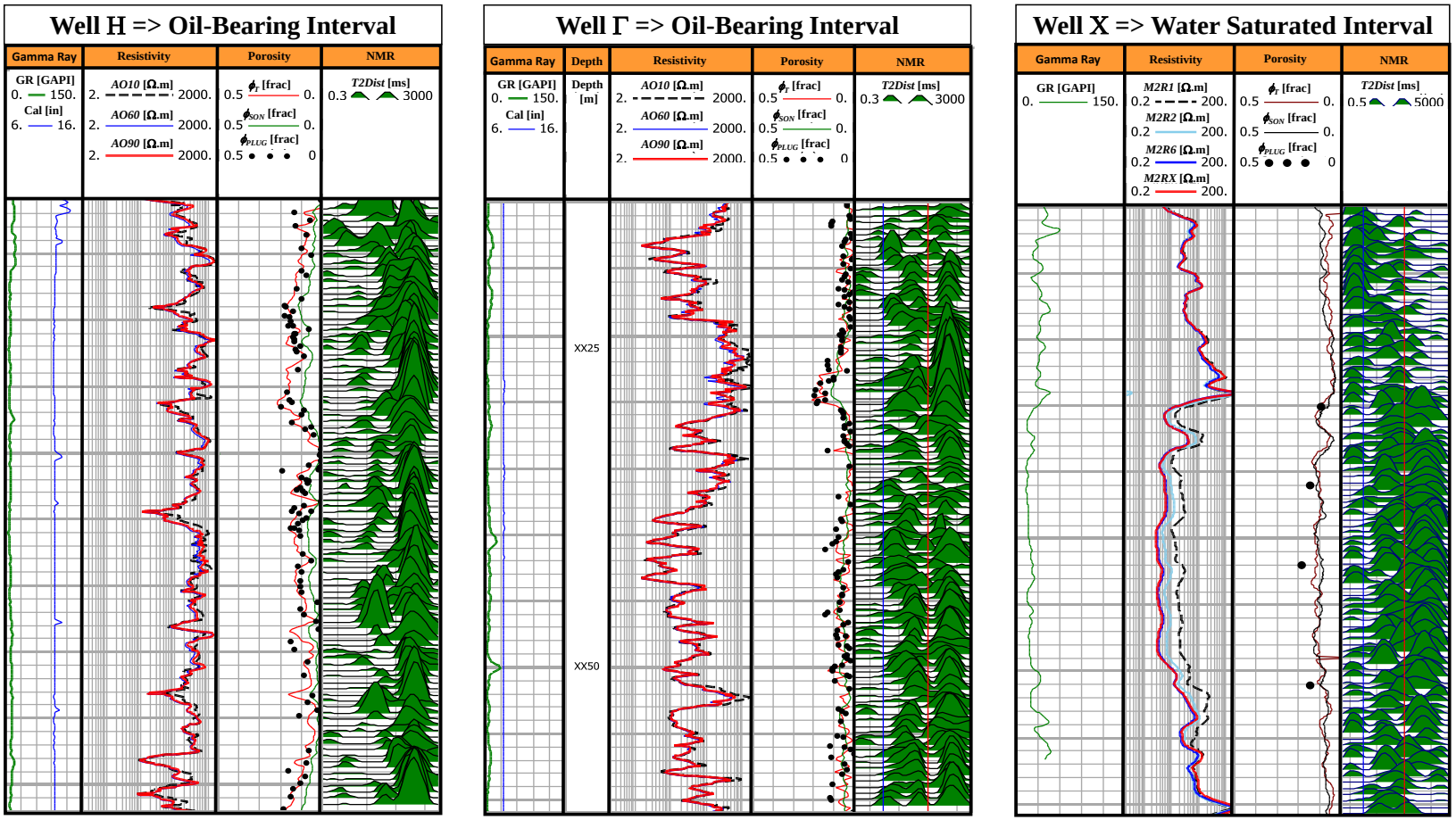

Figure 1.3: Comparison of the three evaluated wells. Track 1: caliper and gamma-ray logs. Track 2: apparent resistivities with different depths of investigation. Track 3: computed total porosity using mineral inversion, computed sonic (Wyllie) porosity, and core porosity. Track 4: NMR *T2* distribution.

Chapter 2: Well-Log Analysis and Conventional Interpretation

This chapter analyzes the well logs from the area of study and discusses their initial physical/geological interpretation. Next follows an extensive discussion of the conventional well log evaluation method for this complex field and the conventional estimations of porosity, water saturation, and permeability. Finally, it is shown that petrophysical estimations obtained with the standard approach are not supported by core data because of the geologic complexity of the carbonates formations involved.

2.1 Conventional Evaluation Method and Well-Log Analysis

Figure 2.1 shows the complete set of available well logs, the core measurements, and the results obtained from conventional petrophysical interpretation across the oil-bearing zone in Well **Γ**; this section of the well was drilled with OBM. In track 1, a constant caliper of 8.5 inches was measured, which corresponds to the nominal diameter of the well, indicating no washouts or excessive mudcake. A similar behavior was observed in the remaining evaluated wells.

The gamma-ray log (GR) in **Figure 2.1**, track 1, shows relatively low and constant values. Volumetric concentration of clay tends to be low in most of the layers; thus, zones of high GR are generally associated with organic matter. Consequently, the GR log is not the best option to classify rock types or to establish correlations across different wells (**Figure 1.3**).

Abnormally high resistivity readings were observed in the oil-bearing zone (**Figure 2.1**, track 3). Resistivity values in this zone range between 100 to 2000 Ω.m. Apparent resistivity logs also exhibit separation between logs with different depths of investigation. The separation is due either to shoulder-bed effects or to limits in the vertical resolution of the induction tools.

Density and neutron logs exhibit a positive correlation (**Figure 2.1**, track 4), generating similar values of calculated porosity due to the slight presence of clay in this formation. Total porosity calculated from these logs ranges from 0.02 to 0.26 and photoelectric factor (PEF) values range between 2.5 and 4.5 b/e-, which coincide with nominal values of limestone and dolomite matrix. By default, at Petrobras, neutron logs are expressed in sandstone porosity units. All measured and simulated neutron logs in this thesis are also expressed in sandstone porosity units.

Sonic porosity was computed using Wyllie´s equation (Wyllie *et al.*, 1956) and depicted in **Figure 2.1**, track 5. Input parameters in this equation were carefully selected: the slowness of the matrix was calculated from the mineral composition determined with mineral inversion using basic well logs, and the slowness of the fluid was calculated based on Archie's water saturation component (Sw_{Archie}). Sonic porosity is consistently lower than total porosity calculated using NMR and density-neutron logs. The difference between sonic and total porosity is associated here with presence of vuggy porosity.

The NMR *T2* distribution (**Figure 2.1**, track 8) in this reservoir is complex, exhibiting variable unimodal and bimodal responses. This behavior results from the complexity of the pore space. The effect of mud filtrate on NMR measurements can cause misleading *T2* distribution interpretations, chiefly in OBM-drilled wells. Presence of laminated rocks or thinly bedded fluid-flow units also interferes with NMR measurements, as the NMR tool has a relatively low vertical resolution. The mixing effect associated with NMR measurement will be discussed in Appendix B. Total porosity obtained from NMR measurements is similar to that calculated using neutron and density logs.

Water saturation (*Sw*) was calculated from both NMR *T2* distributions (Sw_{NMR}) and Archie's equation (Sw_{Archie}). Results are shown in **Figure 2.1**, track 6; Sw_{Archie} values

show larger variations than do Sw_{NMR} values, due to the relatively high vertical resolution of density porosity used as total porosity in that equation. The parameters used in Archie´s equation are similar to those measured by laboratory core analysis (**Table 2.1**).

Archie parameters	Value
a	1
m	2.15
n	2.3

Table 2.1: Archie's parameters used to calculate water saturation in this study.

Linear mineral inversion was then used to estimate the mineral composition of the formation (**Figure 2.1**, track 9). The inversion was performed with gamma-ray, resistivity, density, neutron, and PEF logs, along with the mass balance equation. Results obtained from this estimation agree with laboratory measurements in wells where x-Ray diffraction (XRD) data were available. In addition, water saturation values obtained from inversion were in agreement with results calculated using Archie's equation.

Porosity values calculated using nuclear or NMR logs showed a good agreement with core total porosity (**Figure 2.1**, track 5). In contrast, permeability values calculated with either Timur-Tixier (Timur, 1969) or Timur-Coats (Coats *et al.*, 1991) equations did not accurately reproduce core measurements (**Figure 2.1**, track 7). Conventional petrophysical evaluation methods are inaccurate when calculating permeability because of the complex pore space and spatial heterogeneity of the reservoir under consideration. **Figures 2.2** and **2.3** show a similar conventional evaluation performed in Wells **H** and **X**, respectively. Well logging occurred at different time intervals in Well **X**; well logs were collected after 1 day and 15 days of OBM invasion, respectively. **Figure 2.3** shows both

measurements. The next chapters describe how the procedures developed in this thesis were used to integrate rock information, core measurements, and well logs to obtain a reliable evaluation of pore connectivity and permeability.

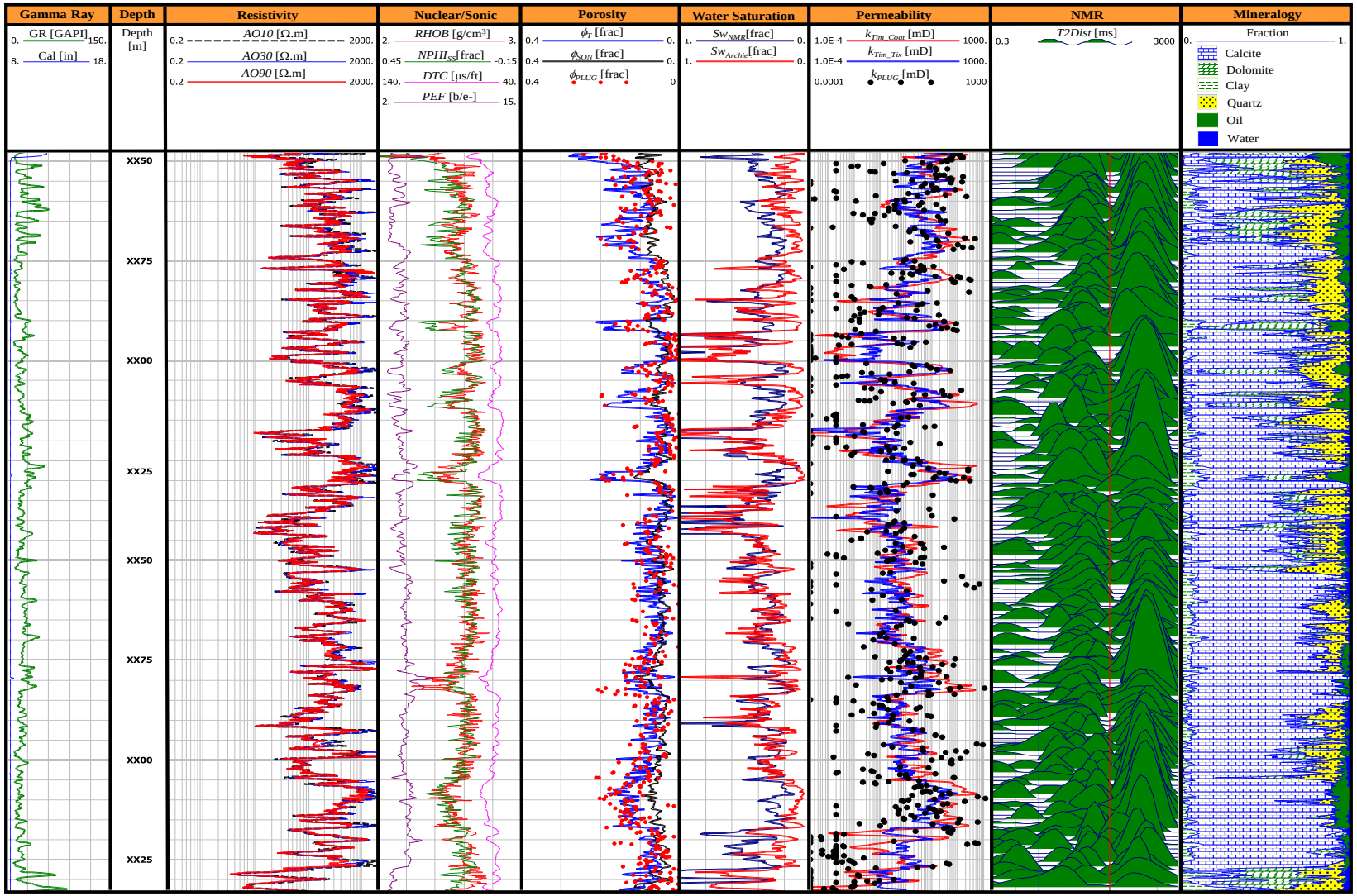
Gamma Ray
Depth
Resistivity
Nuclear/Sonic
Porosity
Water Saturation
Permeability
NMR
Mineralogy
GR [GAPI]
0.
150.
Cal [in]
8.
18.
Depth [m]
AO10 [Ω.m]
AO30 [Ω.m]
AO90 [Ω.m]
0.2
2000.
RHOB [g/cm³]
2.
3.
NPHISS[frac]
0.45
-0.15
DTC [µs/ft]
140.
40.
PEF [b/e-]
2.
15.
ϕT [frac]
ϕSON [frac]
ϕPLUG [frac]
0.4
0.
0
SwNMR[frac]
SwArchie[frac]
1.
0.
k Tim_Coat [mD]
k Tim_Tix [mD]
k PLUG [mD]
1.0E-4
1000.
0.0001
1000
T2Dist [ms]
0.3
3000
Fraction
1.
Calcite
Dolomite
Clay
Quartz
Oil
Water
XX50
XX75
XX00
XX25
XX50
XX75
XX00
XX25

Figure 2.1: Conventional petrophysical interpretation in Well **Γ** across the oil-bearing zone. The well was drilled with OBM. Track 1: caliper (blue) and gamma-ray (green) logs. Track 2: depth. Track 3: apparent resistivities with different depths of investigation. Track 4: neutron porosity in sandstone units (green), density (red), PEF (purple) and sonic logs (fuchsia). Track 5: computed total porosity using mineral inversion (blue), computed sonic (Wyllie) porosity (black) and core porosity (red dots). Track 6: total water saturation computed with Archie's equation (red) and total water saturation computed with the NMR log (blue). Track 7: permeability computed with the Timur-Coats equation (red), permeability computed with the Timur-Tixier equation (blue), and core permeability (black dots). Track 8: NMR *T2* distribution. Track 9: estimated mineralogy using linear inversion.

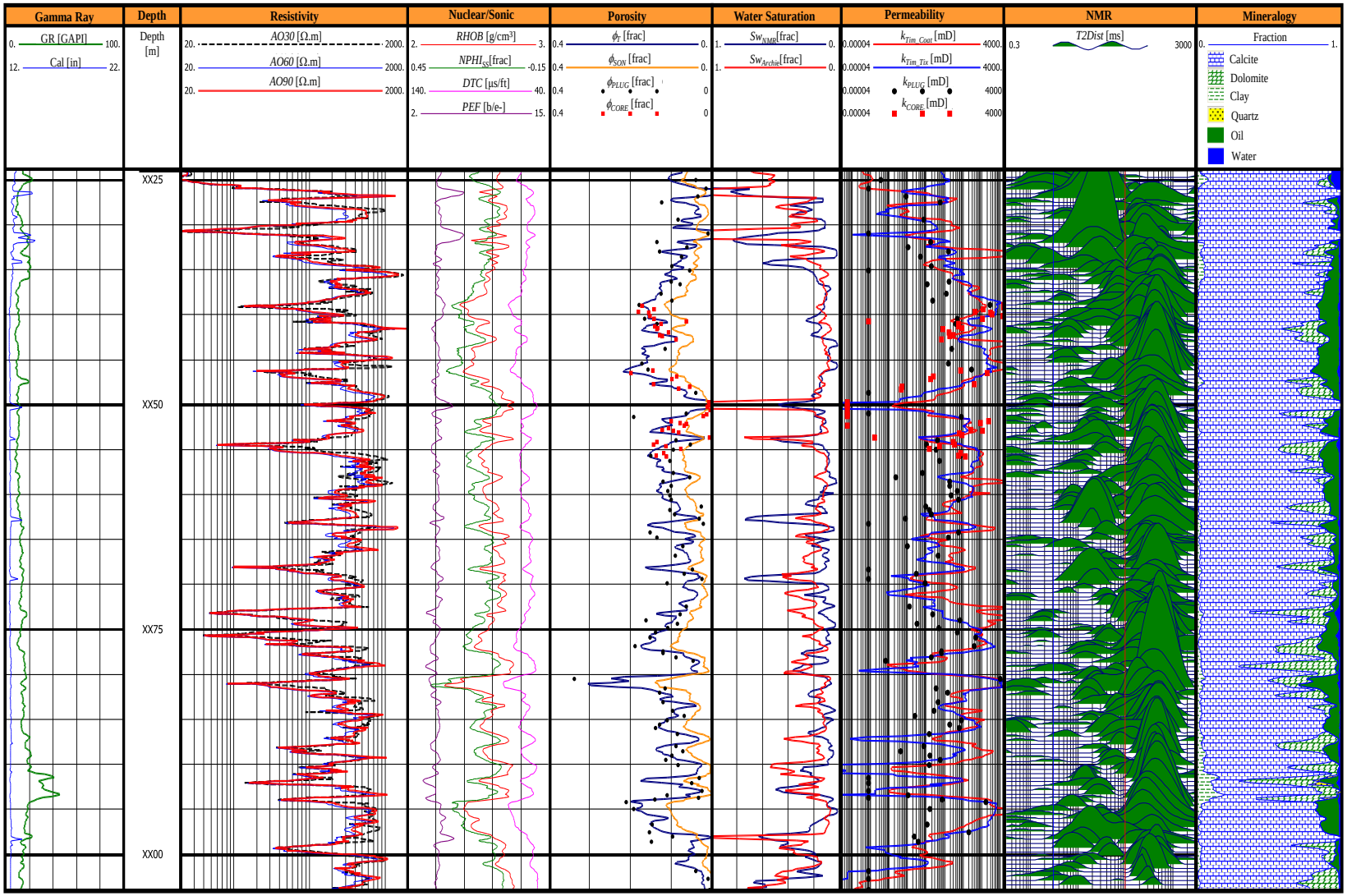
Gamma Ray
GR [GAPI]
0.
100.
Cal [in]
12.
22.
Depth
Depth [m]
XX25
XX50
XX75
XX00
Resistivity
AO30 [Ω.m]
AO60 [Ω.m]
AO90 [Ω.m]
20.
2000.
Nuclear/Sonic
RHOB [g/cm³]
2.
3.
NPHI_SS [frac]
0.45
-0.15
DTC [µs/ft]
140.
40.
PEF [b/e-]
2.
15.
Porosity
φ_T [frac]
φ_SON [frac]
φ_PLUG [frac]
φ_CORE [frac]
0.4
0.
0
Water Saturation
Sw_NMR [frac]
Sw_Archie [frac]
1.
0.
Permeability
k_Tim_Coat [mD]
k_Tim_Tix [mD]
k_PLUG [mD]
k_CORE [mD]
0.00004
4000.
4000
NMR
T2Dist [ms]
0.3
3000
Mineralogy
Fraction
0.
1.
Calcite
Dolomite
Clay
Quartz
Oil
Water

Figure 2.2: Conventional petrophysical interpretation in Well **H** across the oil-bearing zone. The well was drilled with OBM. Track 1: caliper (blue) and gamma-ray (green) logs. Track 2: depth. Track 3: apparent resistivities with different depths of investigation. Track 4: neutron porosity in sandstone units (green), density (red), PEF (purple) and sonic logs (fuchsia). Track 5: computed total porosity using mineral inversion (blue), computed sonic (Wyllie) porosity (orange) and core porosity (red and black dots). Track 6: total water saturation computed with Archie's equation (red) and total water saturation computed with the NMR log (blue). Track 7: permeability computed with the Timur-Coats equation (red), permeability computed with the Timur-Tixier equation (blue), and core permeability (red dots). Track 8: NMR *T2* distribution. Track 9: estimated mineralogy using linear inversion.

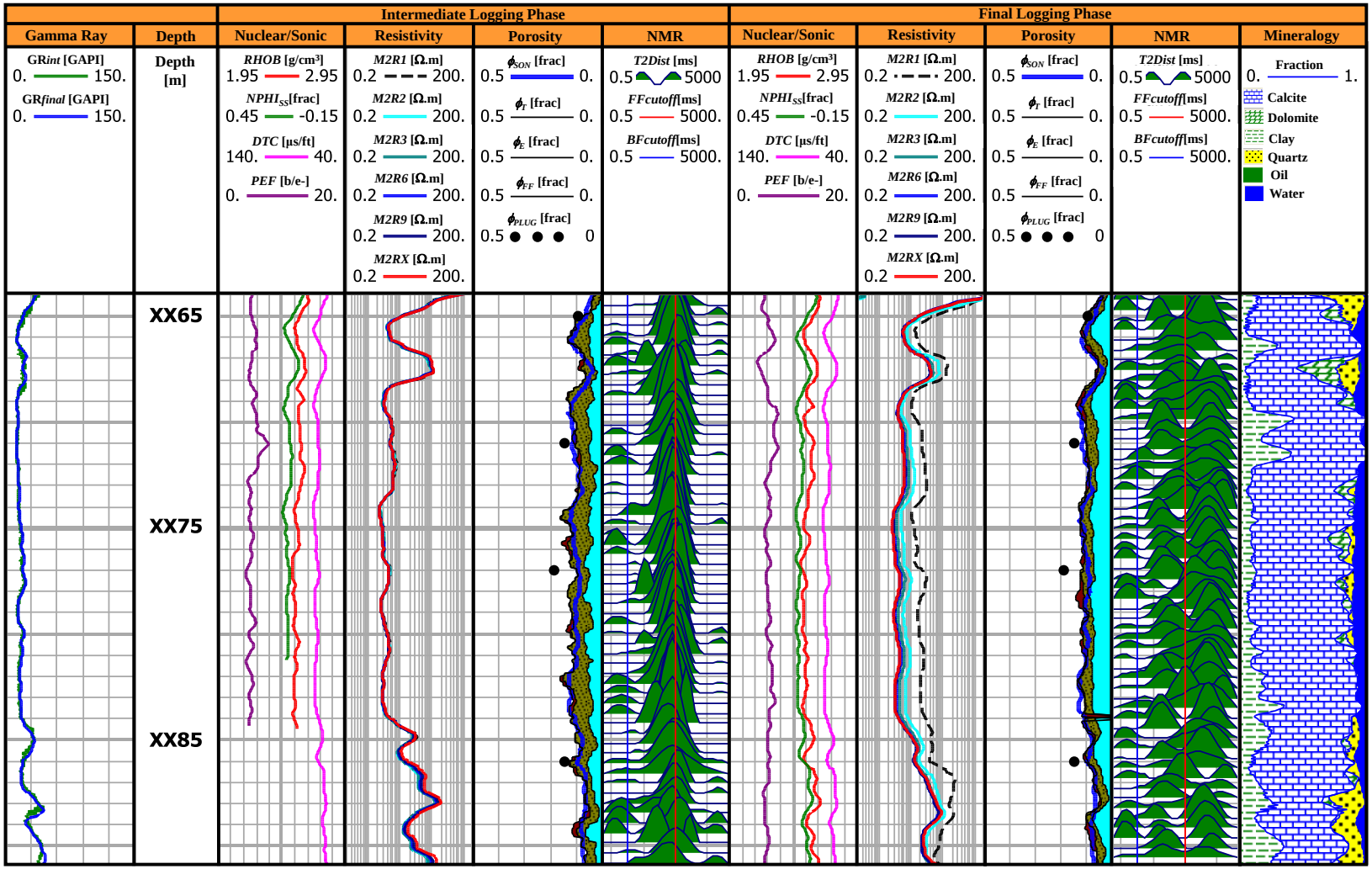
Intermediate Logging Phase
Final Logging Phase
Gamma Ray
Depth
Nuclear/Sonic
Resistivity
Porosity
NMR
Mineralogy
GRint [GAPI]
0. 150.
GRfinal [GAPI]
0. 150.
Depth [m]
RHOB [g/cm³]
1.95 2.95
NPHISS[frac]
0.45 -0.15
DTC [µs/ft]
140. 40.
PEF [b/e-]
0. 20.
M2R1 [Ω.m]
0.2 200.
M2R2 [Ω.m]
0.2 200.
M2R3 [Ω.m]
0.2 200.
M2R6 [Ω.m]
0.2 200.
M2R9 [Ω.m]
0.2 200.
M2RX [Ω.m]
0.2 200.
ϕSON [frac]
0.5 0.
ϕT [frac]
0.5 0.
ϕE [frac]
0.5 0.
ϕFF [frac]
0.5 0.
ϕPLUG [frac]
0.5 0
T2Dist [ms]
0.5 5000
FFcutoff[ms]
0.5 5000.
BFcutoff[ms]
0.5 5000.
Fraction
0. 1.
Calcite
Dolomite
Clay
Quartz
Oil
Water
XX65
XX75
XX85

Figure 2.3: Conventional petrophysical interpretation in Well **X** across the free water level with two measurements acquired at different times. The well was drilled with OBM. Tracks 3, 4, 5, and 6 are measurements and interpretations of the first logging run. Tracks 7, 8, 9, 10, and 11 are measurements and interpretations of the second logging run. Track 1: gamma-ray of the intermediate phase (green) and gamma-ray of the final phase (blue). Track 2: depth. Track 3: neutron porosity in sandstone units (green), density (red), PEF (purple) and sonic logs (fuchsia). Track 4: apparent resistivities with different depths of investigation. Track 5: computed sonic (Wyllie) porosity (blue), porosity and porosities proportions estimated with the NMR *T2* distribution (light blue, olive, and brown) and core porosity (black dots). Track 6: NMR *T2* distribution. Track 7: neutron porosity in sandstone units (green), density (red), PEF (purple) and sonic logs (fuchsia). Track 8: apparent resistivities with different depths of investigation. Track 9: sonic (Wyllie) porosity (blue), porosity and porosities proportions estimated with the NMR *T2* distribution (light blue, olive, and brown) and core porosity (black dots). Track 10: NMR *T2* distribution. Track 11: estimated mineralogy using linear inversion.

Chapter 3: Rock Typing

One of the first steps in well-log interpretation consists of determining rock types. Archie (1952) made the first attempt to correlate rock types with petrophysical rock properties in carbonate reservoirs. This step is important because of the high degree of spatial heterogeneity in the studied reservoir. Various rock types with different petrophysical properties exist in the reservoir and, consequently, provide very diverse well-log signatures. The petrophysicist should be able to identify well-log signatures, correlate them with fluid-flow units and analyze them separately. It is important to understand that petrophysical rock typing may not be equivalent to geological or geophysical rock typing; petrophysicists are interested in the porosity-permeability behavior of the reservoir, as an indicator of reservoir storage capacity and productivity.

3.1 Conventional Rock Classifications

Several techniques for rock classification were used in this research, including cluster analysis and rock classification methods by Lucia (1999), Amafule (Amafule *et al*., 1993), Winland (Pittman, 1992), Leverett (1941), and Timur-Tixier's (Timur, 1969). **Figures 3.1, 3.2, and 3.3** show attempts to apply diverse rock classification methods in Wells **H** and **Γ**. Results obtained from these classification methods were unsatisfactory due to the heterogeneity of the reservoir and presence of vuggy porosity in some layers.

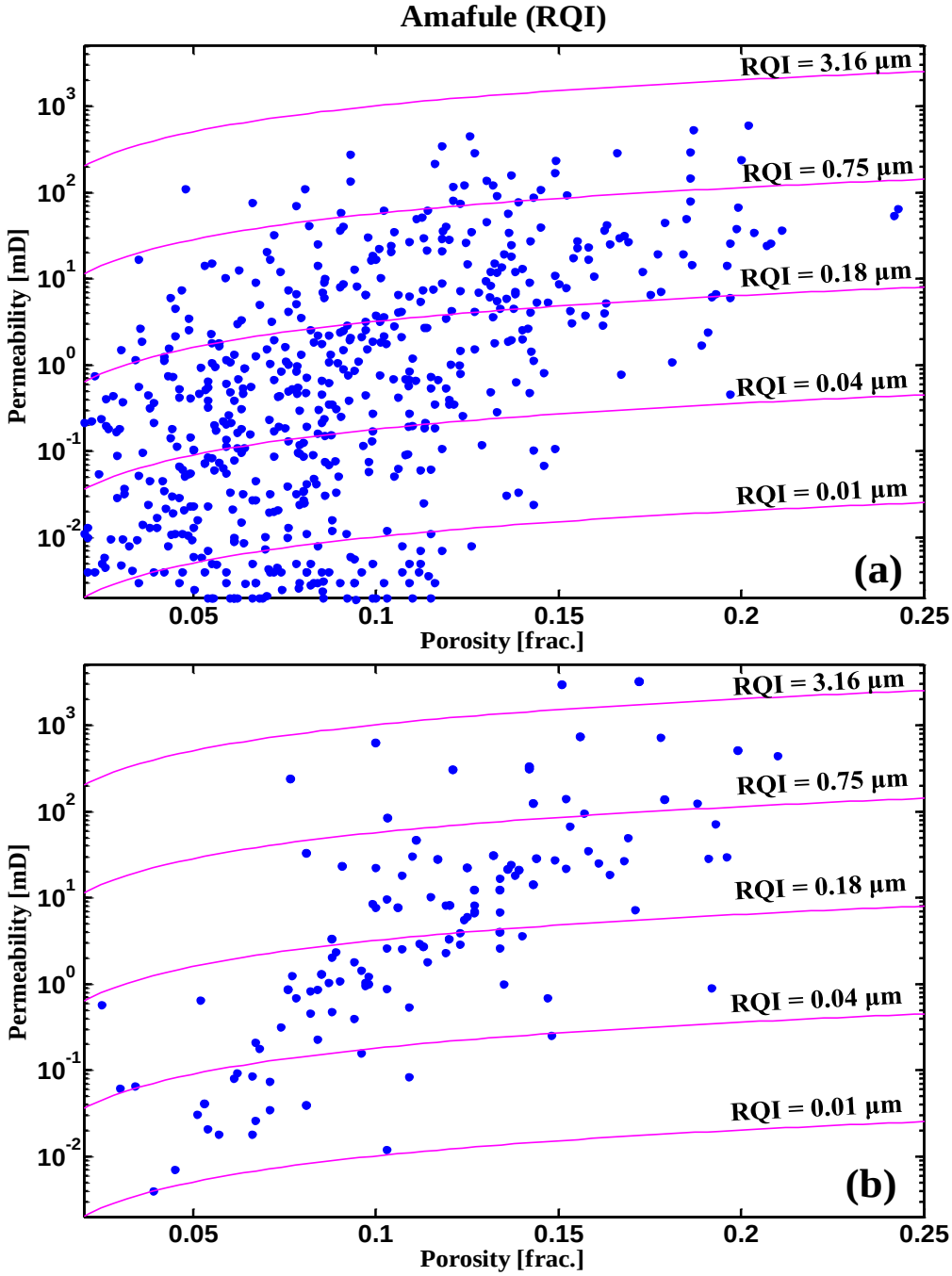

Figure 3.1: Cross-plot of total porosity and permeability used to diagnose and classify rock types using Amafule's method (Amafule *et al*., 1993) in the oil-bearing zone of (a) Well **Γ** and (b) Well **H**. Blue dots identify laboratory core measurements. Magenta continuous lines describe points with equal value of Amafule's RQI (reservoir quality index).

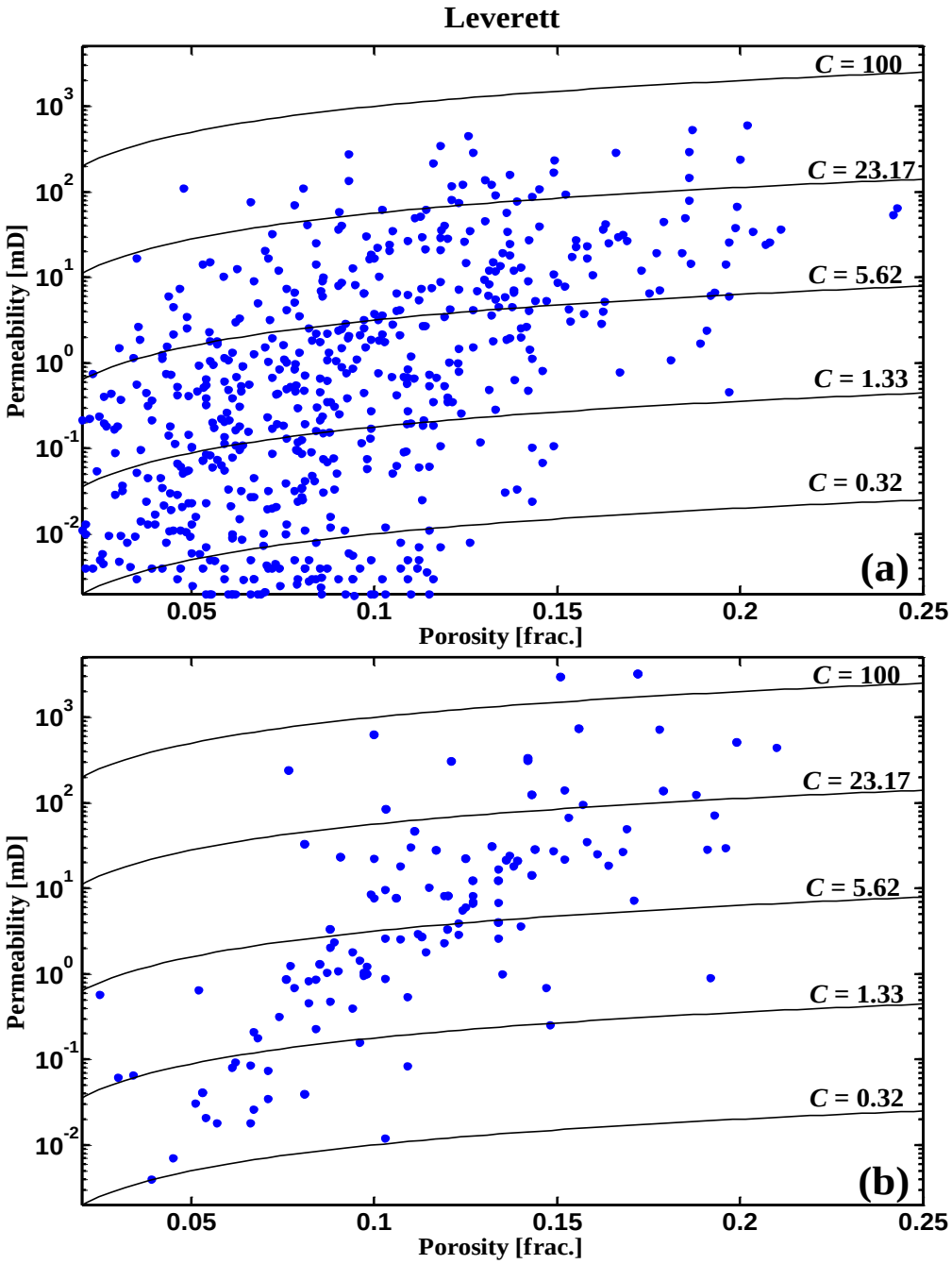

Figure 3.2: Cross-plot of total porosity and permeability used to diagnose and classify rock types using Leverett's method (Leverett, 1941) in the oil-bearing zone of (a) Well **Γ** and (b) Well **H**. Blue dots identify laboratory core measurements. Black continuous lines describe points with equal value of the square root of the porosity-permeability ratio (*C*).

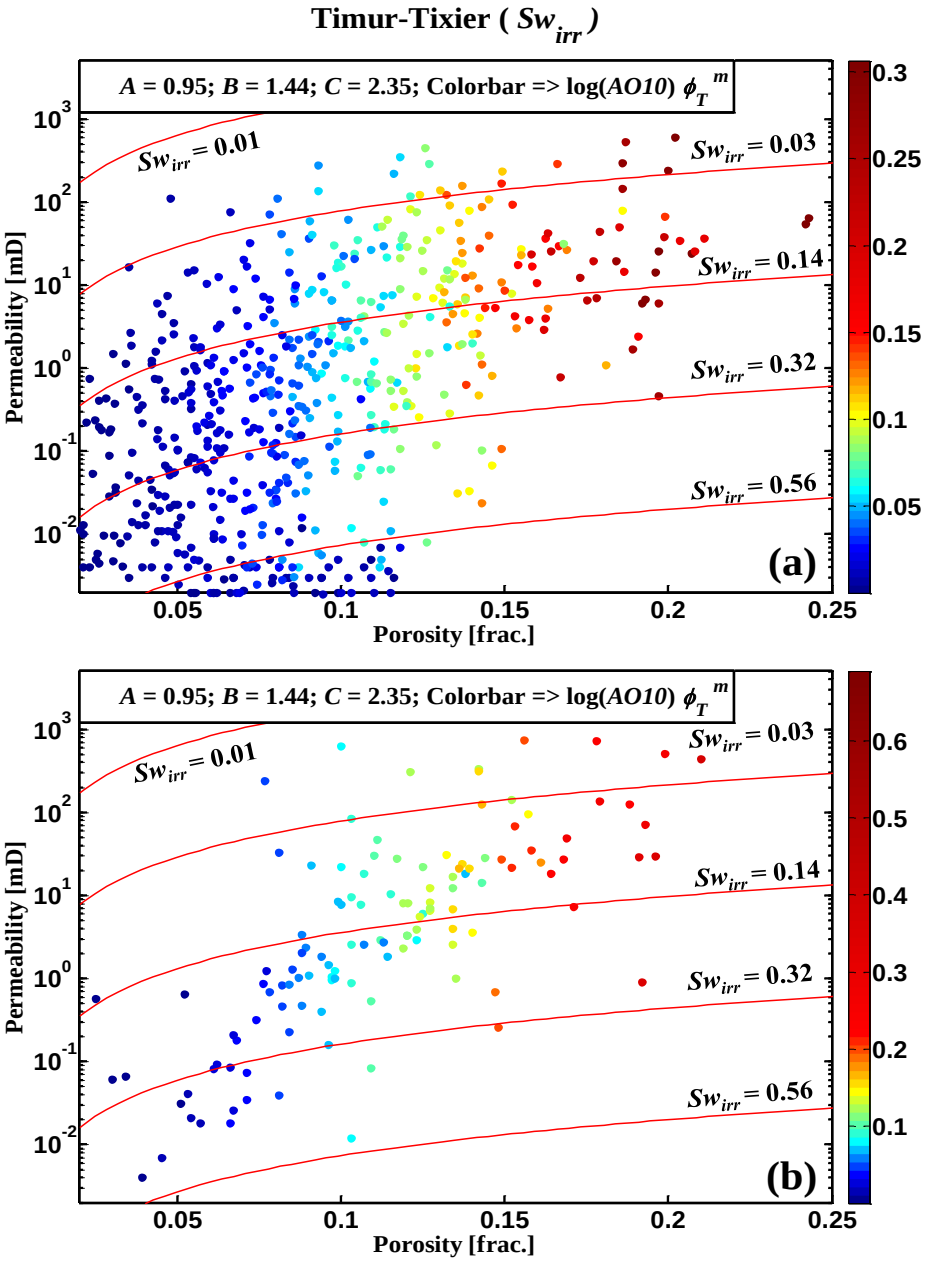

Figure 3.3: Cross-plot of total porosity and permeability used to diagnose and classify rock types using the irreducible water saturation method (Timur, 1969) in the oil-bearing zone of (a) Well **Γ** and (b) Well **H**. Colored dots identify laboratory core measurements. Red continuous lines describe points with equal value of irreducible water saturation. The color bar used to identify core measurements describes the base-10 logarithm of the shallowest-sensing apparent resistivity log (*AO10*) times total porosity (ϕ_T) raised to Archie's porosity exponent (m).

3.2 NEW METHOD BASED ON WELL LOGS

This work introduces a new rock-typing method that accounts for the high degree of spatial heterogeneity in the evaluated reservoir. The key to this method was to correlate rock information, well logs and petrophysical properties. Resistivity, NMR, density, and sonic logs were the basis for differentiating fluid flow units in the reservoir and, consequently, for detecting bed boundaries.

First, resistivity measurements exhibit large variations, whereas total porosity does not vary significantly (**Figure 2.1**, track 3 and 5). Analyses of thin sections, core measurements, and NMR logs indicate that the large variations in apparent resistivity are due to variations of irreducible water saturation in each layer (Diniz-Ferreira and Torres-Verdín, 2012). Mobile connate water is absent in the evaluated zone of the reservoir. Verwer *et al.* (2011) pointed out that in comparing two samples with the same total porosity, the sample dominated by an intricate network of micropores shows lower values of electrical resistivity than does the sample having large pores. This effect is attributed to carbonate pore structure. A large number of pores and pore connections result in a high apparent cross-section area available for flow of electrical current, which reduces electrical resistivity values. In contrast, isolated pores show a high resistivity for a given porosity because of the reduced number of pore connections (Verwer *et al.*, 2011).

Second, NMR *T2* distributions (**Figure 2.1**, track 8) provide independent information about pore-size distributions and fluid saturation. It was observed that layers containing large pore volumes associated with *T2* signals lower than 30 ms indicated rocks with low values of resistivity due to relatively large microporosity. In contrast, *T2* peaks having values greater than 30 ms were associated with oil occupying the large pores.

Finally, assuming that the sonic log responds to the most rigid section of the rock, depth intervals that exhibit a significant difference between total porosity and sonic porosity are commonly associated with vuggy porosity. The physical concept related to this assumption is that highly complex pore-structured carbonate rocks, such as boundstone, provide more contact area between grains than do rocks that contain interparticle and intercrystalline pores, thereby giving rise to faster sonic wave travel times for a given porosity (Mavko and Mukerji, 1995). In addition, the sonic wave front propagates faster in solids than in fluids, and consequently the time of flight will contain matrix information that bypasses large pores in the rock, such as vugs.

On the basis of the predominant type of porosity in each layer, the reservoir was divided into three different fluid flow units, as described in **Table 3.1**. **Figure 3.4** shows core photographs, well logs used to perform rock typing, core measurements, and thin sections in the oil-bearing zone of Well **H**. This figure shows that the comparison between well-log signatures and rock types is consistent with the properties summarized in **Table 3.1.** Differences in signatures of the observed well logs are associated with variations in pore connectivity (type of porosity) and permeability. Moreover, the transition between rock types does not occur sharply, hence it is common to encounter mixed or transitional layers or to encounter laminated layers with thicknesses below the resolution of well logs (**Figure 1.2**). In this thesis, those thin layers were classified and evaluated using core data.

Rock type	Porosity type	Resistivity values	*T2* distribution	Difference between total and sonic porosity
1	Interconnected	Medium-High	Large amount of porosity associated with relaxation time higher than 30 ms.	Less than 20%
2	Vuggy	High	Large amount of porosity associated with relaxation time higher than 30 ms.	Greater than 20%
3	Micro-porosity	Low	Large amount of porosity associated with relaxation time lower than 30 ms.	Less than 20%

Table 3.1: Signatures observed in well logs and used to identify different fluid-flow units.

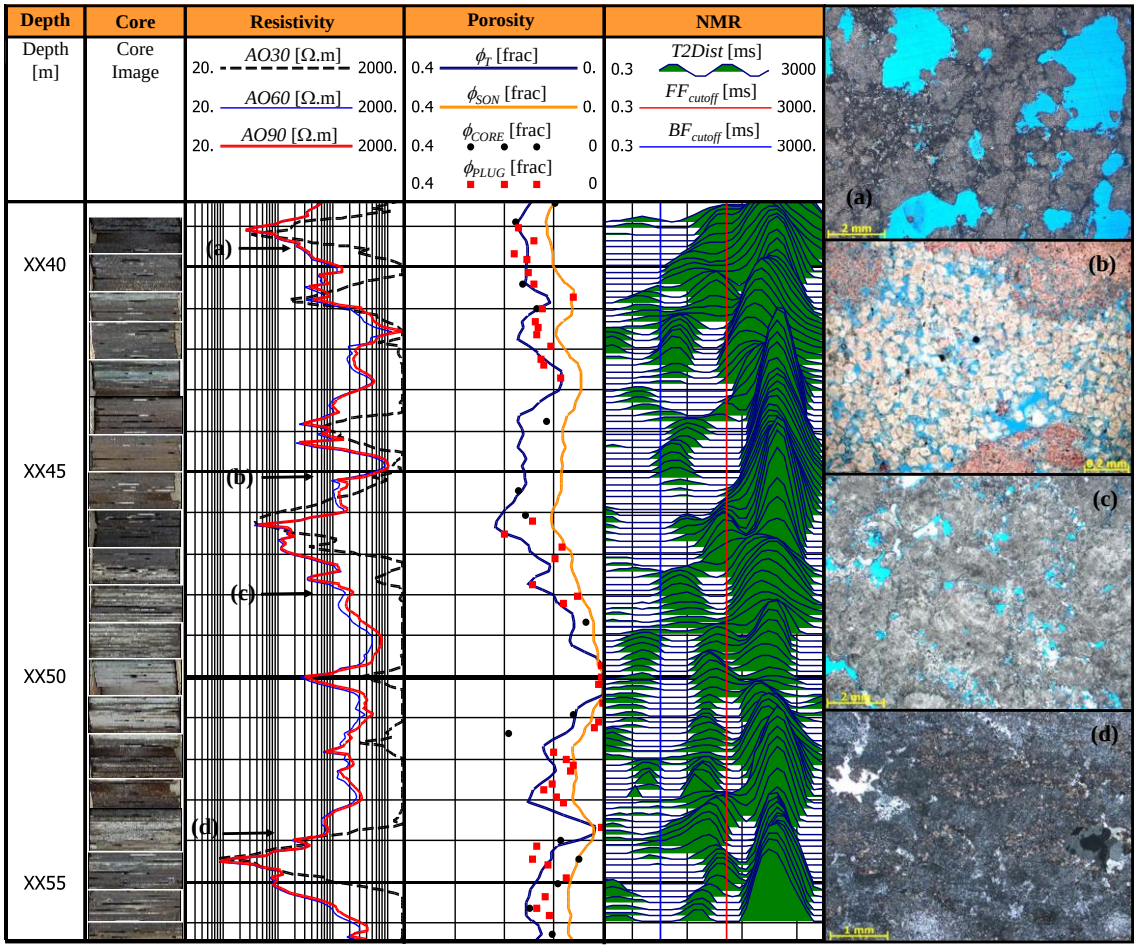

Figure 3.4: Comparison of well logs, core images and thin sections in the cored depth section of Well **H**. The well was drilled with OBM. Track 1: depth. Track 2: core image. Track 3: apparent resistivities with different depths of investigation. Track 4: computed NMR total porosity (dark blue), computed sonic (Wyllie) porosity (orange), and core porosity (black and red dots). Track 5: NMR *T2* distribution. Track 6: Thin sections at different depths (a) XX39 m: high interconnected vuggy porosity (k = 722 mD and ϕ_T = 0.178); rock type 2. (b) XX45 m: presence of dolomite crystals and high porosity; rock type 2 with secondary porosity. (c) XX47 m: high interconnected porosity and some isolated vuggy porosity (k = 95 mD and ϕ_T = 0.155); rock types 1 and 2. (d) XX49.8 m: laminated structure with cementation and microporosity; rock type 3.

Chapter 4: Construction of Static and Dynamic Multi-Layer Reservoir Models

Results from conventional interpretation methods were used to perform static and dynamic simulations in the evaluated wells. Next, the concept of Common Stratigraphic Framework (CSF), introduced by Voss *et al*. (2009), was used in this project to reduce the effects of mud-filtrate invasion and shoulder beds on well logs when estimating layer-by-layer static and dynamic petrophysical properties.

4.1 STATIC SIMULATIONS

This project involved the use of UTAPWeLS[1] software to select bed boundaries based on petrophysical rock typing (**Table 3.1**). Next, based on the predominant type of porosity, each bed was populated with petrophysical properties such as porosity, fluid saturation, and mineral composition. Subsequently, numerical simulations of well logs were performed to quantify the agreement of the constructed multi-layer model with available measurements. Adjustments in petrophysical layer properties were made until an acceptable agreement between numerical simulations and field measurements was reached (Voss *et al*., 2009). Static simulations reproduced neutron, gamma ray, photoelectric factor, density, and induction logs. Appendix C shows tables with initial estimates and the final set of properties yielded by the simulations. The NMR *T2* distribution along specific depth intervals was also numerically simulated to match field and core NMR measurements. Appendix A describes the forward method used to simulate NMR *T2* distribution; the assumptions behind the method are also explained in the appendix.

[1] Developed by The University of Texas at Austin's Research Consortium on Formation Evaluation.

4.2 DYNAMIC SIMULATIONS

The constructed static model was the basis for performing dynamic simulations. A dynamic reservoir model was constructed by simulating the process of mud-filtrate invasion to examine the dynamic petrophysical properties of the reservoir and to establish geological and petrophysical consistency. Dynamic simulations require input drilling variables such as type of mud, time of invasion, and overbalance pressure. Also included in the process are layer-by-layer values of porosity, permeability, capillary pressure, and relative permeability. Finally, the simulation requires pre-invasion fluid reservoir inputs such as salt concentration of connate water, initial fluid saturation, and reservoir temperature (Gandhi *et al*., 2013). The petrophysical properties used in static simulations were also used as initial values of pre-invasion reservoir properties. Next, radial distributions of water saturation were numerically simulated. Radial distributions of water saturation were transformed into radial distributions of electrical resistivity using Archie's equation and associated electrical parameters yielded by laboratory measurements (**Table 2.1**). Implementation of adequate dynamic parameters enabled the replication of all the available well-logs after the process of mud-filtrate invasion.

4.3 SIMULATIONS OVERVIEW AND PARAMETER SPECIFICATION

The flow chart in **Figure 4.1** describes the complete interpretation method, from petrophysical rock typing of bed boundaries to static and dynamic output of earth model properties. In this iterative manual process, the mismatch between measured and numerically simulated logs progressively decreases. For formations from which core measurements were not available, an initial estimate of petrophysical properties was made based on similar fluid flow units whose core measurements were available. The two petrophysical properties that most influence the numerical simulations are interconnected porosity and irreducible water saturation. These properties directly impact permeability

values. **Table 4.1** summarizes the rock and fluid properties assumed to describe saturation-dependent relative permeability and capillary pressure using the Brooks-Corey parametric formulation (Brooks and Corey, 1964). **Table 4.2** describes the mudcake, fluid, and formation properties assumed in the simulations of the process of mud-filtrate invasion in Well **X**.

Rock type	ϕ_r **[frac.]**	k **[mD]**	Sw_{irr} **[frac.]**	So_r **[frac.]**	k_{rnw}	e_{nw}	k_{rw}	e_w	P_c^0 **[psi.D$^{1/2}$]**	e_p
1	0.15	300	0.1	0.25	0.9	1.5	0.3	3	2	6
2	0.12	10	0.1	0.35	0.9	1.5	0.3	3	5	6
3	0.13	0.1	0.45	0.25	0.7	1.2	0.35	3	5	6

Table 4.1: Rock-fluid properties calibrated and optimized with the simulation of mud-filtrate invasion for rock types 1, 2, and 3. Where Sw_{irr} and So_r are irreducible water saturation and residual oil saturation, respectively; k_{rnw} and k_{rw} are the relative permeabilities for the non-wetting phase and wetting phase, respectively; e_{nw} and e_w are the experimental exponents for non-wetting phase and wetting phase relative permeability equations, respectively; P_c^0 is the coefficient for the capillary pressure equation, and e_p is the pore size distribution exponent, using the Brooks-Corey model (Brooks and Corey, 1964).

Variable	Unit	Value
Wellbore radius	inch	8.5
Maximum invasion time	days	15
Reservoir temperature	^{o}F	132
Initial reservoir pressure	psi	8150
Overbalance pressure	psi	320
Mud-filtrate viscosity (at STP)	cP	1
Formation compressibility	psi^{-1}	1×10^{-7}
Mudcake reference permeability	mD	0.01
Mudcake reference porosity	frac.	0.2
Mudcake compressibility exponent	frac.	0.4
Mudcake exponent multiplier	frac.	0.1
Connate-water salinity	ppm [NaCl]	250000

Table 4.2: Summary of mudcake, fluid, and formation properties assumed in the simulation of the mud-filtrate invasion process.

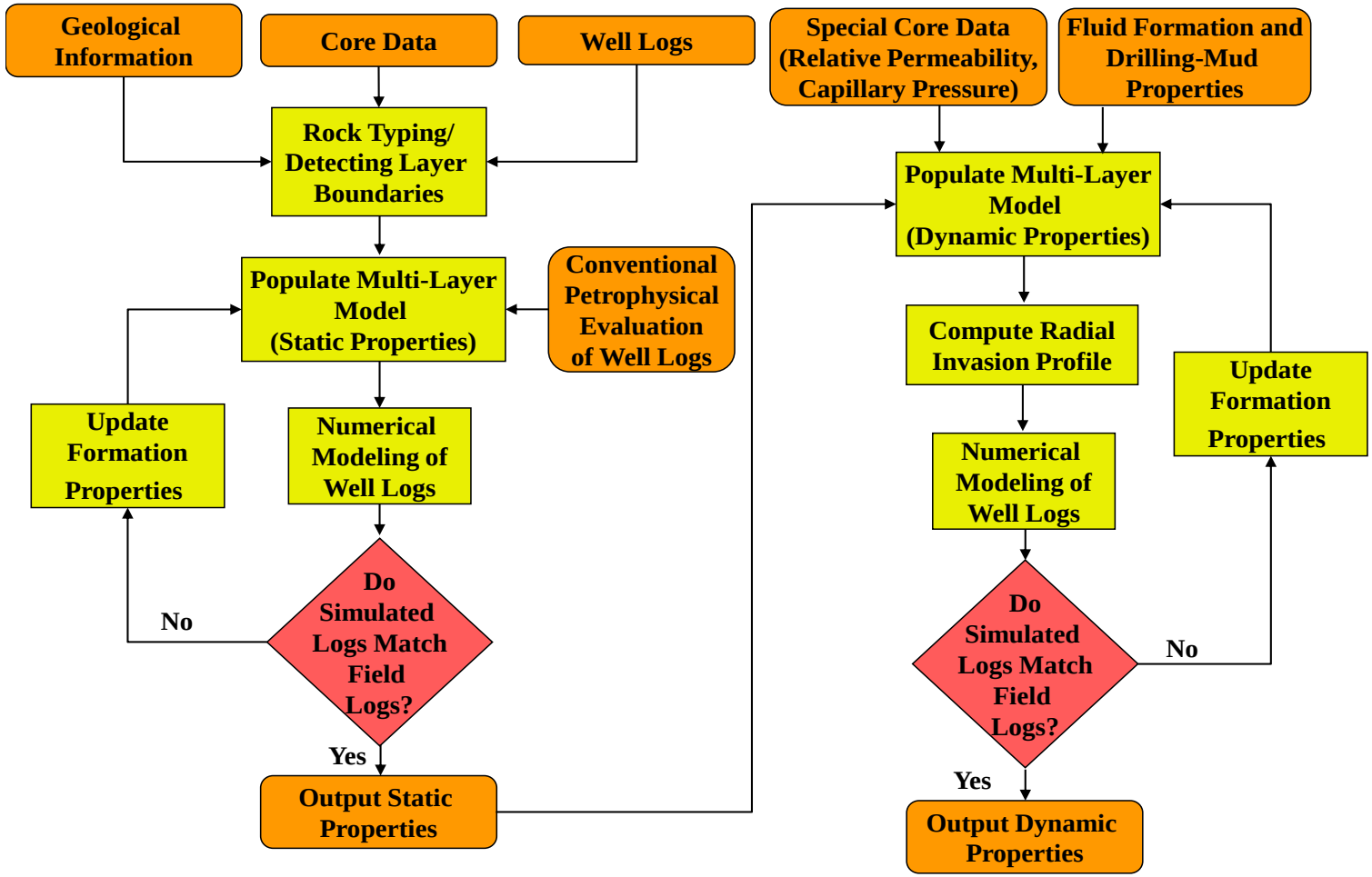

Figure 4.1: Flow chart describing the iterative interpretation method adopted in this thesis to reduce the mismatch between numerically simulated and measured resistivity and nuclear logs. This process yields static and dynamic multi-layer reservoir models that honor all the available measurements as well as the physics of mud-filtrate invasion.

Chapter 5: Static Simulations: Wells H and Γ

The evaluation method consists of dividing the reservoir into bed boundaries based on rock typing, populating each bed with consistent petrophysical properties (earth model), and performing static simulations. Adjustments to the earth model were made until an acceptable agreement was reached between available well logs and their numerical simulations, while honoring the core data. Simulated well logs were gamma-ray, apparent resistivity (induction), neutron, PEF, and density. To reproduce the high spatial heterogeneity of the reservoir, the model was constructed with high-resolution well logs and thin beds. In layers where core data were unavailable, reasonable petrophysical parameters, based on rock typing, were used to populate bed boundaries.

In the oil-bearing zone, there is no significant difference between the resistivity of mud filtrate and the resistivity of connate reservoir fluid; consequently there is no separation between apparent resistivity curves with different depths of investigation. Due to this effect, dynamic simulations are ineffective to estimate permeability in these zones.

5.1 STATIC SIMULATION

Figures 5.1 and **5.2** show the results obtained from static simulations in Well **H** and Well **Γ**, respectively. **Figure 5.3** shows a detailed comparison between petrophysical properties used in the simulations and the original values calculated with well logs. In **Figure 5.3** (track 1) it is observed that resistivity logs were unable to read the true resistivity formation values. This effect occurs because the resistivity tool lacks the vertical resolution necessary to reproduce the laminations in this section. Large discrepancies are observed on thin resistive layers pinched among low resistivity layers. Due to shoulder-bed effects numerical simulations were important to achieve the true

resistivity formation and to understand the petrophysical properties that govern the reservoir.

The simulations indicated that:

- For the same porosity, low values of resistivity correlated with high values of irreducible water saturation.
- In the oil-bearing zone, the separation of induction curves with different depths of investigation was due either to shoulder-bed effects or to limits in the sensitivity of induction tools.
- Total porosity calculated with density or NMR logs was a realistic initial estimate for constructing static models.
- Sonic porosity calculated with Wyllie´s equation was a realistic initial value for interconnected porosity in layers that exhibited vuggy porosity. As indicated by core samples, this behavior occurs because a fraction of the total porosity is isolated from the pore network (rock type 2).
- Previously estimated mineral concentrations were used as an input to nuclear-log simulations.
- Water saturation present in the oil-bearing zone was assumed to be immobile.

Implementation of these observations into the constructed static model yielded numerical simulations that matched all the available well logs.

The histograms in **Figures 5.4** and **5.5** show the relative variation between the initial values and the final estimates of porosity and water saturation for both wells. Values larger than 100% in **Figure 5.4** are associated with low porosity depth intervals. In Well **Γ,** low porosity values occur in XX05, XX21, XX33, and XX56m. These regions are associated with low-permeability intervals. Appendix C provides tables with initial and final sets of petrophysical parameters after performing the numerical simulations.

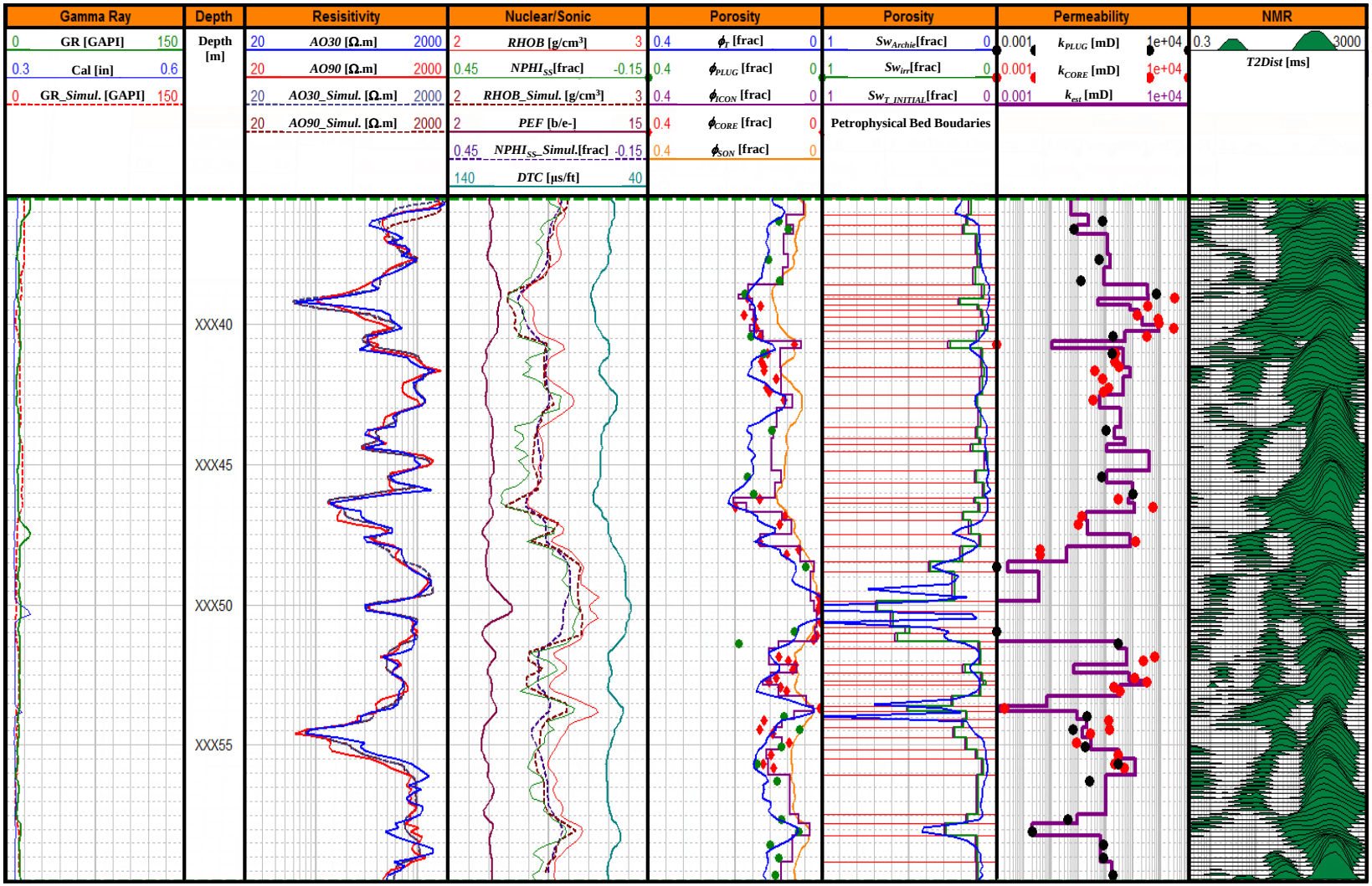
Gamma Ray
Depth
Resisitivity
Nuclear/Sonic
Porosity
Porosity
Permeability
NMR
0
GR [GAPI]
150
0.3
Cal [in]
0.6
0
GR_Simul. [GAPI]
150
Depth [m]
20
AO30 [Ω.m]
2000
20
AO90 [Ω.m]
2000
20
AO30_Simul. [Ω.m]
2000
20
AO90_Simul. [Ω.m]
2000
2
RHOB [g/cm³]
3
0.45
NPHI_SS[frac]
-0.15
2
RHOB_Simul. [g/cm³]
3
2
PEF [b/e-]
15
0.45
NPHI_SS_Simul.[frac]
-0.15
140
DTC [µs/ft]
40
0.4
ϕT [frac]
0
0.4
ϕPLUG [frac]
0
0.4
ϕICON [frac]
0
0.4
ϕCORE [frac]
0
0.4
ϕSON [frac]
0
1
SwArchie[frac]
0
1
Swirr[frac]
0
1
SwT_INITIAL[frac]
0
Petrophysical Bed Boudaries
0.001
kPLUG [mD]
1e+04
0.001
kCORE [mD]
1e+04
0.001
kest [mD]
1e+04
0.3
3000
T2Dist [ms]
XXX40
XXX45
XXX50
XXX55

Figure 5.1: Results of static simulations in Well **H** across the oil-bearing zone. The well was drilled with OBM. Dashed curves identify numerical simulations. Track 1: gamma-ray log (green), caliper log (blue), and simulated gamma-ray log (dashed red). Track 2: depth. Track 3: apparent resistivities acquired with different depths of investigation (red and blue), and simulated apparent resistivities with different depths of investigation (dashed dark red and dashed dark blue). Track 4: density (red), neutron porosity in sandstone units (green), PEF (purple), compressional slowness (teal), simulated density (dashed dark red), and simulated neutron porosity in sandstone units (dashed purple). Track 5: computed total porosity from mineral inversion (blue), computed sonic (Wyllie) porosity (orange), core porosity (green and red dots), and interconnected porosity used in the numerical simulations (purple). Track 6: total water saturation computed from Archie's equation (blue), irreducible water saturation used in the numerical simulations (green), total water saturation used in the numerical simulations (purple), and petrophysical bed boundaries (red). Track 7: core permeability (black and red dots), and estimated permeability from Timur-Tixier's equation using earth model results (purple). Track 8: NMR *T2* distribution.

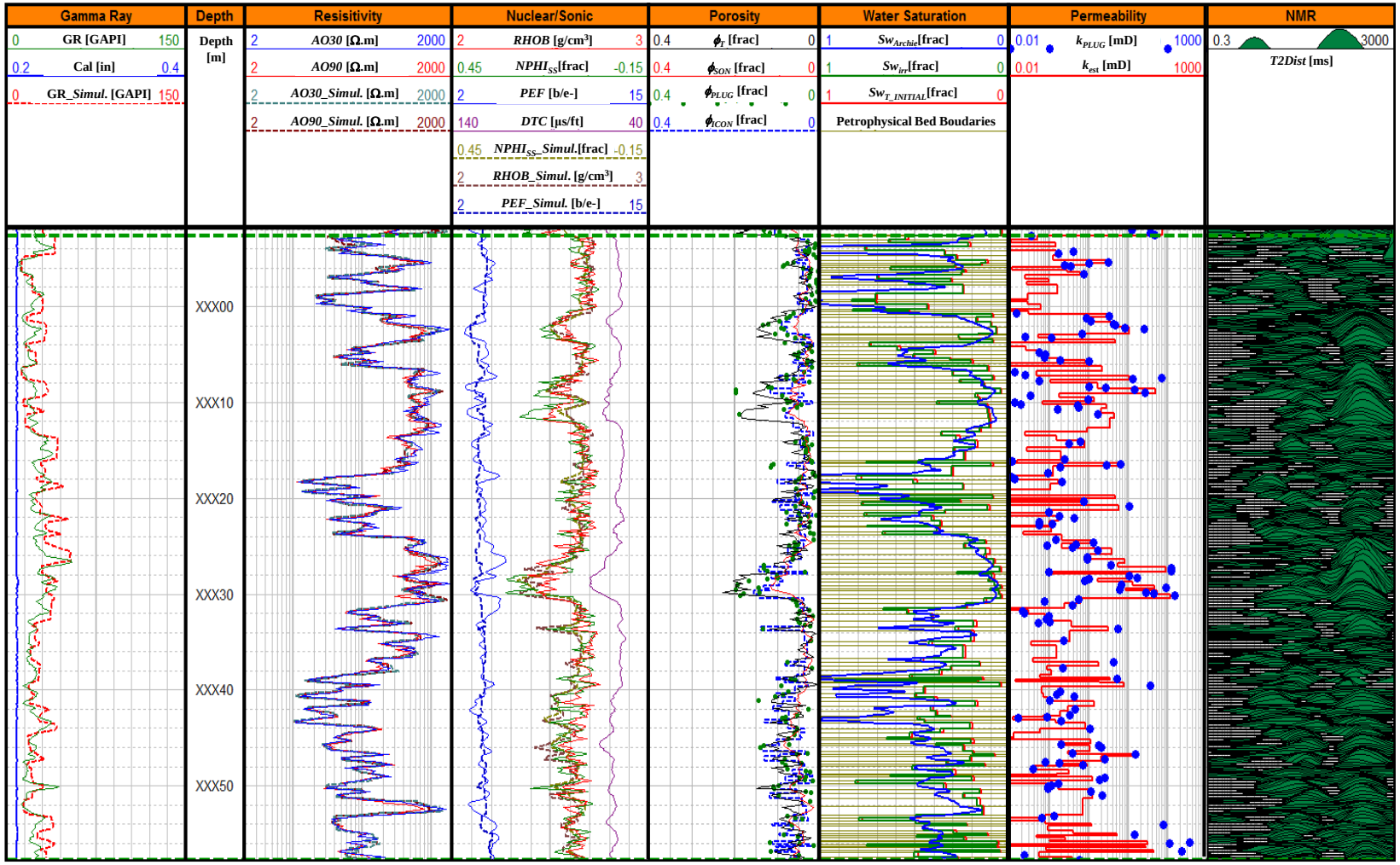
Gamma Ray
0 GR [GAPI] 150
0.2 Cal [in] 0.4
0 GR_Simul. [GAPI] 150
Depth
Depth [m]
XXX00
XXX10
XXX20
XXX30
XXX40
XXX50
Resisitivity
2 AO30 [Ω.m] 2000
2 AO90 [Ω.m] 2000
2 AO30_Simul. [Ω.m] 2000
2 AO90_Simul. [Ω.m] 2000
Nuclear/Sonic
2 RHOB [g/cm³] 3
0.45 NPHI_SS [frac] -0.15
2 PEF [b/e-] 15
140 DTC [µs/ft] 40
0.45 NPHI_SS_Simul. [frac] -0.15
2 RHOB_Simul. [g/cm³] 3
2 PEF_Simul. [b/e-] 15
Porosity
0.4 φ_T [frac] 0
0.4 φ_SON [frac] 0
0.4 φ_PLUG [frac] 0
0.4 φ_ICON [frac] 0
Water Saturation
1 Sw_Archie [frac] 0
1 Sw_irr [frac] 0
1 Sw_T_INITIAL [frac] 0
Petrophysical Bed Boudaries
Permeability
0.01 k_PLUG [mD] 1000
0.01 k_est [mD] 1000
NMR
0.3 3000
T2Dist [ms]

Figure 5.2: Results of static simulations in Well **Γ** across a depth section in the oil-bearing zone. The well was drilled with OBM. Dashed curves identify numerical simulations. Track 1: gamma-ray log (green), caliper log (blue), and simulated gamma-ray log (dashed red). Track 2: depth. Track 3: apparent resistivities acquired with different depths of investigation (red and blue) and simulated apparent resistivities with different depths of investigation (dashed dark red and dashed teal). Track 4: neutron porosity in sandstone units (green), simulated neutron porosity in sandstone units (dashed olive), density (red), simulated density (dashed dark red), PEF (blue), simulated PEF (dashed blue) and sonic logs (purple).Track 5: computed total porosity from mineral inversion (black), computed sonic (Wyllie) porosity (red), interconnected porosity used in the numerical simulations (blue), and core porosity (green dots). Track 6: total water saturation computed with Archie's equation (blue), total water saturation used in the numerical simulations (red), irreducible water saturation used in the numerical simulations (green), and petrophysical bed boundaries (olive). Track 7: core permeability (blue dots), and estimated permeability from Timur-Tixier's equation using earth model results (red). Track 8: NMR *T2* distribution.

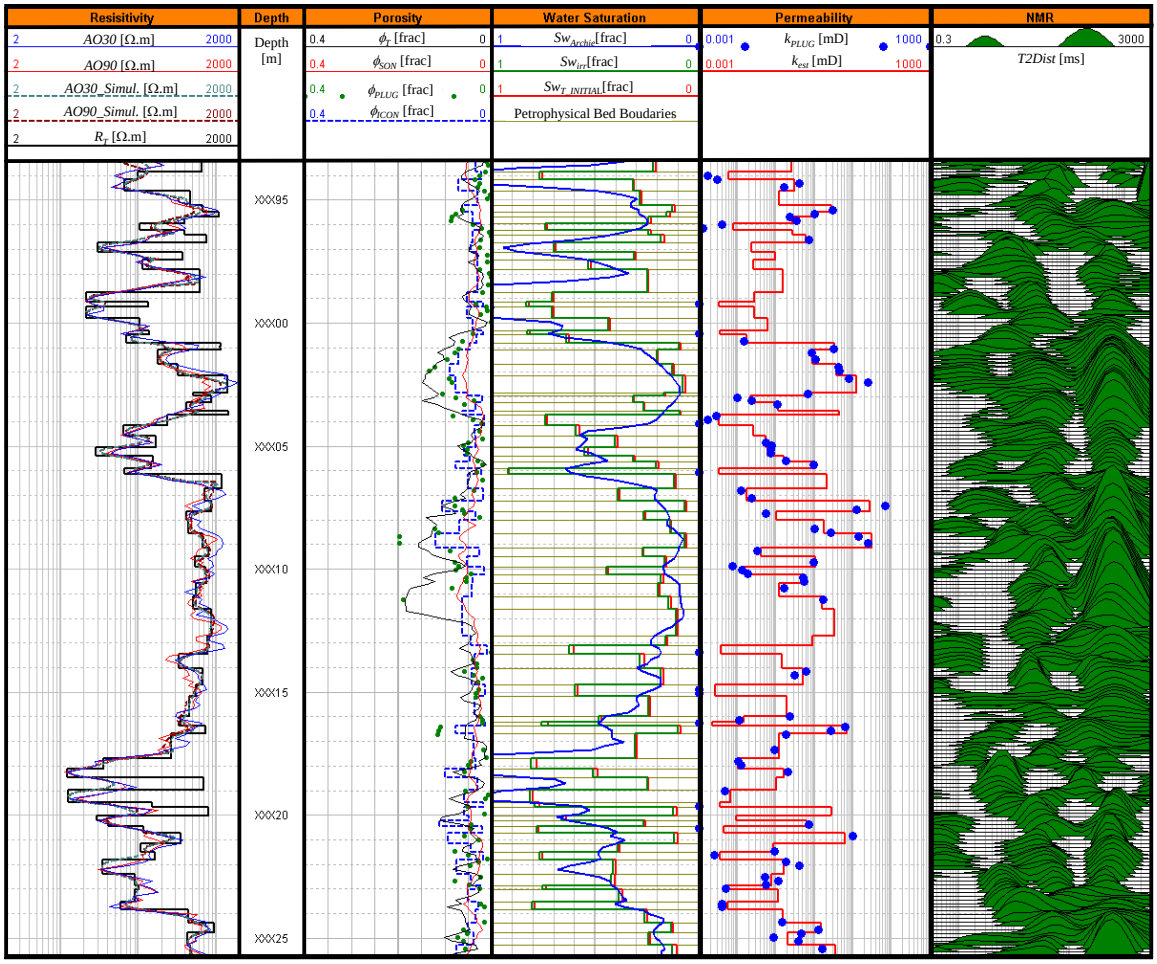

Figure 5.3: Detailed results of static simulations in Well **Γ** across a depth section in the oil-bearing zone. The well was drilled with OBM. Track 1: apparent resistivities acquired from different depths of investigation (red and blue), simulated apparent resistivities with different depths of investigation (dashed dark red and dashed teal), and true resistivity of the non-invaded zone (black). Track 2: depth. Track 3: computed total porosity from mineral inversion (black), computed sonic (Wyllie) porosity (red), interconnected porosity used in the numerical simulations (blue), and core porosity (green). Track 4: total water saturation computed with Archie's equation (blue), total water saturation used in the numerical simulations (green), irreducible water saturation used in the numerical simulations (red), and petrophysical bed boundaries (olive). Track 5: core permeability (blue dots), and estimated permeability from the Timur-Tixier's equation (red). Track 6: NMR *T2* distribution.

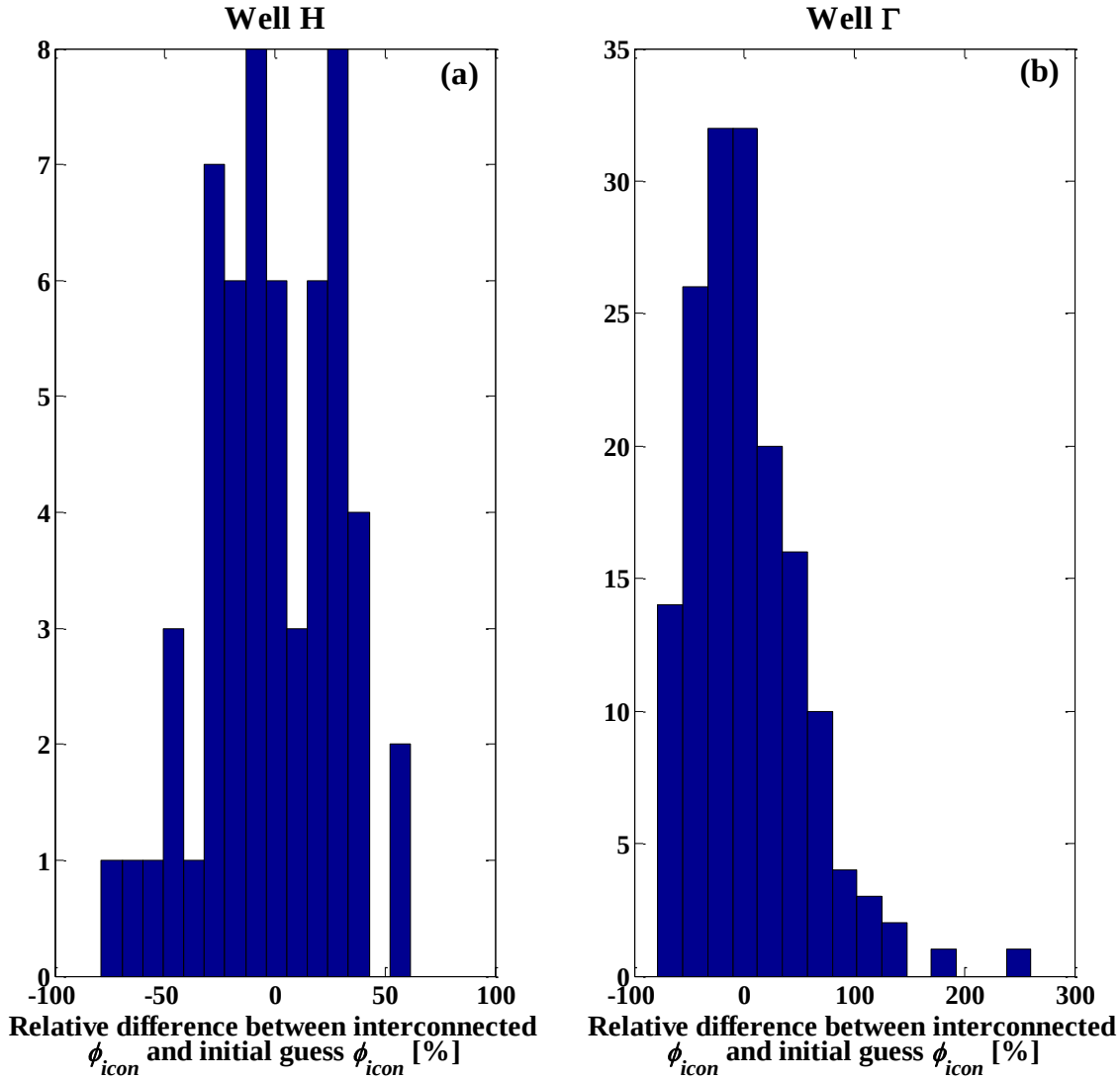

Figure 5.4: Histogram of the relative percent differences between the initial estimate of interconnected porosity and the final result obtained from numerical simulations. (a) Well **H** and (b) Well **Γ**.

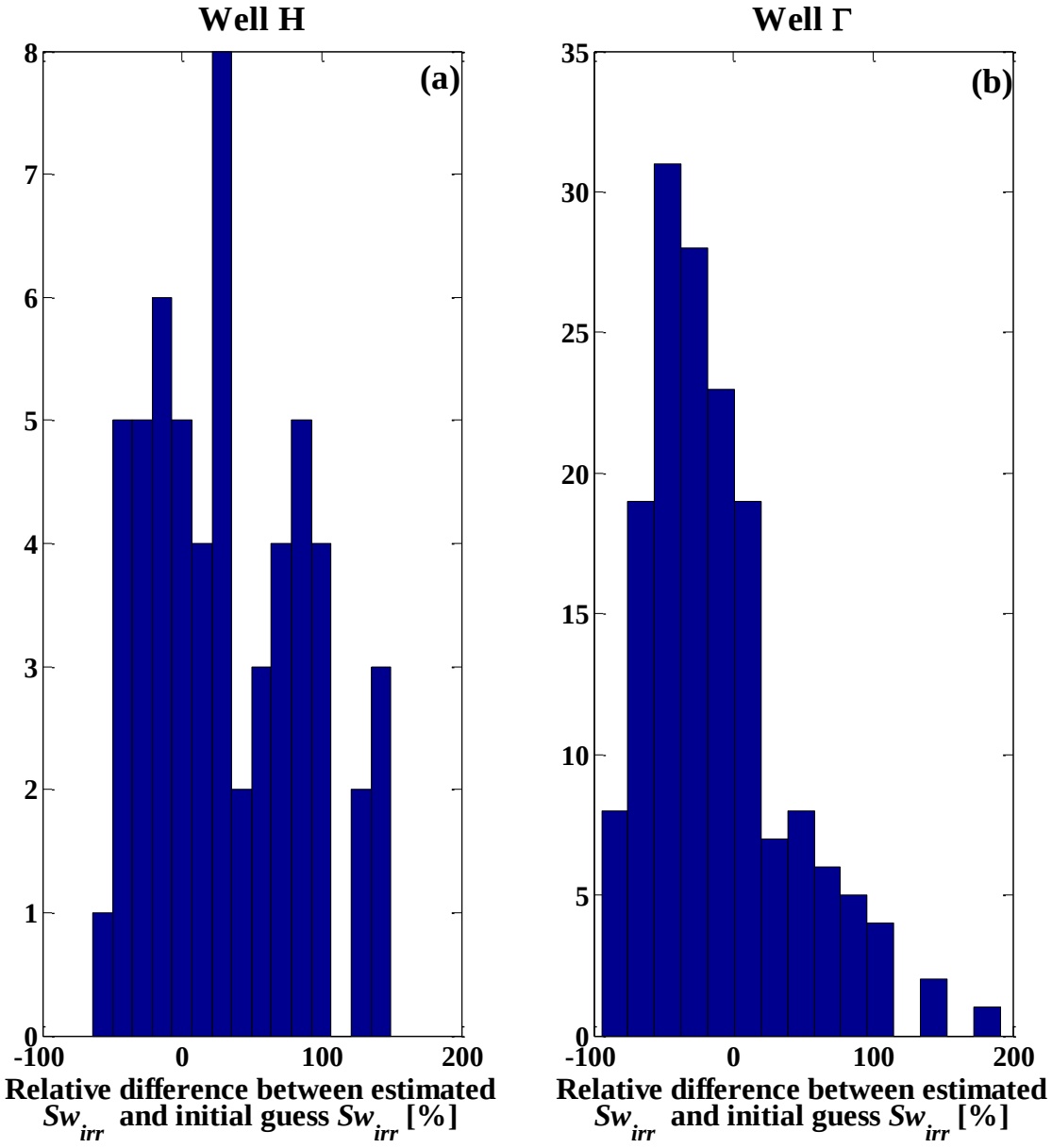

Figure 5.5: Histogram of the relative percent differences between the initial estimate of irreducible water saturation and the final result obtained from numerical simulations. (a) Well **H** and (b) Well **Γ**.

5.2 PERMEABILITY ESTIMATION

The radial resistivity profile in the oil-bearing zone of OBM wells is negligible because there is no change in water saturation with their substitution in the pore space, therefore producing no signature on the invasion profile. However, resistivity values correlate with Sw_{irr} values. After correcting interconnected porosity and irreducible water saturation for shoulder-bed effects, we implemented the Timur-Tixier (1969) equation to estimate permeability (**equation 5.1**). The permeability index is given by

$$k = A \cdot \phi_{ICON}^{B} \cdot Sw_{irr}^{C}, \qquad (5.1)$$

where ϕ_{ICON} is interconnected porosity calculated with static simulations, Sw_{irr} is irreducible water saturation estimated in static simulations, and A = 0.95; B = 1.44, and C = -2.35 are the specific constants used in the analysis of the reservoir which were obtained from least-squares correlations of core data. These constant parameters were used for all the evaluated wells and for all rock types. Corrected values of permeability were estimated when consistent values of ϕ_{ICON} and Sw_{irr} were used. The correct choice of these values depends on the predominant rock type for each layer: in layers that contain microporosity, the use of high values of Sw_{irr} is recommended, while low values of ϕ_{ICON} should be used in layers that contain isolated vuggy porosity. Results from this calculation are shown in **Figures 5.1 and 5.2**, track 7.

Figures 5.6 and **5.7** compare core permeability, and estimated permeability before and after shoulder-bed effects corrections in Wells **H** and **Γ,** respectively. To perform sensitivity analysis of the results, the initial ϕ_{ICON} or Sw_{irr} values were varied by +/-10%, then the second variable was recalculated using Archie's equation, and finally permeability was recalculated using **equation 5.1**. The largest and smallest results from

this calculation were used as error bars in permeability estimation (**Figures 5.6** and **5.7**). Similarly, **Figures 5.8** and **5.9** compare core porosity, and interconnected porosity before and after shoulder-bed effects corrections in Wells **H** and **Γ,** respectively. This method yielded a considerable improvement in permeability estimations as a result of the corrections applied. However, in regions where vertical reservoir heterogeneity was larger than the vertical resolution of well logs an accurate petrophysical interpretation based on well logs was challenging, if not impossible (**Figure 1.2**).

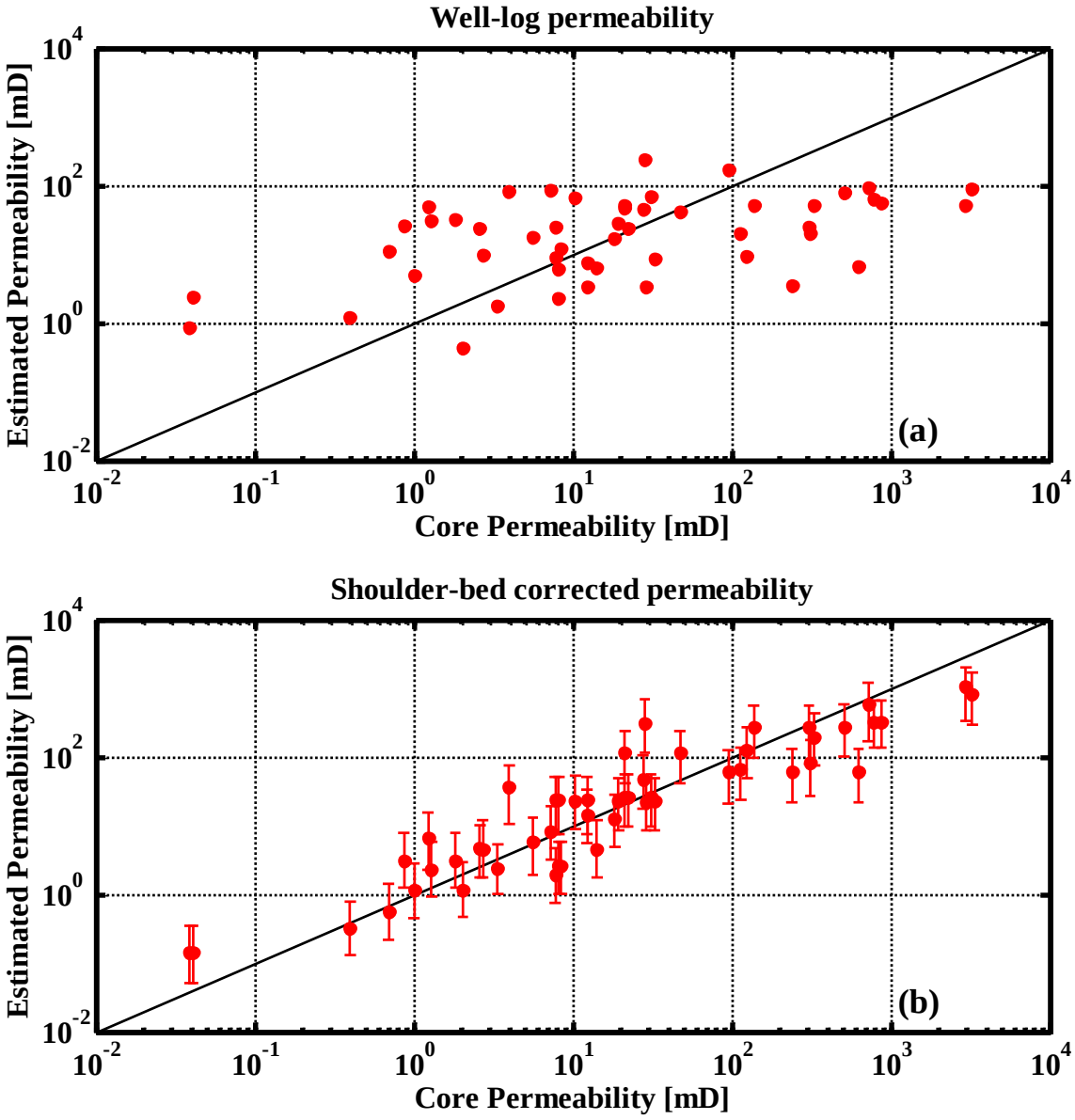

Figure 5.6: Cross plot of core permeability and estimated permeability using Timur-Tixier's equation, Well **H**. Comparison between (a) permeability estimated from well logs and (b) permeability estimated with shoulder-bed corrected well logs.

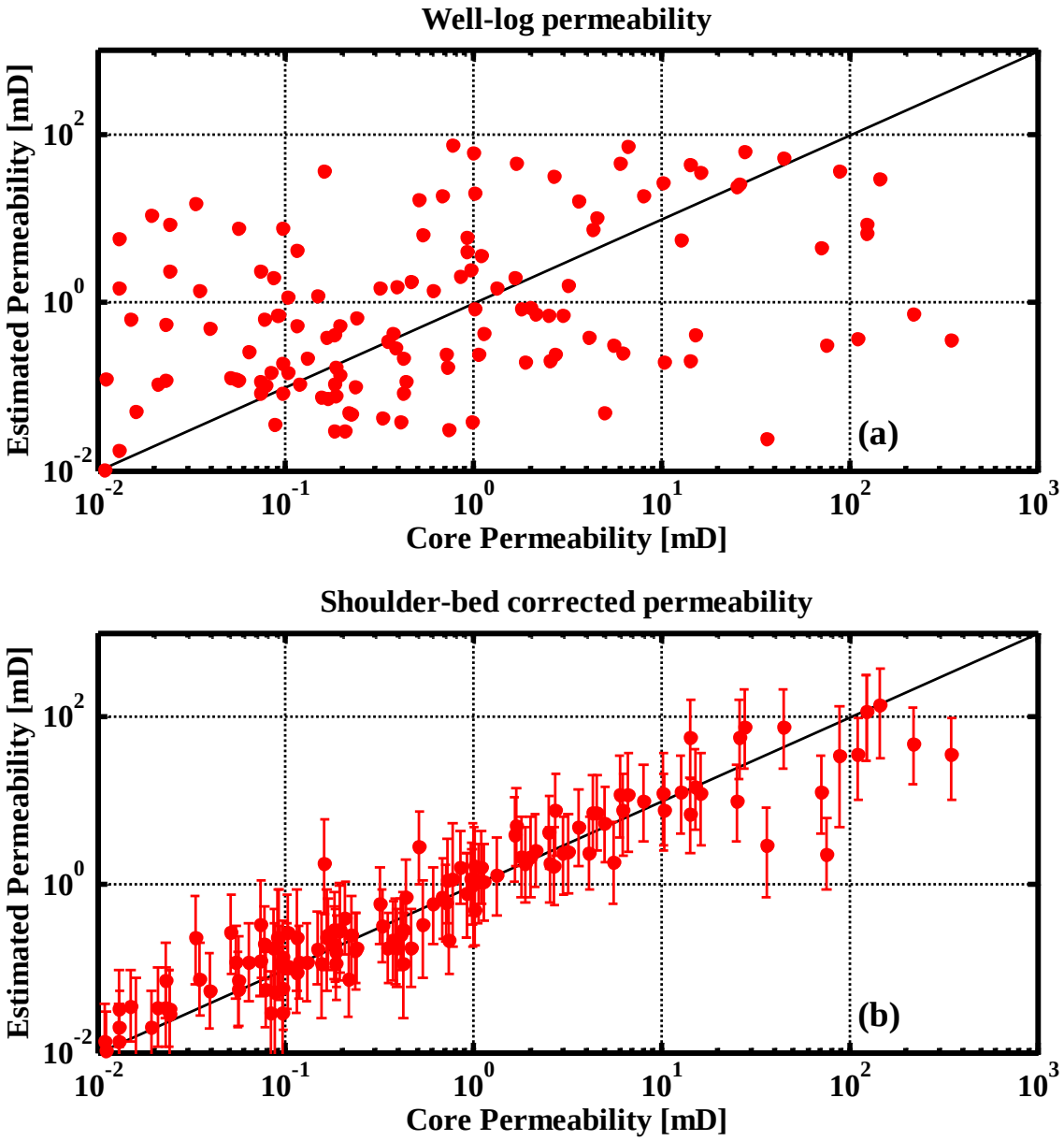

Figure 5.7: Cross plot of core permeability and estimated permeability using Timur-Tixier's equation, Well **Γ**. Comparison between (a) permeability estimated from well logs and (b) permeability estimated with shoulder-bed corrected well logs.

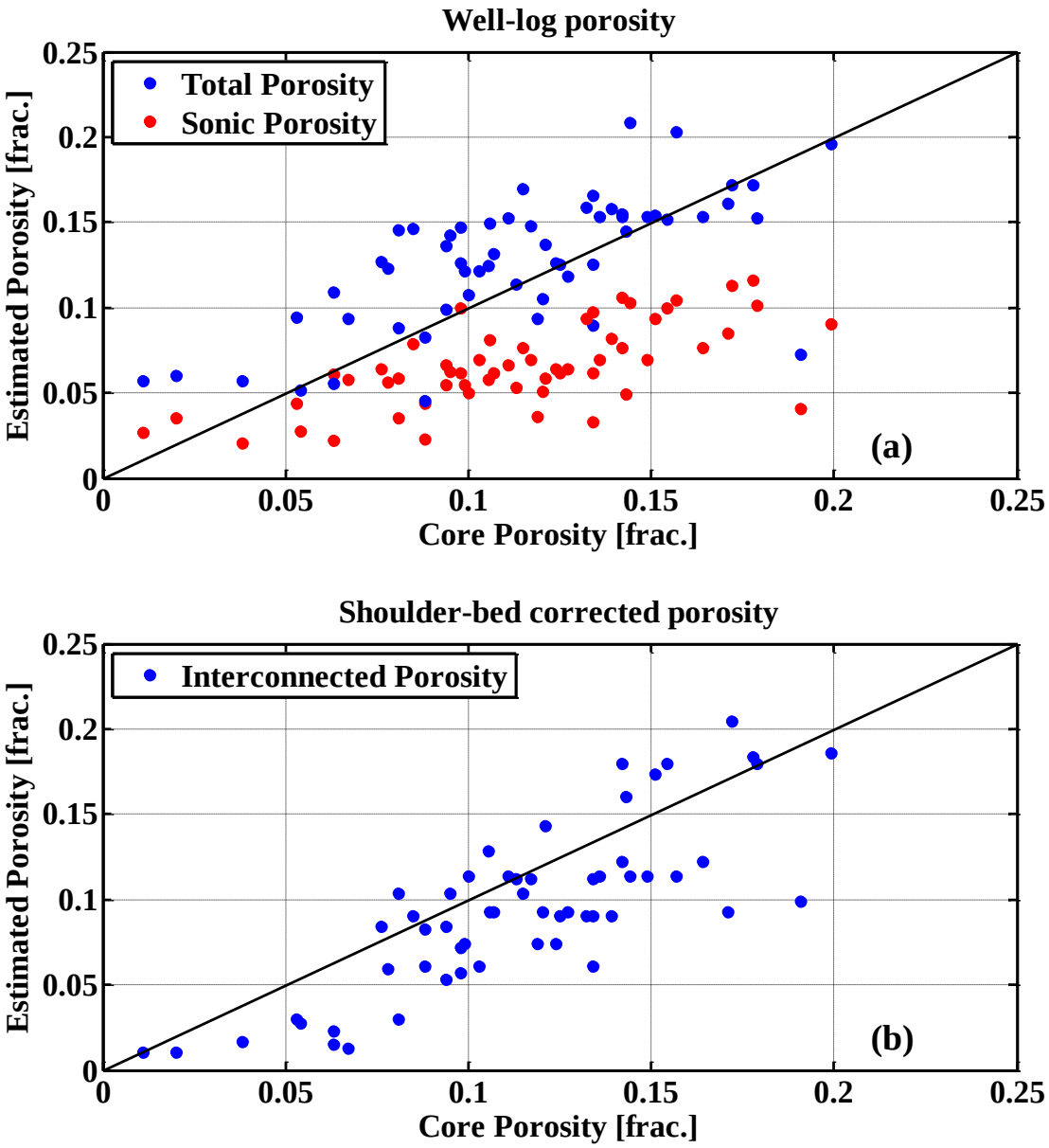

Figure 5.8: Cross plot of core porosity, estimated porosity, and sonic (Wyllie) porosity, Well **H**. Comparison between (a) porosity estimated from well logs, total porosity, and sonic (Wyllie) porosity, and (b) interconnected porosity used in the dynamic simulations with shoulder-bed corrected well logs.

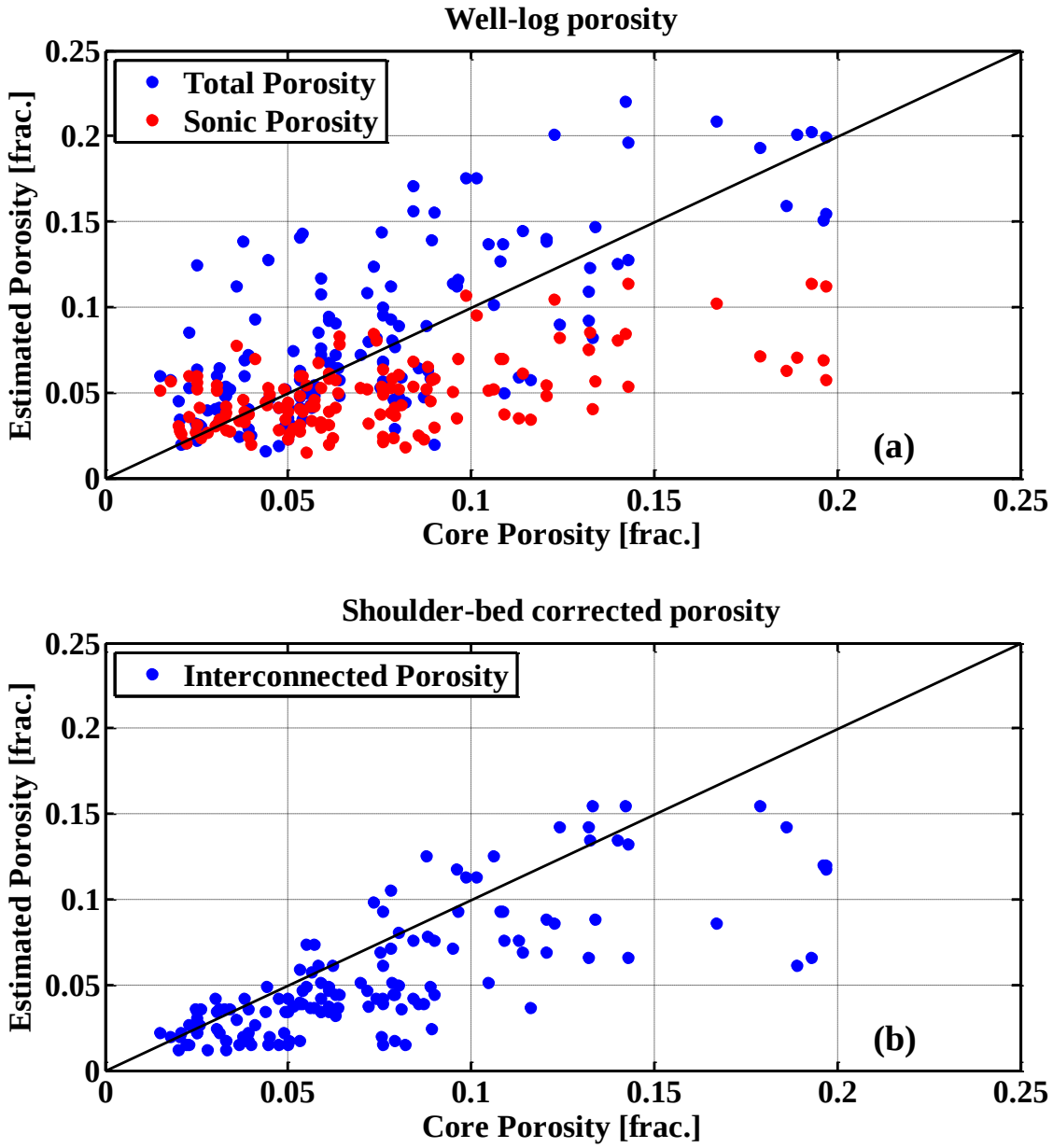

Figure 5.9: Cross plot of core porosity, estimated porosity, and sonic (Wyllie) porosity, Well **Γ**. Comparison between (a) porosity estimated from well logs, total porosity, and sonic (Wyllie) porosity, and (b) interconnected porosity used in the dynamic simulations with shoulder-bed corrected well logs.

5.3 NMR SIMULATIONS IN WELL Γ

Along the same depth interval used for static simulations in Well **H**, NMR *T2* distributions from well logs and core measurements were compared to numerical simulations based on a recently developed method to simulate NMR *T2* distributions in the presence of arbitrary pore-size distributions and fluid saturations (Appendix A). Core samples were saturated with light oil during laboratory measurements in order to reproduce well conditions (filtrate invasion around the borehole). Values of porosity and light-oil *T2* bulk input to the simulations were similar to those measured in the laboratory. **Figure 5.10** compares numerical simulations and core measurements for samples with different porosity/permeability behavior. On the basis of the numerical simulation of NMR *T2* distribution, it was possible to make the following observations:

- The irreducible water saturation used in NMR simulations is similar to that used in static simulations. The NMR peak associated with high values of *T2* represents large pores saturated with mud filtrate.
- To match calculated resistivity values with log measurements in core samples with isolated porosity, it was necessary to use values of porosity (ϕ_{ICON}) in Archie's equation that were lower than those used to simulate the NMR distributions (ϕ_{PLUG}). This discrepancy occurs because NMR measures total porosity while resistivity measurements are influenced by interconnected porosity. The largest discrepancy occurs in sample F1257. **Figure 5.10** shows that this plug contains vuggy porosity. **Table 5.1** compares estimated values of resistivity using total porosity (R_{T_Archie}) to the resistivity measurements (*AO10*). To match these resistivity values in sample F1257, it was necessary to assume that 0.19 of total porosity corresponded to isolated porosity.

- Normally, laboratory *T2* distributions do not match log measurements. This behavior is due to the difference in the volume of investigation, the fluid content, and the error source of the two measurements. Indeed, due to the large volume of investigation and the relatively high spatial heterogeneity of the reservoir, the NMR log generally measures the combined response of different layers of rock, thereby effectively merging each individual *T2* distribution. To analyze this effect, two different rock types were numerically mixed and the *T2* distribution of the mixture was plotted. **Figure 5.11** shows the result obtained from this simulation. The merging between measurements from different formations may cause misinterpretation of the distribution. Petrophysical properties such as total porosity and permeability of the mixed measurement will represent an average between petrophysical properties from homogeneous rocks. Appendix B provides additional details about this mixing effect on NMR measurements.

Sample number	F1211	F1249	F1257	F1409	F1527
ϕ_{PLUG} [frac.]	0.04	0.09	0.08	0.16	0.14
ϕ_{ICON} [frac.]	0.037	0.09	0.067	0.147	0.132
Sw_{irr} [frac.]	0.29	0.21	0.24	0.18	0.22
AO10 [Ω.m]	757	210	320	112	87
R_{T_Archie} [Ω.m]	689	211	198	96	76

Table 5.1: Comparison of apparent resistivities (*AO10*) measured by induction logs, and resistivities (R_{T_Archie}) calculated with Archie's equation using NMR simulation parameters. The simulation parameters are total porosity (ϕ_{PLUG}) and irreducible water saturation (Sw_{irr}); ϕ_{ICON} is the porosity fraction necessary to reproduce the apparent resistivity of the *AO10* measured induction log.

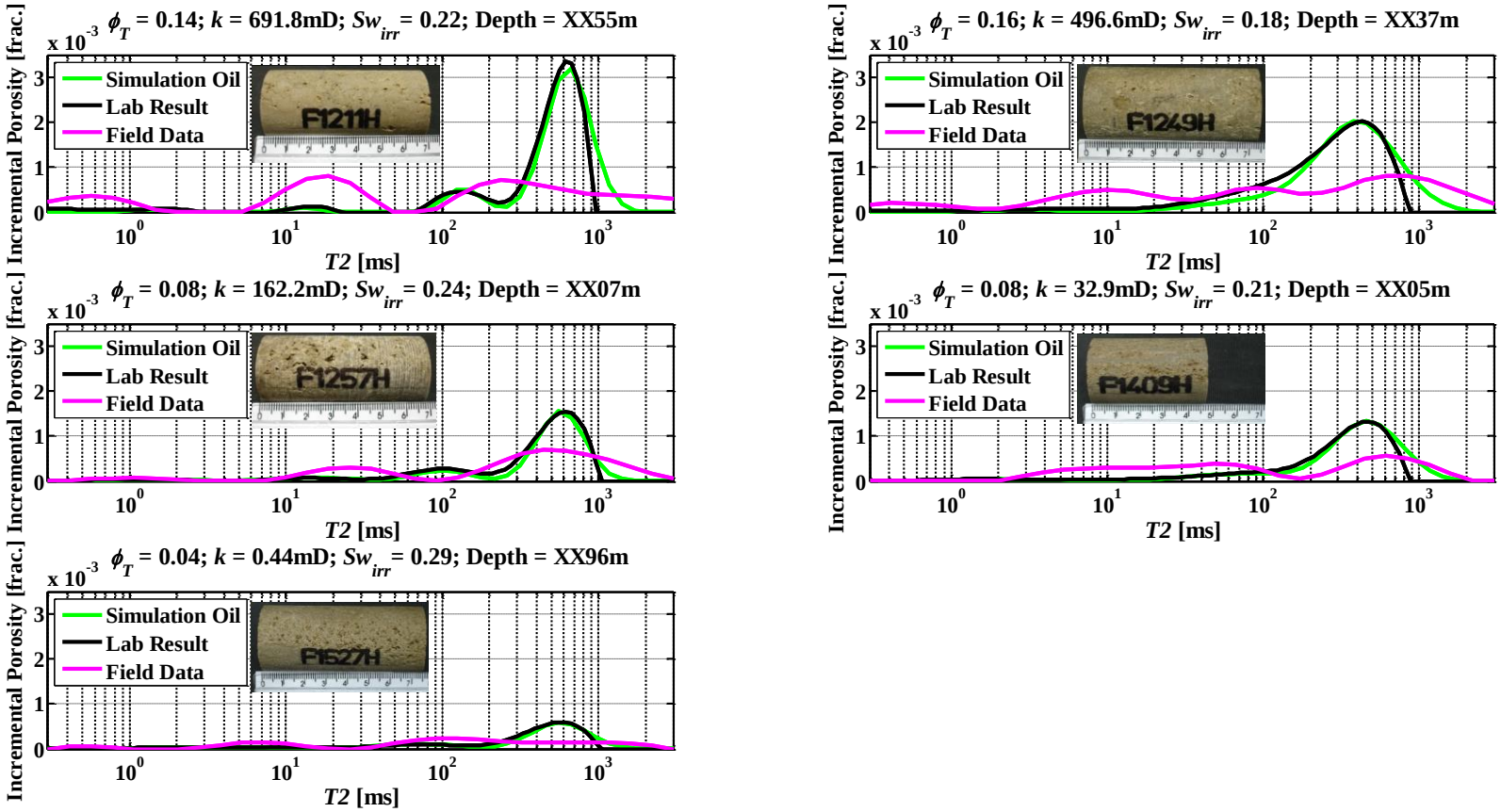

Figure 5.10: Results obtained from NMR numerical simulation for five different core samples retrieved from the same depth interval and used for static simulations of Well **Γ**. Each panel shows the laboratory *T2* distribution measurement (black), the measured *T2* distribution in the wellbore (magenta), the numerical simulation of the *T2* distribution with oil-saturated rock (red), and the photograph of the core sample.

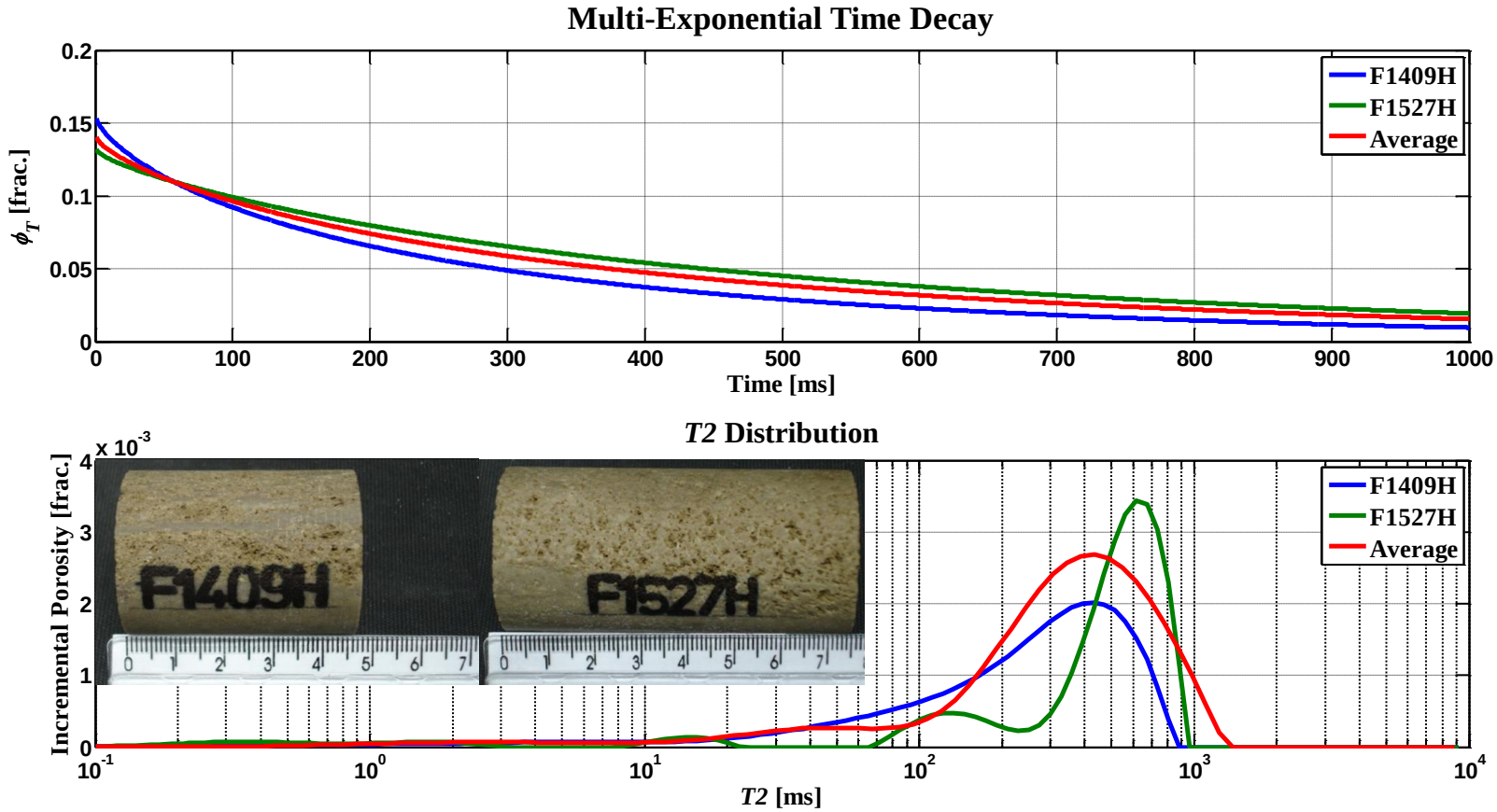

Figure 5.11: Results obtained from NMR numerical simulation (magnetization time decay and *T2* distribution) of a composite mixture of two rocks with different porosity-permeability behavior. Simulations assumed that the volume of investigation included 50% of each rock. Sample 1409H: k = 496.6 mD, ϕ_T = 0.16, and Sw_{irr} = 0.18 (blue). Sample 1527H: k = 691.8 mD, ϕ_T = 0.14, and Sw_{irr} = 0.22 (green). The composite mixture of the two samples is identified with red curves.

Similarly, the algorithm presented on Appendix A was used to simulate well log NMR *T2* distributions of Well **H**. The NMR log is subject to shoulder-bed effects, variable fluid composition in the volume of investigation (drilling-fluid invasion), and adverse conditions in the wellbore during the measurements. **Figure 5.12** compares well log measurements and simulations for Well **H**. **Table 5.2** summarizes properties used in simulations, well logs measurements, and core data values for several simulated depths. NMR simulations based on the well log corroborate the results obtained with core data NMR simulations. Additionally, results of the well-log NMR simulations indicate that:

- The free-fluid peak is highly dependent on the amount of drilling fluid invading the formation and remains near the wellbore during NMR measurements. The *T2* bulk ($T2_B$) used in NMR simulations is fluid dependent. Different $T2_B$ values were used to match NMR simulation with field measurement for different samples. Values varied between formation fluid and filtrate *T2* bulk (Toumelin *et al.*, 2004). Cross validation between NMR and resistivity simulations is not possible due to lack of resistivity contrast between filtrate and fluid formation.
- The amount of invaded fluid directly impacts permeability estimations due to shifting in the NMR *T2* free fluid peak. Using a pre-established theoretical *T2* cutoff in a shifted *T2* distribution may produce an incorrect free fluid/total bound fluid ratio. This incorrect value applied in the Timur-Coates' equation will lead to erroneous permeability estimation. Instead of using a sharp *T2* cutoff, I separated the *T2* distribution in single log-Gaussian distributions. After, I quantified the amount of fluid present in each Gaussian and estimated free fluid/bound fluid ratio based on this quantification. **Table 5.2** compares permeability estimations based on a pre-established theoretical *T2* cutoff (k_{Tim_Coat}) with permeability

estimations based on quantification of fluid present in each single log-Gaussian distribution (k_{Gauss}).

- Due to the presence of isolated vuggy porosity in this region, an important depth to analyze is XX11 (**Tables 5.2**). At this depth, measured permeability (k_{PLUG}) is 1.69 mD and estimated permeability with NMR (k_{Gauss}) is 190 mD. This discrepancy is also present in the apparent resistivity; the well log (*AO10*) is 649 Ω.m and resistivity estimation using Archie's equation (R_{T_Archie}) is 142 Ω.m. To match the resistivity values, I assumed that 45 % of the porous volume is associated with isolated vuggy porosity. Using this new porosity value (ϕ_{ICON}) and corrected ratio between free fluid and bound fluid, the new estimated permeability is 5.64 mD. This value is consistent with measurements and static simulations. At this depth interval, the interconnected porosity value used on the static simulations is similar to the value calculated with the sonic log.

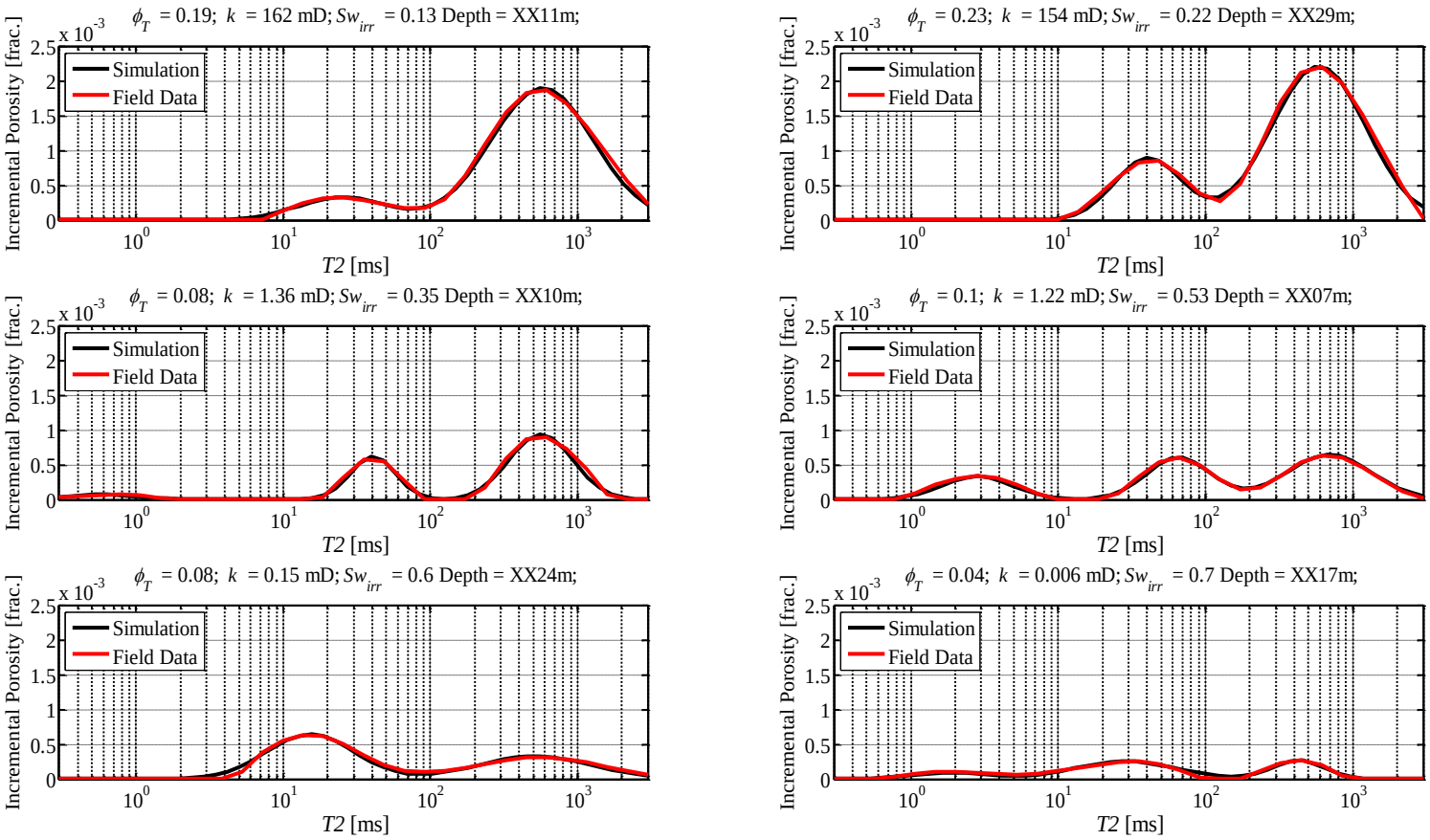

Figure 5.12: Results of NMR numerical simulation for six different depth samples retrieved from the same depth interval used for static simulations of Well **Γ**. Each panel shows the well-log *T2* distribution (red) and the numerical simulation of the *T2* distribution assuming an oil-saturated rock (black).

Depth	XX07	XX10	XX11	XX17	XX24	XX29
ϕ_{PLUG} [frac.]	0.1	0.08	0.19	0.04	0.08	0.23
Sw_{irr} [frac.]	0.53	0.35	0.13	0.7	0.6	0.22
AO10 [Ω.m]	77	416	649	80	42	117
R_{T_Archie} [Ω.m]	18	84	142	70	21	25
$T2_B$ [ms]	670	570	580	520	430	590
k_{PLUG} [mD]	0.08	0.97	1.69	<0.0001	0.15	146
k_{Tim_Coat} [mD]	1.22	1.36	162	0.006	0.15	154
k_{Gauss} [mD]	0.75	1.33	190	0.004	0.18	153

Table 5.2: Comparison of petrophysical properties measured from cores and well logs and properties estimated with NMR simulations (Well **Γ**); $T2_B$ of 7cp median crude (OBM) = 200 ms and $T2_B$ of 1cp light crude (formation oil) = 1000 ms (Toumelin *et al.*, 2004).

Chapter 6: Static and Dynamic Simulations: Well X

The evaluated interval of Well **X** is fully saturated with water. Well-log measurements were acquired at two different times (**Figure 2.3**). In the first case, only a negligible amount of OBM invaded the formation, and did not alter well-log measurements drastically. In this first measurement, I applied the same procedure used to perform static simulations in Wells **H** and **Γ.** In the second time lapse-measurement, OBM invaded the formation producing separation between apparent resistivity curves with different depth of investigation; resistivity curves were used to perform dynamic simulations. For free water level regions, dynamic simulations of the OBM invasion process were key in obtaining reliable permeability estimations of the formation.

6.1 Static and Dynamic Simulation in Free Water Depth Intervals

Results of conventional petrophysical evaluation methods were used to perform static and dynamic simulations in the interval. The Common Stratigraphic Framework, presented by Voss *et al.,* (2009), was used to perform the numerical simulations of all the available well logs. In addition to the CSF method and to increase interpretation reliability, I numerically simulated NMR *T2* distribution along the same depth interval that I performed static and dynamic simulations (Diniz-Ferreira and Torres-Verdín, 2012).

Presence of microporosity at the evaluated interval reduces rock permeability. This interval was interpreted as a mix of rock types 1 and 3 (**Table 3.1**). After rock typing, bed boundaries were then populated and static simulations using all the available well logs of the first time-lapse were performed. **Figure 6.1** shows layer-by-layer static simulations, including NMR simulations. Adjustments to static petrophysical properties were made until an acceptable agreement between simulations and measurements was

reached. Static simulations of nuclear and resistivity logs helped the accurate estimation of the interval total porosity. However, since this is a free-water depth interval, it is not possible to accurately estimate irreducible water saturation based on static simulations. Without reliable estimations of irreducible water saturation, the Timur-Tixier's equation cannot be used in this first time lapse measurement.

Next, numerical simulations of mud-filtrate invasion were performed to examine dynamic petrophysical properties of the reservoir. In the second run, which occurred 15 days after the first measurements, it is possible to observe the separation in the induction curves due to OBM invasion (**Figure 6.2**). The second time-lapse measurement was used in performing dynamic simulations. In the first attempt a blind test was performed; at this stage no core measurements were available. After core measurement became known, the permeability of the dynamic simulations was compared with core measurements. The result exhibited less than one log scale of error. Indeed, the method helped in predicting the low permeability values of the interval.

Core measurements helped upgrade our model and generated better results. Initial and final sets of properties used on static simulations are shown in Appendix C – **Table C.3**. Layer-by-layers adjustments of static and dynamic petrophysical properties (**Figure 4.1**) were performed to reproduce all available well-logs and to honor core measurements. **Figure 6.2** shows results obtained from dynamic simulations in the free water level of Well **X**. The dynamic multi-layer reservoir model was constructed to match well logs and their numerical simulations. When core measurements were not available, the petrophysical properties used in simulations were chosen based on rock type. Additionally, calculated sonic (Wyllie) porosity was used as an initial hypothesis of interconnected porosity in dynamic numerical simulations.

The permeability index was estimated using different methods. **Figure 6.2** – track 9 shows the permeability curves produced by dynamic simulations, the Timur-Tixier's **equation (5.1)**, and the Timur-Coates' **equation (B.2)** before invasion, and after invasion. **Table 6.1** shows the parameters acquired using least squares for each equation. **Figure 6.2** affirms the use of core measurements allows the estimation of correct parameters and produces reliable permeability index curves. Additionally, using the correct rock-typing, it is possible to qualitatively interpret the permeability of each interval.

Equations	***A***	***B***	***C***
Timur-Tixier	0.4	2	1.46
Timur-Coates water	11032	1.82	2.01
Timur-Coates oil	14145	1.32	2.34

Table 6.1: Comparison of parameters estimated with least-squares regression for different equations used to calculate permeability in Well **X.**

Regions having low porosity and permeability show the deepest OBM invasion. This behavior is related to the physics of mud filtrate invasion: 1) the formation of the mudcake is inefficient and slower in low permeability zones, 2) with a small pore volume, only a small amount of filtrate invading the formation will dislocate formation fluid from a larger radius around the wellbore. The deeper invasion in the interval is observed in the second layer (**Figure 6.2** – track 8); this layer has the smallest porosity and permeability.

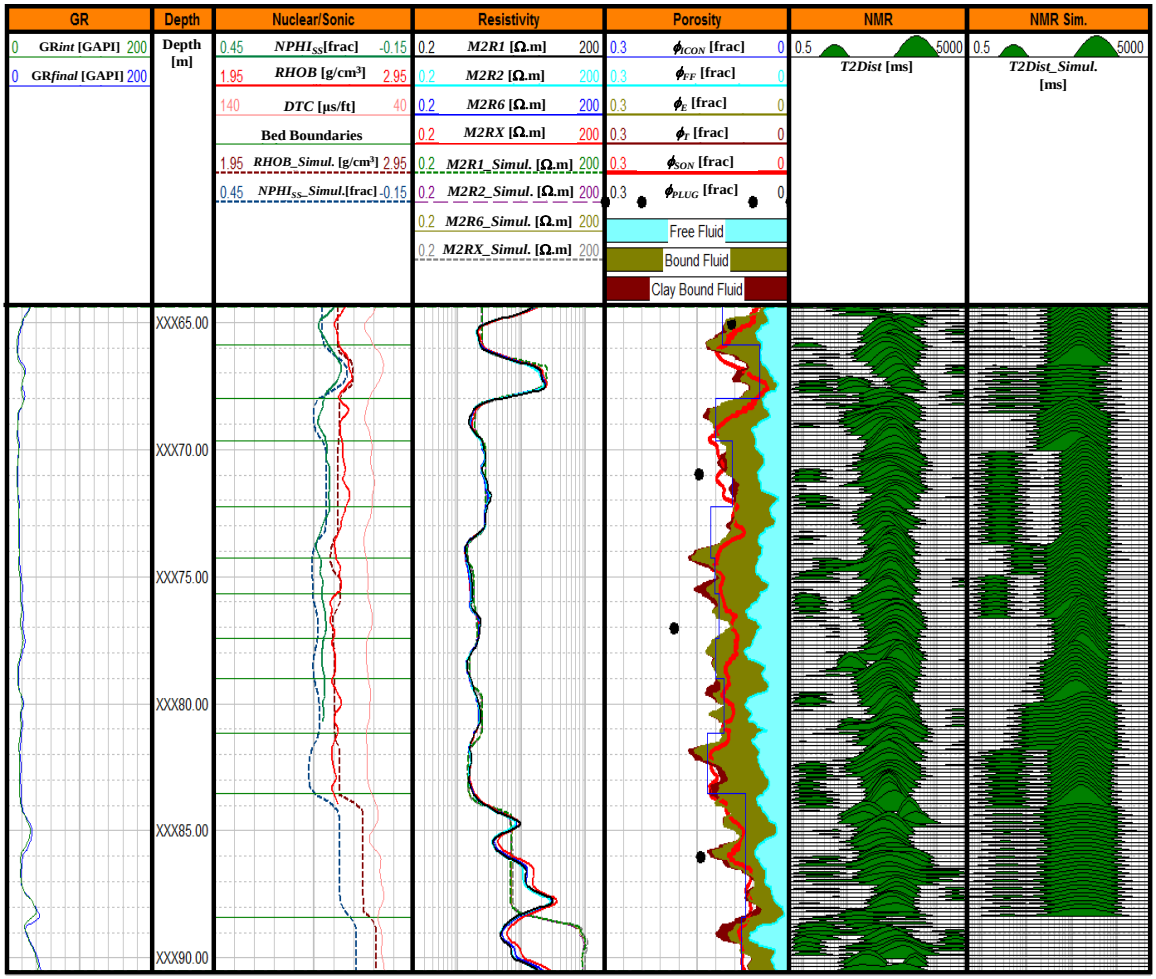

Figure 6.1: Results of static simulations in Well **X** across a short depth section fully saturated with water. The well was drilled with OBM. Measurements were acquired after 1 day of OBM invading the formation. Dashed curves identify numerical simulations. Track 1: gamma-ray of the intermediate phase (green) and gamma-ray of the final phase (blue). Track 2: depth. Track 3: apparent resistivities with different depths of investigation (red, blue, aqua, dark blue and black), and simulated apparent resistivities (dashed red, dashed blue, dashed aqua, dashed dark blue and dashed black). Track 4: density (red), neutron porosity in sandstone units (green), sonic (light pink), PEF (purple), simulated density (dashed red), and simulated neutron porosity in sandstone units (dashed dark green). Track 5: computed sonic (Wyllie) porosity (red), porosity and porosity fractions estimated with NMR *T2* distributions (light blue, olive, and brown), interconnected porosity used in the numerical simulations (blue), and core porosity (black dots). Track 6: NMR *T2* distributions. Track 7: numerical simulations of the NMR *T2* distributions.

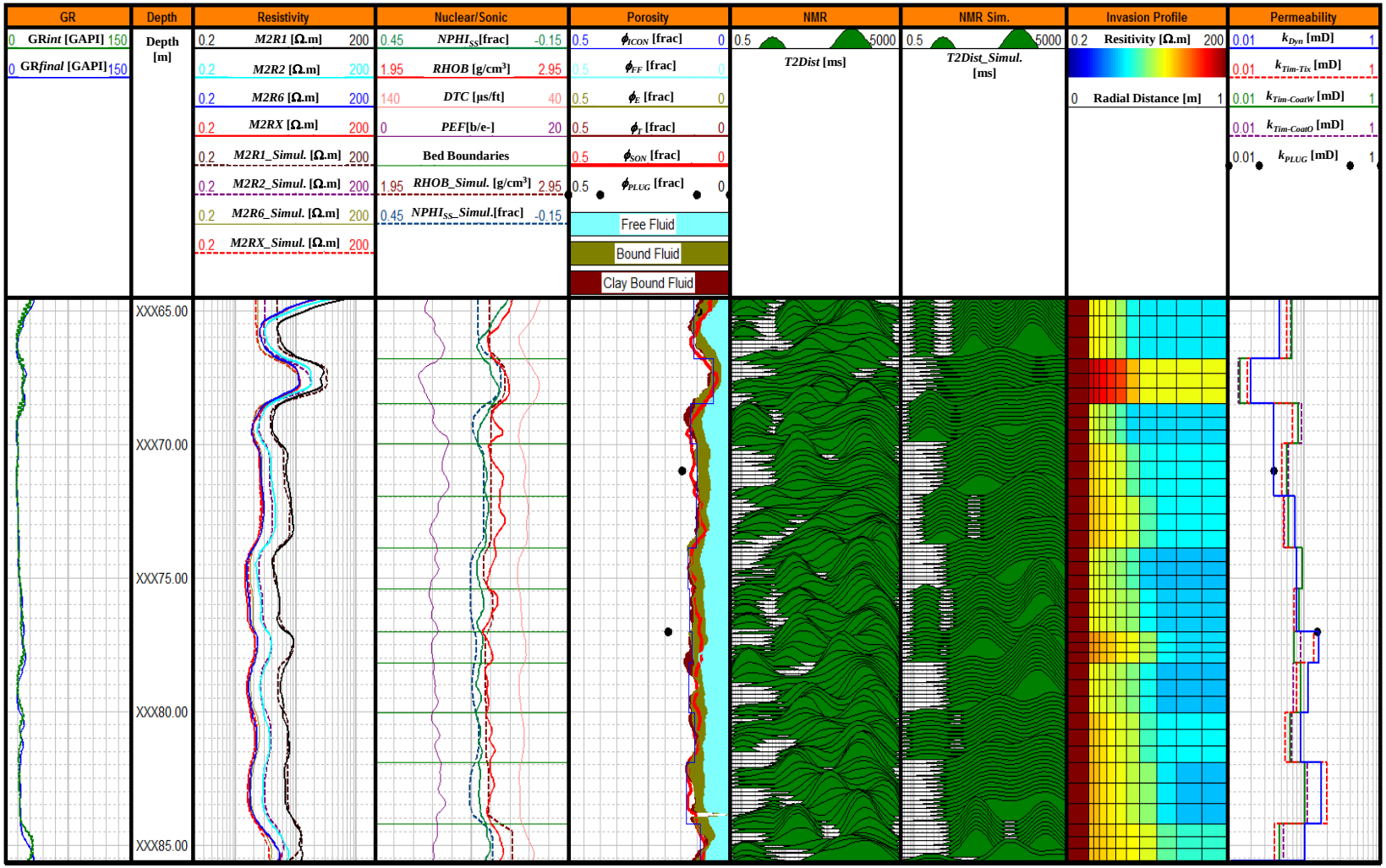
GR
Depth
Resistivity
Nuclear/Sonic
Porosity
NMR
NMR Sim.
Invasion Profile
Permeability
0 GRint [GAPI] 150
0 GRfinal [GAPI] 150
Depth [m]
0.2 M2R1 [Ω.m] 200
0.2 M2R2 [Ω.m] 200
0.2 M2R6 [Ω.m] 200
0.2 M2RX [Ω.m] 200
0.2 M2R1_Simul. [Ω.m] 200
0.2 M2R2_Simul. [Ω.m] 200
0.2 M2R6_Simul. [Ω.m] 200
0.2 M2RX_Simul. [Ω.m] 200
0.45 NPHISS[frac] -0.15
1.95 RHOB [g/cm3] 2.95
140 DTC [µs/ft] 40
0 PEF[b/e-] 20
Bed Boundaries
1.95 RHOB_Simul. [g/cm3] 2.95
0.45 NPHISS_Simul.[frac] -0.15
0.5 ϕICON [frac] 0
0.5 ϕFF [frac] 0
0.5 ϕE [frac] 0
0.5 ϕT [frac] 0
0.5 ϕSON [frac] 0
0.5 ϕPLUG [frac] 0
Free Fluid
Bound Fluid
Clay Bound Fluid
0.5 5000
T2Dist [ms]
0.5 5000
T2Dist_Simul. [ms]
0.2 Resitivity [Ω.m] 200
0 Radial Distance [m] 1
0.01 kDyn [mD] 1
0.01 kTim-Tix [mD] 1
0.01 kTim-CoatW [mD] 1
0.01 kTim-CoatO [mD] 1
0.01 kPLUG [mD] 1
XXX65.00
XXX70.00
XXX75.00
XXX80.00
XXX85.00

Figure 6.2: Results of dynamic simulations in Well **X** across a short depth section fully saturated with water. The well was drilled with OBM. Measurements were acquired after 9 days of OBM invading the formation. Dashed curves identify numerical simulations. Track 1: gamma-ray of the intermediate phase (green) and gamma-ray of the final phase (blue). Track 2: depth. Track 3: apparent resistivities with different depths of investigation (red, blue, aqua, dark blue and black), and simulated apparent resistivities (dashed red, dashed blue, dashed aqua, dashed dark blue and dashed black). Track 4: density (red), neutron porosity in sandstone units (green), sonic (light pink), PEF (purple), simulated density (dashed red), and simulated neutron porosity in sandstone units (dashed dark green). Track 5: computed sonic (Wyllie) porosity (red), porosity and porosity fractions estimated with NMR *T2* distributions (light blue, olive, and brown), interconnected porosity used in the simulations (blue), and core porosity (black dots). Track 6: NMR *T2* distributions. Track 7: numerical simulations of NMR *T2* distributions. Track 8: radial distribution of electrical resistivity from the simulations of mud-filtrate invasion. Track 9: core permeability (black dots), permeability used to perform dynamic simulations (blue), permeability estimated with Timur-Tixier's equation (dashed red), and permeability estimated with Timur-Coates' equation (dashed purple).

6.2 NMR SIMULATIONS AND FLUID SUBSTITUTION IN WELL X

Using dynamic simulation results, I performed fluid-substitution simulations in the NMR measurements. First, I simulated NMR *T2* distribution of the first time-lapse, which corresponds to the pre-invasion measurement (**Figure 6.1 –** track 7). To produce reliable results, the five midpoint measurements of each layer were averaged. The NMR fluid substitution entailed using simulated NMR *T2* distribution of the first run and properties estimated in the dynamic simulations such as irreducible water saturation and the closest borehole water saturation value after OBM invasion. **Figure 6.3** compares the NMR *T2* distributions before invasion, after invasion, and after fluid substitution.

Results of the fluid substitution on NMR measurements indicate the following:

- Microporosity signals, before and after invasion, are similar because fluid is immobile in this portion of the rock. The Sw_{irr} values assumed in NMR and dynamic simulations are similar. **Table 6.2** shows the comparison between Sw_{irr} used for each layer. Discrepancies between the two values exist because (1) the tools have different radial values of investigation and vertical resolution, and (2) NMR distribution was simulated based on an average between the five midpoint measurements of each layer.
- Because of OBM invasion, the free fluid peak changed between measurements. The free water peak in the first measurement corresponds to a bimodal distribution in the second measurement. The peak that presents values higher than 300 ms corresponds to the OBM that invaded the rock, and the peak that falls between 10 and 100 ms is the free water that remains in the formation. **Table 6.2** shows that exist a good agreement between the irreducible water saturation used to numerically simulate NMR and resistivity logs.

- After the OBM invasion, the free-water peak moved to lower values of *T2*. This effect occurs because the presence of OBM in the pore space decreases the free-water resonance space. The fluid-solid interaction effect starts to have more influence in the NMR relaxation than the bulk effect.

It is important to mention that the free-fluid region of the NMR *T2* distribution is extremely dependent on fluid saturation. The use of previously established parameters and/or cut-offs in complex reservoirs may produce abnormal permeability estimations.

	Sw_{irr} dynamic simulations [frac.]	**Sw_{irr} NMR simulations [frac.]**
Layer 1	0.25	0.15
Layer 2	0.20	0.20
Layer 3	0.25	0.30
Layer 4	0.25	0.1
Layer 5	0.25	0.2
Layer 6	0.25	0.29
Layer 7	0.25	0.20
Layer 8	0.17	0.13
Layer 9	0.25	0.1
Layer 10	0.25	0.22
Layer 11	0.16	0.06
Layer 12	0.25	0.27

Table 6.2: Comparison of irreducible water saturation after invasion used to simulate NMR and resistivity logs in Well **X.**

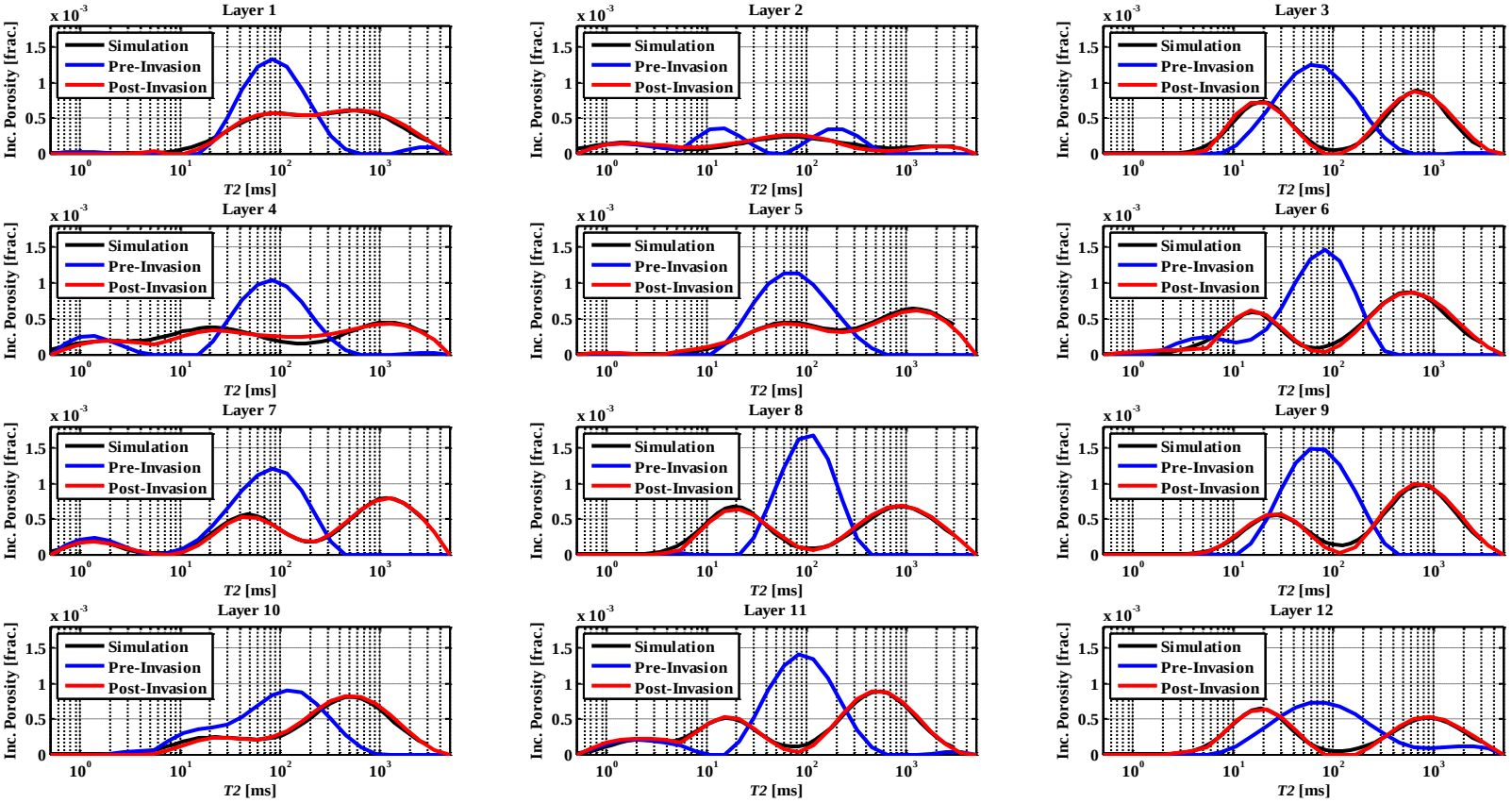

Figure 6.3: Results of NMR fluid substitution for the 12 layers included in the dynamic model Well **X**. Each panel shows the pre-invasion well-log NMR *T2* distribution (blue), post-invasion NMR *T2* distribution (red) and the simulation of the NMR T2 distribution after OBM invasion (black). To simulate the black curves, I first simulated the pre-invasion *T2* distribution; then I performed fluid substitution until an acceptable agreement between the post-invasion and the simulated *T2* distribution curves was reached.

Chapter 7: Summary and Conclusions

This final chapter summarizes the recommended best practices and conclusions for improving estimations of petrophysical properties from well logs in complex carbonate reservoirs. The new method was tested in a highly heterogeneous carbonate reservoir that contains layers with non-interconnected porosity. Suggestions for future research are provided at the end of the chapter.

7.1 Recommendations and Best Practices

The first step in petrophysical interpretation of complex carbonate reservoirs is to perform quality control and basic data evaluation. This initial evaluation comprises estimates of total porosity, sonic porosity, total water saturation, irreducible water saturation (in the presence of OBM), absolute permeability, and mineralogy. It is important to emphasize that, without core measurements, permeability estimations based on empirical equations and standard parameters are only qualitative in nature.

For the heterogeneous carbonate formations under consideration I recommend slower logging speeds to acquire high-resolution data with acceptable quality. Acquisition of advanced measurements, such as NMR and sonic logs, is also necessary for a complete interpretation of the formation. The NMR log helps identify complex pore space, analyze fluid distribution, and estimate absolute permeability. Additionally, sonic measurements are important in identifying regions that contain vuggy porosity.

Core plug acquisition should be planned to secure a good representation of all the rock types present in the reservoir. The acquisition and measurement of core plugs from only good quality rocks will bias the interpretation toward optimistic petrophysical results. With core measurements, a good depth match between well logs and core measurements is crucial. Using the results of this work, I recommend that the best

measurements for performing depth matching are well-log density total porosity combined with core plugs total porosity.

The next step in the petrophysical evaluation is to perform rock typing. **Table 3.1** shows the method for identifying the predominant type of porosity in each layer. Differences higher than 20% between total and sonic porosities are indicators of layers that contain vuggy porosity. Low values of resistivity and an NMR distribution that exhibits large porosity associated with relaxation times lower than 30 ms are indicators of a layer that contains microporosity. Regions that exhibit large variability in the bulk density are interpreted as laminated regions. In these regions, the mixing effect present in NMR measurement and the shoulder-bed effect in all the logs may obscure the identification of highly permeable layers. Each rock type was associated with a specific and internally consistent set of static and dynamic petrophysical properties correlated with underlying pore-size distributions. Petrophysical properties depend on the predominant type of porosity within each layer.

Finally, petrophysical properties used in each layer were validated with well-log simulations. Additional refinements in petrophysical properties were necessary to secure a good match between field data and simulations. In the oil-bearing zone of the reservoir, estimations of interconnected porosity and irreducible water saturation were performed with shoulder-bed effect corrections. Finally, permeability was assessed using the Timur-Tixier equation for each layer. In the fully water saturated zone, I quantified the effect of mud-filtrate invasion on apparent resistivity logs. By constructing a geologically consistent earth model, it was possible to numerically simulate and match resistivity and nuclear logs. Additionally, NMR simulations validated the presence of microporosity and OBM invasion into the formation. After performing these corrections, the estimation of

permeability values improved considerably compared to conventional well-log interpretations.

7.2 SUMMARY AND CONCLUSIONS

Heterogeneous carbonate formations can be evaluated using static and dynamic reservoir models that integrate geological information, well logs, and core data. The following salient conclusions stem from the work reported in this thesis:

- Rock classification is important in the petrophysical evaluation of this complex carbonate field. Rock classification is established based on the predominant type of porosity in each layer. Layers that contain mixtures of rock types are common.
- Integration of geological information, conventional well logs, NMR data, and core analysis is essential for constructing a reliable earth model. Without core measurements, accurate estimation of petrophysical properties is difficult, if not impossible to obtain.
- Integrated analysis of resistivity, NMR, nuclear, and sonic logs indicates that some layers include isolated porosity or microporosity, which can correspond to a significant fraction of total porosity.
- Many depth sections of the reservoir consist of thinly bedded and highly-laminated sequences that are difficult or impossible to interpret with conventional well logs.
- In the oil-bearing zone, accurate estimations of interconnected porosity and irreducible water saturations are crucial for production assessments. Shoulder-bed corrections are of paramount importance in making petrophysical estimations, in this case because of the high spatial heterogeneity of the field.

- Estimated interconnected porosity values range between total and sonic porosity, according to the rock type of the layer. Interconnected porosity was established to be close to sonic porosity in regions dominated by isolated vuggy porosity.
- Regions dominated by microporosity tend to exhibit high values of irreducible water saturation and, consequently, low resistivity values. Significant adjustments in irreducible water saturation values were necessary to match well logs with simulations in highly laminated regions.
- Within free-water regions, dynamic simulations were essential to quantify the effect of OBM invasion on apparent resistivity logs. Additional refinements of petrophysical parameters, based on core measurements, were necessary to reliable reproduce reservoir conditions.
- Low porosity and low permeability regions are associated with deeper OBM invasion. Two physical reasons are the basis for this behavior: 1) low-porosity zones have low pore volume for the same volume of rock, thus some filtrate that invades the formation sweeps a larger radius of rock than it would sweep high-porosity zones, whereas 2) the process of mudcake formation is less efficient in low-permeability regions.
- The free-fluid peak in *T2* distributions is extremely dependent on the non-wetting fluid that saturates the rock.
- Layers associated with microporosity/high irreducible water saturation exhibit a large pore volume located at *T2* values lower than 30 ms.
- Presence of layers thinner than the vertical resolution of the NMR tool and noise present in NMR field data may preclude reliable assessments of porosity and permeability.

- NMR logs should be used carefully for quantitative analysis in heterogeneous reservoirs, especially in highly-laminated formations.

Results obtained with this new interpretation method resulted in, on average, a 34% better agreement between permeability core measurements and well-log based permeability estimations.

7.3 Limitations of the Method

Although careful petrophysical analyses were performed on all available data, systematic errors can still persist in permeability estimations. The limitations of the method are associated with the vertical resolution of well-logging tools, the variable volumes of investigation between measurements, and the precise depth match between core plugs and well-log measurements. In highly laminated regions, precise permeability estimation cannot be attained due to the aforementioned reasons. Additionally, in regions having vuggy porosity, the precise amount of isolated porosity is difficult to estimate. This porosity description directly impacts permeability estimations.

7.4 Suggestions for Future Research and Method Limitations

The main objective of this thesis was to develop a petrophysical method for the interpretation for complex carbonate reservoirs exhibiting high spatial heterogeneity and presence of isolated porosity. Using the interpretation method developed in this thesis and the knowledge acquired from the exercise, one can perform further qualitative permeability analysis. Cross validation of estimations with core data is highly recommended.

For future work, it is advisable to integrate more advanced well logs into the interpretation. Multi-component induction and image logs can help in the identification of laminated regions. Elemental capture spectroscopy (ECS) measurements are important

for better estimating the mineralogy of the formation, thereby aiding in the construction of the earth model. In the oil-bearing zone of the reservoir, *T2-D* maps should be acquired at key points within the reservoir; *T2-D* maps may help to elucidate OBM invasion in regions where there is no resistivity contrast between OBM and formation fluid.

Further laboratory measurements are helpful in the reservoir interpretation process. NMR laboratory experiments should be conducted to improve effective medium theories and the impact of fluid saturation on final measurements. Finally, measurements of water saturation with the Dean-Stark method (1920) should be added to routine core analysis. Though the accuracy of the Dean-Stark method is low, the measurement does help petrophysicists in making quantitative evaluations of irreducible water saturation.

Appendix A: Forward NMR Simulation

This appendix describes the forward simulation of NMR *T1* and *T2* distributions, and *T1-T2*, *T1-D* and *T2-D* maps in the presence of arbitrary pore-size distributions and fluid saturations. The original Matlab code was written by Raúl Andrés Guevara-Torres and upgraded by former students of the formation evaluation research consortium group at The University of Texas at Austin.

A.1 *T1*, *T2,* AND DIFFUSIVITY

Longitudinal relaxation time (*T1*) and transversal relaxation time (*T2*) are the two magnetic relaxation times of fluids in porous media. The analytical equation for *T2* is described by

$$\frac{1}{T2} = \frac{1}{T2_B} + \rho_2 \frac{S}{V} + \frac{(\gamma \cdot G \cdot TE)^2 \cdot D}{12}, \tag{A.1}$$

where $T2_B$ is the bulk transverse relaxation time (fluid dependent), ρ_2 is the transverse surface relaxivity (rock dependent), *S/V* is the ratio of pore surface to pore volume (pore-body size dependent), γ is the gyromagnetic ratio for a hydrogen proton, *G* is the average magnitude of the DC magnetic field gradient over the entire sample, *TE* is inter-echo spacing in the Carr-Purcell-Meiboom-Gill (CPMG) sequence, and *D* is effective fluid diffusivity.

The longitudinal relaxation time is not dependent on diffusivity, hence the *T1* expression becomes

$$\frac{1}{T1} = \frac{1}{T1_B} + \rho_1 \frac{S}{V}, \tag{A.2}$$

where $T1_B$ is the bulk longitudinal relaxation time (fluid dependent) and ρ_l is the longitudinal surface relaxivity (rock dependent). Surface relaxivity in the fluid/fluid interface is negligible; however, in the fluid/solid interface the relaxivity has values that depend on fluid/rock pairs (Kenyon, 1997).

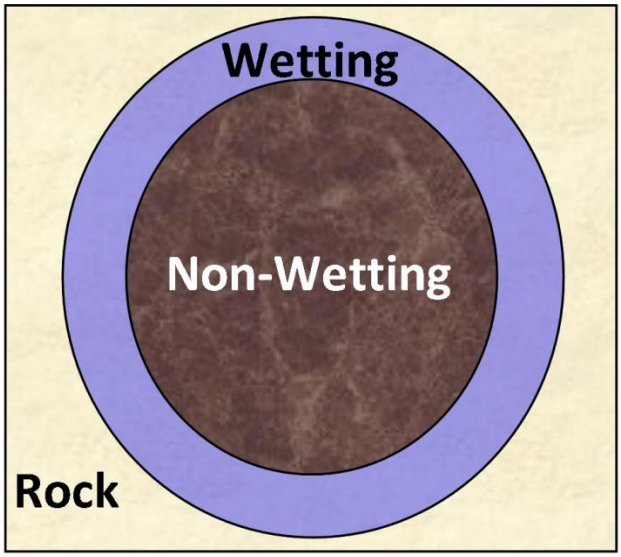

Figure A.1: Idealized pore with wetting and non-wetting phases.

A.2 NMR SIMULATION

Figure A.1 shows an idealized pore in a rock filled with wetting and non-wetting fluids. This pore has a specific surface relaxivity that depends on the wetting fluid/mineral pair, has a specific surface to volume ratio (*S/V*) that depends on the pore size, has a specific bulk relaxation time that depends on the saturating fluids, and has a diffusivity that depends mainly on the non-wetting fluid properties.

Given that a porous rock is composed of different sized pores, a log-Gaussian distribution was used to represent the pore-size distribution of the rock. Similarly,

because oil consists of a complex mixture of hydrocarbons, the log-Gaussian distribution was also used to represent the bulk relaxation time ($T1_B$ and $T2_B$) and the diffusivity. The probability density function *(p(x))* of a log-Gaussian distribution is represented by

$$p(x) = \frac{1}{\sigma\sqrt{2\pi}} exp\left(-\frac{(log(x) - log(\mu))^2}{2\sigma^2} \right), \qquad \text{(A.3)}$$

where x is replaced by r to calculate the pore size distribution, μ represents the predominant pore size of the rock, and σ describes the variability of the pore size distribution in this rock. High values of σ describe rocks with complex pore structures. **Equation A.3** was also applied to estimate the probability density function of the bulk relaxation time and the diffusivity coefficient of the non-wetting fluid.

Assuming spherical pore shapes, **equation A.1** for the wetting phase and with no diffusion effects can be written as

$$\frac{1}{T2} = \frac{1}{T2_B} + 3\rho_2 \frac{1}{r}. \qquad \text{(A.4)}$$

Because the non-wetting phase is not in contact with the paramagnetic material of the rock, the surface term can be neglected in the non-wetting phase analysis. **Equation A.4** indicates that for a given r there is a corresponding $T2$ (or $T1$). Rearranging this equation yields

$$r = \frac{3\rho_2}{\frac{1}{T2} - \frac{1}{T2_B}}. \qquad \text{(A.5)}$$

By examining this equation one can argue that the number of pores in a given porosity interval must be proportional to the *T2* amplitude of that interval. A transformation to a normalized *T2* distribution is desired for a normalized pore-size distribution. The equation for this transformation is given by

$$p(T2)\cdot\Delta(T2)=p(r)\cdot\Delta(r). \tag{A.6}$$

By rearranging this equation and transforming the given interval in an infinitesimal interval, the equation can be expressed as

$$p(T2)=p(r)\cdot\frac{dr}{dT2}. \tag{A.7}$$

Replacing **equations A.3** and **A.5** in **equation A.7** yields

$$p(T2)=\frac{1}{\sigma\sqrt{2\pi}}exp\left(-\frac{\left(log\left(\frac{3\rho_2}{\left(1/T2-1/T2_B\right)}\right)-log(\mu)\right)^2}{2\sigma^2}\right)\cdot\left(3\rho_2\left(\frac{T2_B}{\left(T2-T2_B\right)}\right)^2\right) \tag{A.8}$$

This equation is the *T2* distribution of the wetting phase in the presence of only surface effects. Similar distributions must be calculated for bulk relaxation time and diffusivity effects, when applicable. The final *T2* distribution of the wetting phase is represented by the multiplication of the two effects, and the final expression of the *T2* distribution of the wetting phase (p_w) can be written as

$$p_W(T_2,D)=\sum_{T2_b} p(r)\cdot p(T2_b)\cdot\frac{dr}{dT2}\ , \qquad \text{(A.9)}$$

where $p(r)$ is the log-normal distribution of the pore size distribution and $p(T2_B)$ is the log-normal distribution of the bulk relaxation time. The similar distribution for the non-wetting phase (p_{NW}) is given by

$$p_{NW}(T_2,D)=\sum_{T2_b} p(T2_b)\cdot\frac{dT2_b}{dT2}\ . \qquad \text{(A.10)}$$

Finally, the one-dimensional *T2* distribution (*T2*) is the sum of the all the effects due to an arbitrary pore-size distribution and arbitrary fluid saturations. The final expression is expressed by

$$T2=\sum_{i=1}^{N} HI_i\cdot S_i\cdot p_i(T_2,D)\ , \qquad \text{(A.11)}$$

where *HI* is hydrogen index, *S* is fluid saturation, and *p* is log-normal distribution of the phases. Rearranging **equation A.2**, and applying the same procedure as described above, a similar expression for *T1* distribution is obtained.

This code was also written to produce 2D maps (*T1-T2, T2-D*, and *T1-D*). The methods for calculating the distributions for wetting and non-wetting phases are similar, except that in 2D maps *T2/T1* decays are calculated for different log-normal distributions of diffusion *p(D).* The final *T2-D* map is expressed by

$$[T_2,D]_{Map}=\sum_{i=1}^{N} HI_i\cdot S_i\cdot p_i(T_2,D)\cdot p_i(D)\,. \qquad \text{(A.12)}$$

Appendix B: Mixing Effects on NMR Logs

B.1 INTRODUCTION

The NMR *T2* distribution is used in formation evaluation to estimate total porosity, to characterize the pore space, and to discriminate fluids saturating a porous rock. Additionally, reservoir permeability values can be estimated with empirical relations based on the NMR *T2* distribution (Timur, 1969; Coates *et al*., 1991; Kenyon *et al*., 1988). These estimations provide a consistent permeability index in homogeneous reservoirs that are completely saturated with water. However, the estimations become inaccurate when applied to heterogeneous reservoirs. Well-log NMR measurements will show a mixed NMR *T2* distribution in reservoirs with laminations that are thinner than the vertical resolution of the measurement. The mixing of rock types or fluid saturation in the volume of investigation of the measurement will preclude a reliable assessment of the petrophysical properties of the rock.

Minh and Sundararaman (2011) described the NMR mixing effect on thin shaly/sand laminated reservoirs. They evaluated a reservoir that showed a false bimodal *T2* distribution due to thin laminations. The authors were able to separate the porosity components of different rock types; they evaluated each rock separately, providing a consistent petrophysical interpretation of the reservoir.

This appendix extends Minh and Sundararaman's (2011) study and analyzes more complex cases. Using laboratory NMR *T2* measurements and numerical NMR simulations, I analyzed cases where the predominant NMR peaks of different rock types have similar *T2* responses. In laboratory samples, I analyzed rocks with different permeability-porosity conditions. In synthetic cases, I simulated the effect of rocks with different lithologies, fluid compositions, and variable signal-to-noise ratios. Results show

that NMR data should be used cautiously for quantitative petrophysical evaluation of heterogeneous reservoirs.

B.2 METHOD

Figure B.1 compares a core photograph of a laminated region in the evaluated carbonate reservoir, the NMR *T2* distribution for this region, and the vertical resolution of the NMR tool. Dark core regions represent high-permeability production zones while light regions represent low-permeability zones. Observations of the image show that the bimodal response of the NMR *T2* distribution corresponds to an average of different rock types on the same volume of investigation of the NMR tool. This bimodal signal causes an erroneous relationship between mobile and bound fluid, resulting in inaccurate permeability estimation in this laminated region. Hence, based on the *T2* distribution, the permeability of the homogeneous components cannot be estimated separately.

To study the mixture effect on NMR data, both laboratory measurements and synthetic data were analyzed. In laboratory experiments, NMR *T2* distributions were measured separately for each homogeneous rock sample. Next, I grouped the two samples and measured the NMR response of the mixed rock. In synthetic cases, I numerically simulated the NMR response of homogeneous rocks. Once the *T2* distributions were obtained, the corresponding time decay responses were calculated and the mixed synthetic rocks were analyzed numerically. These simulations are based on the NMR numerical simulation method described in Appendix A. In both cases, the estimated petrophysical properties of the mixed rocks were compared to the measured properties of homogeneous samples.

From these experiments, one can assess the impact of mixed rocks on NMR measurements and the effect of the mixture on porosity/permeability estimations.

Equation B.1 shows that the echo amplitude time decay of the mixture (ϕ_T) is arithmetically weighted by the echo amplitude time decay of each homogeneous component of the system (ϕ_{Ri}), namely,

$$\phi_T = \sum_{i=1}^{n} FV_{Ri} \cdot \phi_{Ri} \quad , \tag{B.1}$$

where FV_{Ri} is the fractional pore volume and the subscript Ri identifies each homogeneous component of the mixture. Because NMR magnetization amplitude decay is calibrated to a give porosity, the porosity of the mixture corresponds to the weighted arithmetic average porosity of the homogeneous rocks involved.

Next, I use the Timur-Coates equation (**Equation B.2**) to estimate the permeability of the mixed rock, namely,

$$k = A \cdot \left(\frac{FF}{BF_T} \right)^B \cdot \phi_T{}^C , \tag{B.2}$$

where k is permeability of the mixture in millidarcies, ϕ_T is total porosity in percentage, and (FF/BF_T) is the ratio between free fluid and total bound fluid. The free fluid/bound fluid ratio is based on a theoretical cutoff (Coates *et al*., 1991) that depends on the evaluated reservoir; A, B, and C are constants determined by the permeability measured in homogeneous samples.

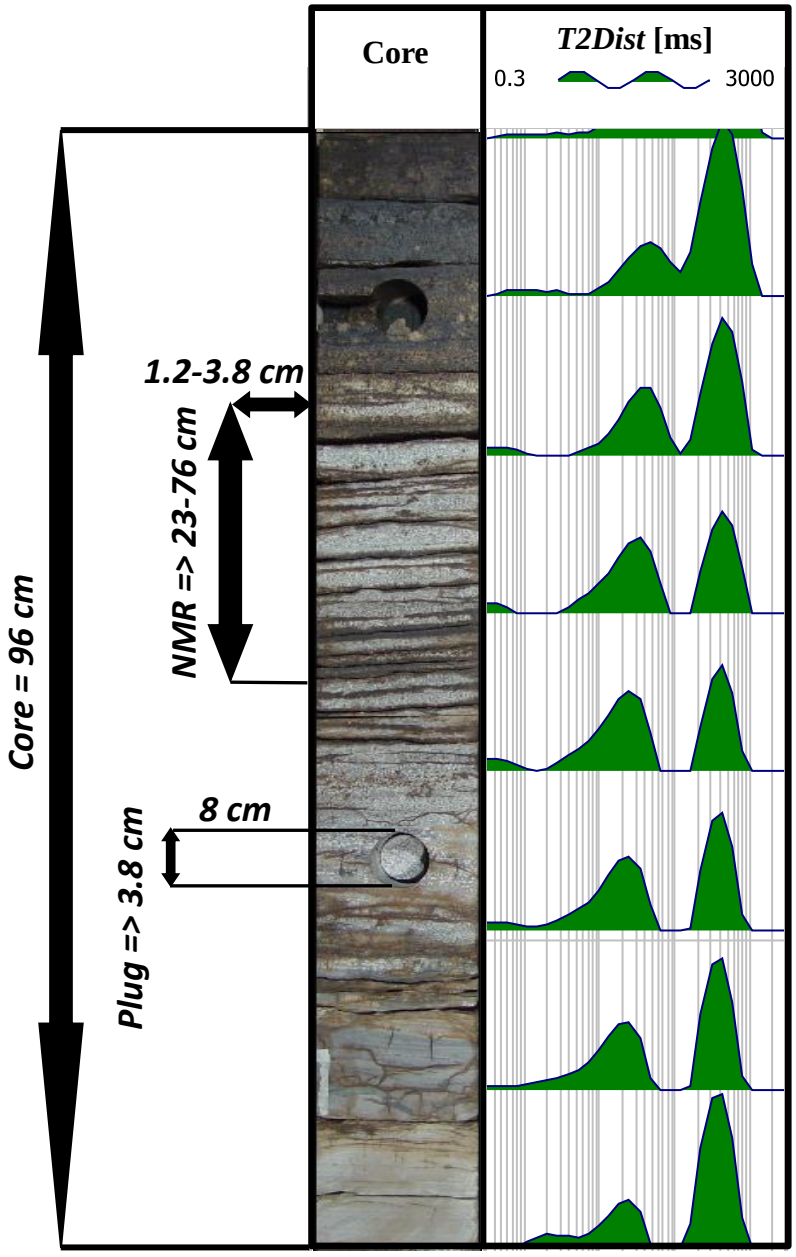

Figure B.1: Comparison of a core photograph, the NMR *T2* distribution, and the vertical resolution of the NMR measurement. This zone corresponds to a laminated region of a carbonate reservoir. The NMR log lacks the vertical resolution necessary to reproduce the laminations present in this core sample. The NMR *T2* distribution shows a bimodal behavior which may be attributed to the presence of a mixed rock within the volume of investigation of the NMR tool.

B.3 RESULTS AND DISCUSSIONS

Table B.1 summarizes all the parameters used to perform the numerical simulations; it describes all the results and comparisons between homogeneous samples and the mixed rocks. Descriptions and results of those experiments are listed below.

B.3.1 Laboratory Measurements

Measurement 1: NMR *T2* distributions were measured of two homogeneous samples and their mixture. The homogeneous samples are grainstones with different porosities and similar permeabilities (**Table B.1**). **Figure B.2** shows the *T2* distribution, decay, and photographs of the two homogeneous samples and their mixture. The porosity of the mixture is an average porosity between the two homogeneous samples. Likewise the porosity component in the NMR decay of the mixture is an average between the two homogeneous samples. This observation was used when numerically simulating the NMR response of the mixture of rocks.

Measurement 2: Next, NMR *T2* responses of two homogeneous samples and their mixture were measured. In this case, there are two dolostone samples, one with high porosity and permeability and the other with average porosity and permeability (**Table B.1**). **Figure B.3** shows the *T2* distribution, decay, and photographs of the two homogeneous samples and their mixture. The estimated permeability of the mixture using the Timur-Coates equation shows a value close to the geometric mean of the homogeneous samples (**Table B.1**). It is emphasized that the geometric mean value of a data set is smaller than its arithmetic mean value. Thus, using **equation B.2** in a mixed rock will emphasize the low-permeability rock portion of the mixture. The geometric-mean permeability (k_{GM}) of each homogeneous component of the system (k_{RI}) is given by

$$k_{GM} = exp\left(\sum_{i=1}^{n} FV_{Ri} \cdot ln\left(k_{Ri}\right) \right). \qquad \text{(B.3)}$$

Case	Method	Sample	Lithology	ϕ_T [%]	k [mD]	k_{GM} [mD]	Sw_{irr} [%]	FV_{Ri} [%]	Cutoff (*FF/BFT*) [ms]	*A, B, C*
1	Laboratory (**Figure 2**)	Sample 7751	Limestone	15.85	19.92	-	-	50	-	-
		Sample 7757	Limestone	25.55	14.35	-	-	50	-	-
		Mixture	Limestone	20.67	15.00 *	16.91	-	-	100	10000, 1.28, 4.22
2	Laboratory (**Figure 3**)	Sample 7768	Dolomite	36.63	1568.92	-	-	50	-	-
		Sample 7779	Dolomite	17.58	20.77	-	-	50	-	-
		Mixture	Dolomite	27.11	270.00 *	180.51	-	-	100	10000, 1.28, 4.22
3	Synthetic (**Figure 4**)	Sand	Sand	11.00	26.03 *	-	-	70	50	10000, 2, 4
		Shale	Shale	8.00	5.24E-17 *	-	-	10	50	10000, 2, 4
		Limestone	Limestone	5.00	5.66E-05 *	-	-	20	50	10000, 2, 4
		Mixture	Mixture	8.00	1.48 *	0.03	-	-	50	10000, 2, 4
4	Synthetic (**Figure 5**)	Sample 1	Limestone	20.00	15.00 *	-	60	50	100	10000, 2, 4
		Sample 2	Limestone	20.00	442.00 *	-	15	50	100	10000, 2, 4
		Mixture	Limestone	20.00	44.00 *	81.42	37	-	100	10000, 2, 4
5	Synthetic (**Figure 6**)	Sample 1	Sand	20.00	264.00 *	-	20	50	30	10000, 2, 4
		Sample 2	Limestone	20.00	239.00 *	-	20	50	100	10000, 2, 4
		Mixture	Mixture	20.00	299 and 56 *	251.19	20	-	30 and 100	10000, 2, 4
6	Synthetic (**Figure 7**)	Original	Sand	20.00	13.10 *	-	-	-	30	10000, 2, 4
		Noise = 20% of total porosity	Sand	19.03	7.70 *	-	-	-	30	10000, 2, 4
		Noise = 50% of total porosity	Sand	18.50	6.02 *	-	-	-	30	10000, 2, 4

Table B.1: Rock-fluid properties of homogeneous rocks and mixtures. *Estimated permeability using the Timur-Coates equation (Coates *et al*., 1991).

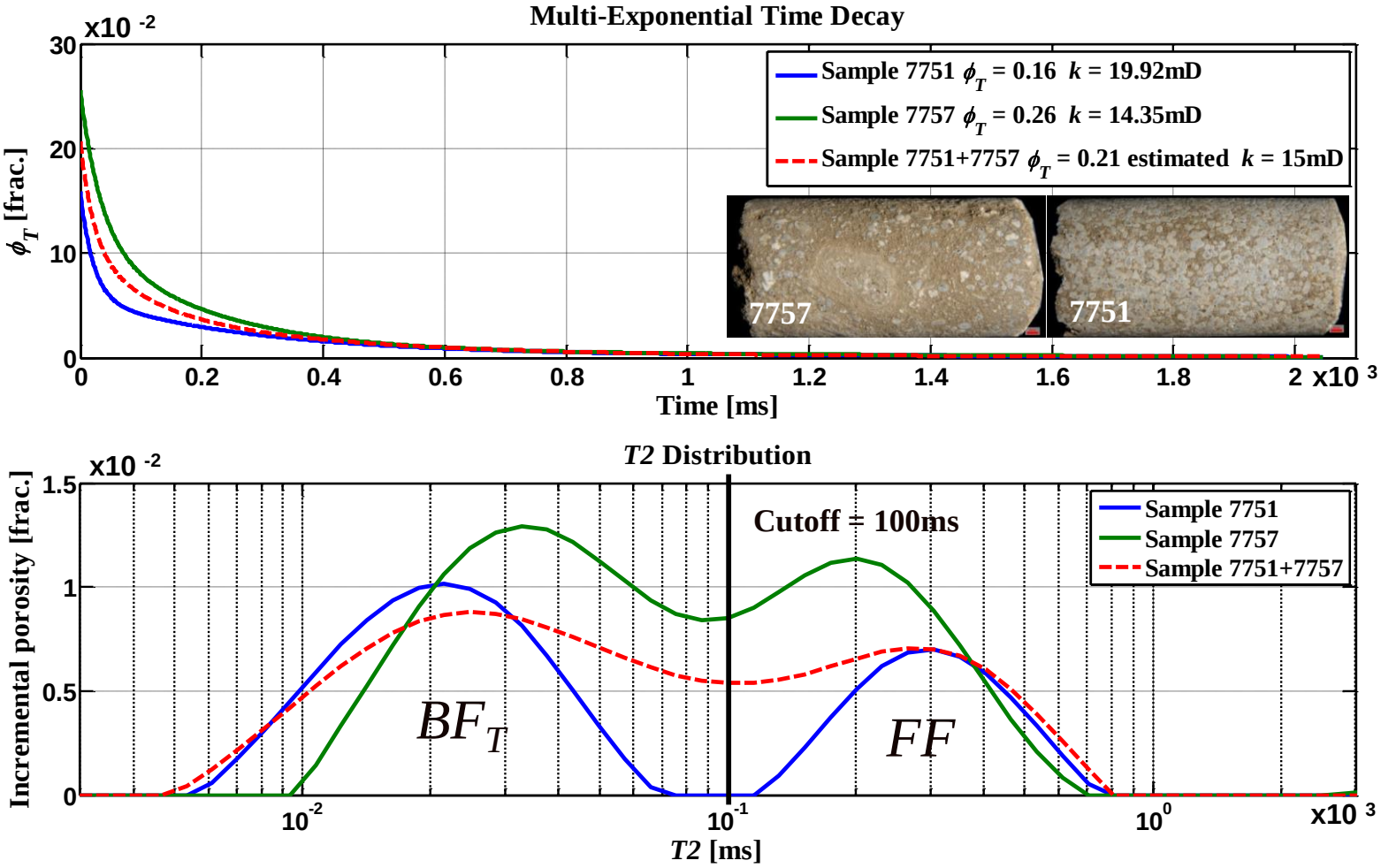

Figure B.2: Results of NMR laboratory measurements of two limestone samples with different porosity and similar permeability and the mixture of these two samples (top: multi-exponential decay, bottom: *T2* distribution).

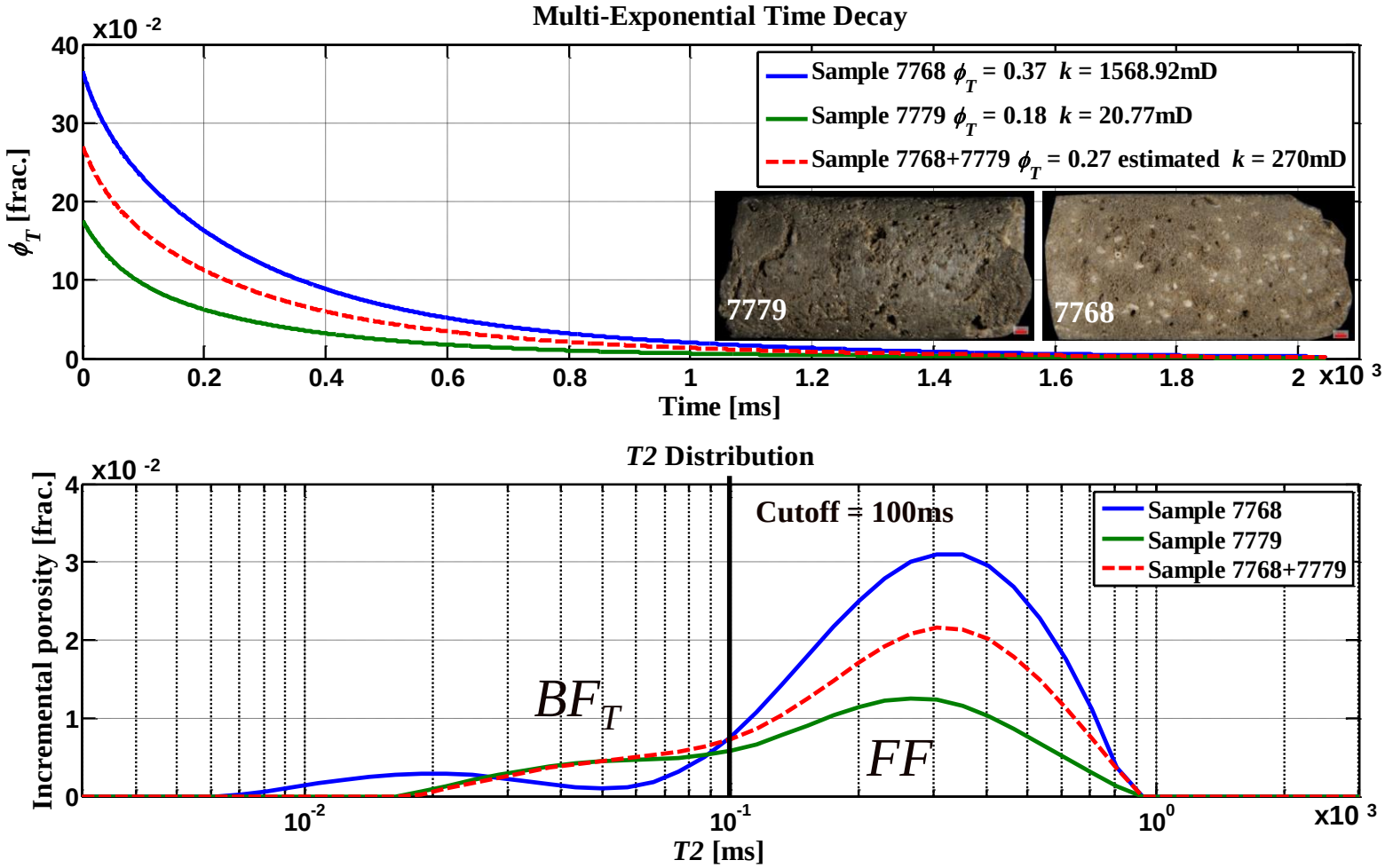

Figure B.3: Results of NMR laboratory measurements of two dolomite samples with different porosity and different permeability and the mixture of these two samples (top: multi-exponential decay, bottom: *T2* distribution).

B.3.2 Synthetic Cases

Synthetic Case 1: I simulated a trimodal pore-size distribution based on one NMR-log sample. One stacked depth measurement of this NMR sample corresponds to a mixture of a permeable sandstone layer with impermeable carbonate and clay layers (**Table B.1**). **Figure B.4** shows the *T2* distribution, the time decay sequences, and the core photograph of the evaluated zone. In this example, applying the Timur-Coates equation to the measured *T2* distribution resulted in a low permeability value, characterizing this region as a non-producing zone. However, once I decomposed the spectrum into sand, shale, and carbonate parts, it was clear that the sand portion had a relatively high permeability and corresponded to 70% of the investigated volume. Consequently, I conclude that the sandstone portion of the measurement represents a potential producing zone.

Synthetic Case 2: I then simulated a mixture of two rocks having different amounts of irreducible water saturation (Sw_{irr}), while the other petrophysical properties remained similar (**Table B.1**). This amount of Sw_{irr} is directly correlated to the microporosity present in the rock (Diniz-Ferreira and Torres-Verdín, 2012). **Figure B.5** shows the *T2*-D maps of the two rock types and the mixture. Once again, the permeability value of the mixture was underestimated due to the effect of the low-permeability sample on the measurement. Consequently, even if the *T2* distribution indicates low-permeability intervals, the decomposition of the spectrum into homogeneous rocks shows that the interval can be a producer.

Synthetic Case 3: I also simulated a mixture of sandstone and limestone with similar petrophysical properties (**Table B.1**). **Figure B.6** shows the *T2*-D maps of the two rock types and the mixture. Both homogeneous rocks showed a good permeability for the

applied cutoffs (30 ms for the sandstone and 100 ms for the limestone). However, implementation of the limestone cutoff in the mixture underestimated the permeability.

Synthetic Case 4: Gaussian noise was added to the NMR decay of a sandstone rock (**Table B.1**). **Figure B.7** compares the NMR response of the original data to the NMR response of noisy data. The added noise corresponds to 20% and 50% of the total porosity of the sample. High noise in the data transformed the two peaks of the original *T2* distribution into a single peak. Permeability and porosity were also underestimated in the noisy data. Thus, interpretation of low signal-to-noise ratio data may provide inaccurate petrophysical values.

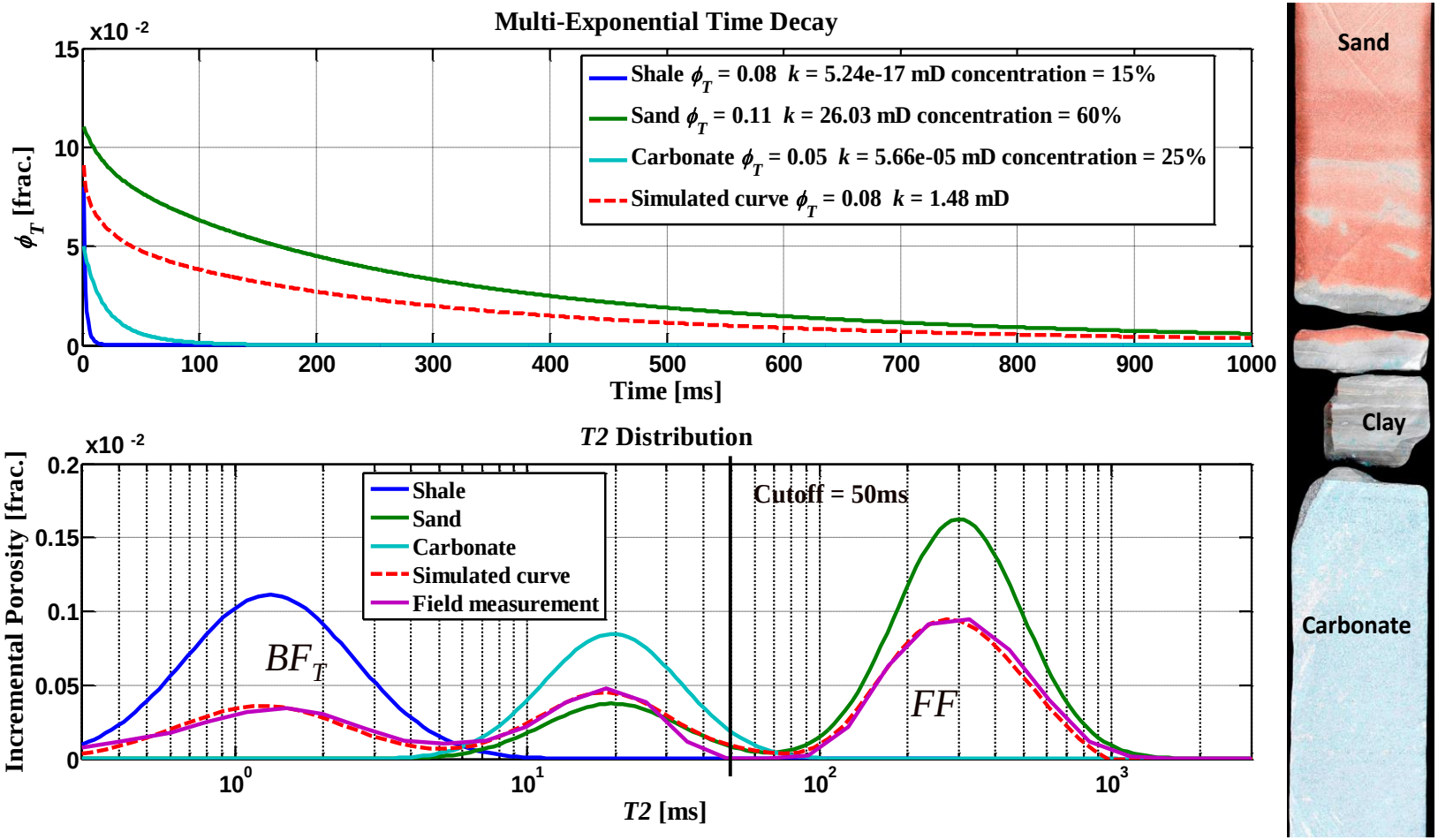

Figure B.4: Results of NMR simulation of a composite of three different rock types sandstone, clay, and limestone (top: multi-exponential decay, bottom: *T2* distribution).

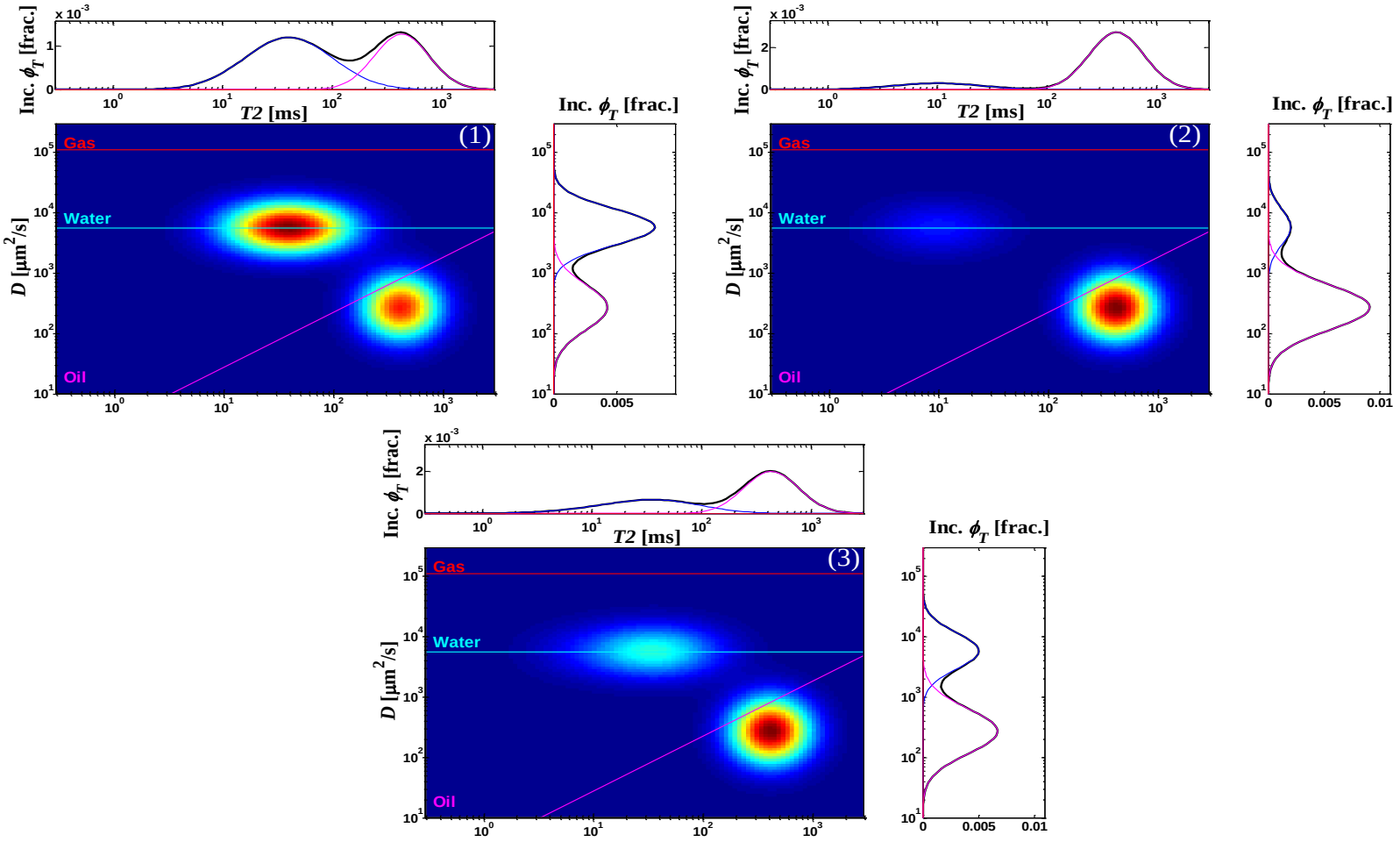

Figure B.5: Results of NMR numerical simulations for two different rocks with the same petrophysical properties, except for the amount of porous space related to microporosity. (1) Limestone with $Sw_{irr} = 0.60$, (2) Limestone with $Sw_{irr} = 0.15$, and (3) Mixture.

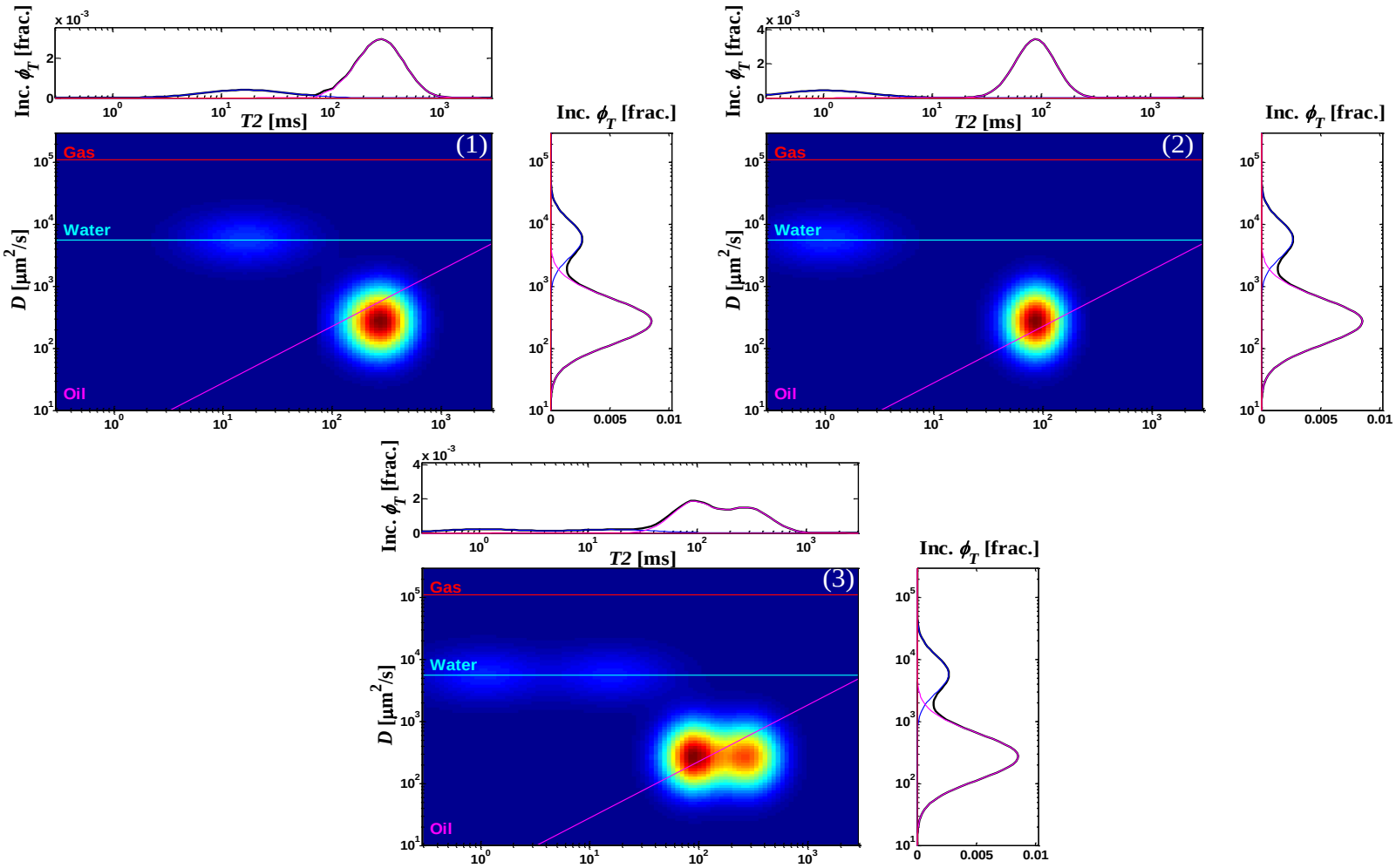

Figure B.6: Results of NMR numerical simulations for two rocks having the same petrophysical properties except for the mineral composition. (1) Limestone, (2) Sandstone, and (3) Mixture.

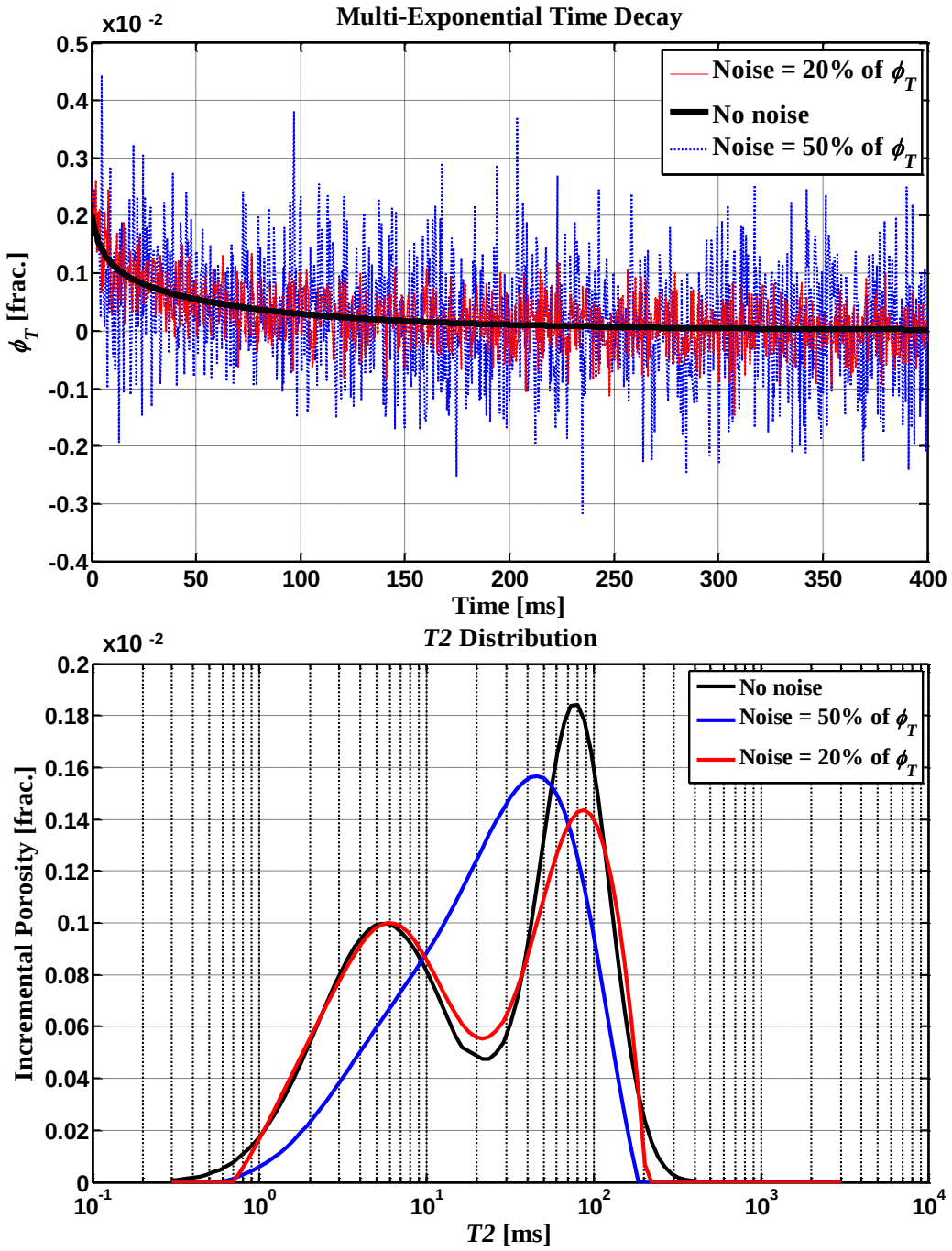

Figure B.7: Effect of noise on NMR measurements. Original data without zero-mean Gaussian noise (black). Original data with Gaussian random noise [maximum noise equal to 20% of the total porosity (blue)]. Original data with Gaussian random noise [maximum noise equal to 50% of the total porosity (red)].

B.4 CONCLUSION

An intricate pore space in a rock may not be the only factor that leads to a complex NMR *T2* distribution. Presence of multi-modal NMR *T2* distributions is also consistently related to mixtures of rock types and variations in fluid composition in the NMR volume of investigation. In addition to this problem, the NMR log commonly exhibits noise due to adverse measurement conditions in the wellbore. As a consequence, quantitative estimations from NMR data tend to be inaccurate in the presence of spatially heterogeneous reservoirs and/or noise.

Interpretation of the NMR *T2* distribution is difficult in formations that contain mixtures of rock types within the same volume of investigation of the NMR tool. Based on the analyzed cases, I draw the following conclusions:

- The total porosity and porosity components in the NMR decay of a mixture of rocks correspond to the fractional weighted arithmetical average of the porosity of each homogeneous rock in the mixture.
- Using the Timur-Coates equation in a mixture of rock will underestimate the permeability of the homogeneous good-quality component. This estimated permeability for the mixture yields results similar to the fractional weighted geometrical average of the system. Using the geometrical average leads to the conclusion that low-quality rocks have the largest influence in the final permeability estimation of the mixture.
- The theoretical *T2* cutoffs for homogeneous rocks cannot be accurately applied in regions with complex lithology. Applying a particular cutoff for a mixture of rocks will either underestimate or overestimate permeability, depending on the applied cutoff.

- In a mixture of rocks or in the presence of variation of fluid composition, two predominant *T2* peaks of the homogeneous rock may be closely spaced, giving rise to a broadened *T2* distribution. In these cases, the spectrum of each rock cannot be assessed separately, and the interpretation of the mixed spectrum is difficult.
- Estimation of petrophysical properties becomes even more difficult in the presence of a low signal-to-noise ratio. This thesis showed that the inversion of a low signal-to-noise-ratio decay transformed a two-peak distribution into a one-peak, broadened distribution. Under such conditions, the porosity and permeability estimated from noisy data will be underestimated.

Quantitative evaluation of NMR logs in heterogeneous reservoirs or from noisy data sets warrants a cautious approach. The mixture of rocks in the same volume of investigation of the NMR tool can give rise to a biased *T2* distribution that contains signal of homogeneous components. This biased distribution can lead to an erroneous interpretation of the data.

Permeability estimation is most affected by mixing effects, and the direct use of the Timur-Coates equation in heterogeneous reservoirs may yield inaccurate results. Advanced interpretation methods such as numerical simulation of the *T2* distribution, decomposition of the *T2* spectrum, core analysis, and shoulder-bed effects corrections can help to improve the estimation of petrophysical properties.

Appendix C: Extended Tables

This appendix contains detailed summary tables for the initial estimate and the final set of parameters used in numerical simulations. The tables below describe the data for the three evaluated wells, Well **H**, Well **Γ**, and Well **X**.

	Initial Estimate						Final Parameters	
Layer number	ϕ_{ICON} **[frac.]**	Sw_{irr} **[frac.]**	**Calcite [frac.]**	**Dolomite [frac.]**	**Quartz [frac.]**	**Clay + Anhydrate [frac.]**	ϕ_{ICON} **[frac.]**	Sw_{irr} **[frac.]**
1	0.070	0.206	0.442	0.253	0.173	0.063	0.040	0.144
2	0.079	0.133	0.421	0.241	0.165	0.064	0.080	0.160
3	0.091	0.097	0.429	0.245	0.168	0.063	0.065	0.180
4	0.093	0.093	0.418	0.239	0.163	0.066	0.087	0.108
5	0.098	0.086	0.423	0.242	0.166	0.063	0.076	0.092
6	0.120	0.059	0.499	0.238	0.082	0.068	0.089	0.118
7	0.142	0.039	0.450	0.215	0.074	0.063	0.169	0.065
8	0.140	0.039	0.437	0.209	0.072	0.073	0.190	0.071
9	0.134	0.046	0.628	0.132	0.016	0.016	0.158	0.208
10	0.130	0.054	0.351	0.273	0.117	0.055	0.165	0.099
11	0.127	0.050	0.354	0.276	0.118	0.056	0.156	0.078
12	0.126	0.049	0.355	0.276	0.118	0.056	0.154	0.071
13	0.122	0.061	0.351	0.273	0.117	0.055	0.165	0.050
14	0.106	0.103	0.663	0.133	0.012	0.016	0.135	0.097
15	0.086	0.150	0.736	0.148	0.013	0.026	0.046	0.261
16	0.112	0.089	0.579	0.226	0.042	0.028	0.095	0.078
17	0.127	0.052	0.580	0.226	0.042	0.029	0.093	0.065
18	0.091	0.079	0.580	0.226	0.042	0.028	0.093	0.078
19	0.065	0.114	0.598	0.233	0.044	0.037	0.068	0.108
20	0.098	0.074	0.376	0.376	0.065	0.039	0.104	0.087
21	0.122	0.058	0.200	0.200	0.200	0.239	0.112	0.108
22	0.123	0.064	0.623	0.151	0.041	0.040	0.115	0.086
23	0.122	0.059	0.633	0.156	0.049	0.041	0.115	0.133
24	0.121	0.052	0.623	0.151	0.041	0.040	0.115	0.048
25	0.128	0.048	0.658	0.137	0.033	0.039	0.093	0.114
26	0.150	0.050	0.399	0.382	0.033	0.043	0.108	0.068

27	0.154	0.047	0.352	0.338	0.029	0.039	0.203	0.118
28	0.128	0.057	0.594	0.124	0.030	0.048	0.173	0.092
29	0.106	0.091	0.383	0.298	0.128	0.081	0.091	0.185
30	0.091	0.189	0.392	0.305	0.131	0.082	0.070	0.144
31	0.089	0.136	0.505	0.221	0.090	0.023	0.142	0.088
32	0.058	0.212	0.568	0.248	0.101	0.014	0.049	0.192
33	0.041	0.297	0.588	0.257	0.104	0.022	0.017	0.377
34	0.021	0.436	0.583	0.255	0.103	0.013	0.025	0.234
35	0.017	0.713	0.384	0.375	0.157	0.027	0.017	0.678
36	0.020	0.378	0.461	0.381	0.094	0.014	0.011	0.590
37	0.041	0.285	0.459	0.379	0.094	0.023	0.015	0.494
38	0.050	0.251	0.461	0.381	0.094	0.014	0.011	0.564
39	0.075	0.145	0.417	0.345	0.085	0.020	0.099	0.093
40	0.086	0.116	0.460	0.250	0.093	0.026	0.120	0.086
41	0.079	0.138	0.497	0.270	0.100	0.026	0.057	0.176
42	0.091	0.104	0.463	0.252	0.093	0.026	0.116	0.078
43	0.102	0.096	0.452	0.246	0.091	0.034	0.135	0.058
44	0.089	0.154	0.473	0.257	0.095	0.026	0.099	0.088
45	0.039	0.418	0.360	0.325	0.193	0.037	0.036	0.245
46	0.019	0.255	0.065	0.750	0.107	0.010	0.019	0.504
47	0.039	0.456	0.405	0.352	0.099	0.030	0.063	0.164
48	0.072	0.153	0.393	0.342	0.096	0.028	0.091	0.187
49	0.085	0.115	0.220	0.498	0.094	0.027	0.110	0.234
50	0.100	0.070	0.395	0.343	0.096	0.025	0.091	0.164
51	0.110	0.058	0.399	0.267	0.169	0.019	0.127	0.109
52	0.108	0.054	0.401	0.268	0.169	0.028	0.123	0.071
53	0.096	0.078	0.414	0.277	0.175	0.009	0.074	0.102
54	0.067	0.131	0.424	0.284	0.179	0.016	0.053	0.160
55	0.044	0.325	0.378	0.341	0.203	0.030	0.027	0.287
56	0.074	0.131	0.609	0.223	0.048	0.022	0.068	0.109
57	0.094	0.088	0.591	0.217	0.047	0.030	0.093	0.104

Table C.1: Initial and final set of properties used in static numerical simulations in Well **H**.

	Initial Estimate						Final Parameters	
Layer number	**ϕ_{ICON} [frac.]**	**Sw_{irr} [frac.]**	**Calcite [frac.]**	**Dolomite [frac.]**	**Quartz [frac.]**	**Clay + Anhydrate [frac.]**	**ϕ_{ICON} [frac.]**	**Sw_{irr} [frac.]**
1	0.055	0.254	0.308	0.385	0.077	0.177	0.050	0.534
2	0.044	0.303	0.318	0.398	0.080	0.185	0.025	0.630
3	0.043	0.748	0.318	0.398	0.080	0.177	0.024	0.206
4	0.055	1.000	0.315	0.394	0.079	0.181	0.033	0.751
5	0.040	0.662	0.305	0.382	0.076	0.177	0.057	0.341
6	0.040	0.329	0.372	0.465	0.093	0.038	0.030	0.275
7	0.044	0.300	0.362	0.452	0.090	0.044	0.055	0.111
8	0.046	0.272	0.370	0.463	0.093	0.038	0.035	0.147
9	0.039	0.251	0.368	0.460	0.092	0.039	0.039	0.286
10	0.027	0.298	0.375	0.469	0.094	0.038	0.022	0.627
11	0.026	0.403	0.368	0.460	0.092	0.045	0.039	0.228
12	0.030	0.620	0.369	0.463	0.093	0.038	0.039	0.253
13	0.036	0.837	0.348	0.435	0.087	0.083	0.044	0.688
14	0.035	0.591	0.354	0.442	0.088	0.084	0.031	0.302
15	0.037	0.442	0.362	0.449	0.092	0.083	0.031	0.519
16	0.030	0.833	0.354	0.442	0.088	0.093	0.031	0.243
17	0.048	1.000	0.329	0.411	0.082	0.125	0.052	0.698
18	0.038	1.000	0.339	0.424	0.085	0.125	0.024	0.820
19	0.033	1.000	0.329	0.411	0.082	0.125	0.052	0.698
20	0.033	0.743	0.333	0.416	0.083	0.129	0.040	0.429
21	0.060	0.686	0.342	0.428	0.086	0.125	0.017	0.815
22	0.063	0.493	0.335	0.419	0.084	0.128	0.035	0.525
23	0.075	0.299	0.370	0.210	0.261	0.104	0.047	0.085
24	0.082	0.216	0.360	0.204	0.253	0.112	0.071	0.171
25	0.096	0.147	0.291	0.165	0.205	0.243	0.088	0.097
26	0.093	0.101	0.296	0.168	0.209	0.251	0.076	0.069
27	0.086	0.097	0.307	0.175	0.216	0.243	0.052	0.159
28	0.087	0.116	0.319	0.181	0.225	0.245	0.024	0.272
29	0.067	0.143	0.315	0.179	0.222	0.243	0.034	0.259
30	0.048	0.172	0.303	0.172	0.213	0.248	0.061	0.085
31	0.024	0.251	0.351	0.295	0.268	0.067	0.015	0.730
32	0.030	0.503	0.342	0.288	0.261	0.067	0.036	0.576
33	0.043	0.564	0.328	0.276	0.250	0.107	0.034	0.392
34	0.041	0.530	0.318	0.268	0.243	0.107	0.059	0.502

35	0.030	0.491	0.323	0.272	0.247	0.107	0.047	0.307
36	0.027	0.600	0.317	0.267	0.242	0.107	0.063	0.190
37	0.036	0.601	0.328	0.277	0.251	0.119	0.020	0.793
38	0.041	0.338	0.396	0.352	0.132	0.068	0.050	0.107
39	0.052	0.205	0.409	0.363	0.136	0.072	0.022	0.300
40	0.066	0.170	0.376	0.335	0.125	0.068	0.094	0.083
41	0.084	0.148	0.325	0.289	0.108	0.241	0.034	0.254
42	0.089	0.123	0.311	0.277	0.104	0.247	0.065	0.132
43	0.103	0.088	0.289	0.256	0.096	0.241	0.116	0.046
44	0.094	0.109	0.323	0.287	0.108	0.248	0.039	0.171
45	0.067	0.151	0.406	0.361	0.135	0.043	0.053	0.153
46	0.085	0.153	0.422	0.375	0.141	0.051	0.018	0.373
47	0.098	0.110	0.402	0.358	0.134	0.043	0.061	0.115
48	0.120	0.089	0.321	0.293	0.084	0.226	0.073	0.111
49	0.122	0.081	0.273	0.471	0.083	0.088	0.082	0.106
50	0.059	0.128	0.278	0.480	0.084	0.091	0.063	0.101
51	0.040	0.218	0.283	0.488	0.086	0.095	0.044	0.150
52	0.039	0.189	0.292	0.504	0.088	0.098	0.016	0.359
53	0.044	0.247	0.300	0.308	0.162	0.188	0.036	0.261
54	0.044	0.207	0.296	0.303	0.159	0.195	0.047	0.169
55	0.038	0.244	0.305	0.313	0.164	0.188	0.022	0.290
56	0.032	0.350	0.300	0.308	0.162	0.195	0.036	0.233
57	0.035	0.475	0.335	0.344	0.180	0.115	0.020	0.466
58	0.043	0.468	0.338	0.347	0.182	0.117	0.012	0.725
59	0.046	0.428	0.313	0.321	0.169	0.115	0.076	0.085
60	0.031	0.730	0.319	0.327	0.172	0.139	0.037	0.296
61	0.044	1.000	0.307	0.315	0.166	0.171	0.034	0.782
62	0.051	0.950	0.282	0.290	0.152	0.172	0.098	0.487
63	0.035	0.814	0.292	0.300	0.157	0.215	0.029	0.243
64	0.059	0.905	0.294	0.301	0.158	0.183	0.057	0.798
65	0.047	0.545	0.341	0.350	0.184	0.102	0.017	0.767
66	0.060	0.595	0.325	0.333	0.175	0.107	0.059	0.088
67	0.076	0.655	0.307	0.315	0.165	0.158	0.048	0.639
68	0.058	0.525	0.283	0.290	0.152	0.168	0.110	0.254
69	0.041	0.420	0.330	0.339	0.178	0.116	0.031	0.772
70	0.033	0.412	0.306	0.314	0.165	0.120	0.093	0.106
71	0.037	0.476	0.325	0.333	0.175	0.116	0.044	0.341
72	0.029	0.491	0.336	0.344	0.181	0.122	0.017	0.751

73	0.039	0.574	0.269	0.276	0.145	0.229	0.074	0.397
74	0.038	0.431	0.317	0.325	0.170	0.138	0.044	0.359
75	0.039	0.386	0.325	0.334	0.175	0.140	0.022	0.735
76	0.053	0.376	0.315	0.323	0.169	0.138	0.049	0.365
77	0.063	0.344	0.284	0.292	0.153	0.220	0.045	0.659
78	0.046	0.207	0.322	0.330	0.173	0.135	0.034	0.221
79	0.040	0.209	0.316	0.324	0.170	0.142	0.049	0.122
80	0.051	0.191	0.307	0.315	0.165	0.169	0.038	0.233
81	0.058	0.173	0.266	0.273	0.143	0.237	0.074	0.106
82	0.065	0.138	0.278	0.285	0.150	0.240	0.044	0.124
83	0.084	0.107	0.267	0.274	0.144	0.237	0.071	0.074
84	0.088	0.097	0.476	0.209	0.036	0.190	0.066	0.085
85	0.080	0.120	0.426	0.187	0.032	0.195	0.142	0.042
86	0.107	0.155	0.500	0.220	0.038	0.190	0.029	0.270
87	0.139	0.117	0.419	0.184	0.032	0.230	0.113	0.079
88	0.149	0.080	0.332	0.146	0.025	0.279	0.086	0.106
89	0.151	0.067	0.430	0.189	0.033	0.230	0.096	0.063
90	0.148	0.080	0.512	0.050	0.062	0.224	0.133	0.037
91	0.145	0.089	0.371	0.163	0.117	0.219	0.118	0.095
92	0.139	0.077	0.350	0.154	0.111	0.226	0.155	0.053
93	0.079	0.080	0.391	0.171	0.123	0.160	0.142	0.037
94	0.047	0.128	0.451	0.198	0.142	0.169	0.037	0.122
95	0.037	0.266	0.445	0.195	0.141	0.160	0.047	0.222
96	0.037	0.432	0.366	0.334	0.095	0.157	0.027	0.656
97	0.043	0.474	0.359	0.328	0.094	0.167	0.042	0.534
98	0.031	0.419	0.363	0.332	0.095	0.157	0.033	0.402
99	0.033	0.447	0.399	0.364	0.104	0.077	0.035	0.175
100	0.056	0.450	0.311	0.284	0.081	0.165	0.139	0.272
101	0.024	0.327	0.392	0.358	0.102	0.091	0.037	0.189
102	0.036	0.429	0.382	0.348	0.100	0.119	0.031	0.407
103	0.033	0.369	0.403	0.368	0.105	0.072	0.031	0.232
104	0.034	0.497	0.400	0.365	0.104	0.075	0.034	0.454
105	0.038	0.350	0.363	0.332	0.095	0.110	0.080	0.153
106	0.028	0.439	0.384	0.351	0.100	0.116	0.035	0.309
107	0.034	0.732	0.385	0.352	0.103	0.110	0.035	0.359
108	0.053	1.000	0.379	0.346	0.099	0.103	0.054	0.513
109	0.059	1.000	0.356	0.325	0.093	0.111	0.103	0.138
110	0.041	0.705	0.380	0.347	0.099	0.103	0.052	0.915

111	0.023	0.525	0.382	0.349	0.100	0.065	0.083	0.159
112	0.028	0.759	0.408	0.372	0.106	0.067	0.029	0.042
113	0.044	0.748	0.393	0.359	0.103	0.065	0.059	0.447
114	0.072	0.725	0.334	0.305	0.087	0.148	0.104	0.493
115	0.082	0.353	0.371	0.339	0.097	0.116	0.057	0.381
116	0.061	0.370	0.357	0.326	0.093	0.124	0.088	0.169
117	0.062	0.640	0.337	0.307	0.088	0.137	0.110	0.402
118	0.050	0.694	0.365	0.334	0.095	0.112	0.073	0.381
119	0.057	0.889	0.333	0.304	0.087	0.175	0.081	0.307
120	0.074	0.947	0.337	0.308	0.088	0.178	0.071	0.471
121	0.083	0.695	0.310	0.283	0.081	0.175	0.130	0.444
122	0.060	0.435	0.337	0.308	0.088	0.174	0.074	0.196
123	0.059	0.466	0.354	0.323	0.092	0.183	0.036	0.348
124	0.075	0.465	0.380	0.347	0.099	0.107	0.047	0.513
125	0.076	0.428	0.382	0.349	0.100	0.111	0.042	0.640
126	0.091	0.489	0.355	0.324	0.093	0.107	0.101	0.185
127	0.104	0.468	0.358	0.327	0.093	0.109	0.094	0.381
128	0.089	0.367	0.339	0.310	0.088	0.107	0.135	0.240
129	0.056	0.325	0.392	0.358	0.102	0.094	0.034	0.185
130	0.064	0.393	0.365	0.333	0.095	0.096	0.093	0.074
131	0.070	0.348	0.335	0.306	0.087	0.121	0.130	0.201
132	0.046	0.274	0.403	0.368	0.105	0.054	0.049	0.323
133	0.062	0.444	0.409	0.373	0.107	0.061	0.036	0.127
134	0.072	0.458	0.397	0.363	0.104	0.074	0.042	0.497
135	0.068	0.333	0.386	0.352	0.101	0.077	0.064	0.285
136	0.058	0.299	0.396	0.362	0.103	0.082	0.041	0.285
137	0.046	0.353	0.407	0.372	0.106	0.077	0.017	0.619
138	0.048	0.439	0.378	0.345	0.099	0.080	0.081	0.185
139	0.062	0.476	0.406	0.371	0.106	0.077	0.020	0.799
140	0.089	0.434	0.310	0.283	0.081	0.211	0.093	0.336
141	0.062	0.357	0.391	0.357	0.102	0.075	0.054	0.148
142	0.072	0.362	0.363	0.331	0.095	0.072	0.118	0.238
143	0.046	0.280	0.411	0.376	0.107	0.044	0.041	0.155
144	0.049	0.257	0.415	0.379	0.108	0.052	0.033	0.134
145	0.075	0.503	0.349	0.319	0.091	0.158	0.061	0.475
146	0.077	0.472	0.365	0.333	0.095	0.164	0.027	0.778
147	0.071	0.425	0.349	0.319	0.091	0.158	0.061	0.475
148	0.069	0.440	0.326	0.298	0.085	0.164	0.112	0.226

149	0.061	0.431	0.349	0.319	0.091	0.158	0.061	0.444
150	0.043	0.365	0.667	0.068	0.000	0.188	0.074	0.280
151	0.046	0.372	0.651	0.066	0.009	0.186	0.094	0.111
152	0.037	0.367	0.694	0.070	0.000	0.192	0.040	0.470
153	0.036	0.382	0.697	0.078	0.008	0.196	0.040	0.228
154	0.049	0.417	0.628	0.064	0.000	0.249	0.056	0.407
155	0.052	0.384	0.582	0.059	0.006	0.242	0.112	0.058
156	0.054	0.359	0.655	0.066	0.000	0.253	0.022	0.741
157	0.061	0.386	0.589	0.060	0.001	0.243	0.104	0.057
158	0.069	0.432	0.609	0.062	0.000	0.261	0.064	0.407
159	0.078	0.383	0.608	0.062	0.001	0.220	0.106	0.048
160	0.063	0.316	0.656	0.066	0.000	0.227	0.047	0.481
161	0.066	0.421	0.639	0.065	0.005	0.224	0.069	0.270

Table C.2: Initial and final set of properties used in static numerical simulations in Well **Γ**.

	Initial Guess						**Final Parameters**	
Layer number	ϕ_{ICON} **[frac.]**	Sw_{irr} **[frac.]**	**Calcite [frac.]**	**Dolomite [frac.]**	**Quartz [frac.]**	**Clay + Anhydrate [frac.]**	ϕ_{ICON} **[frac.]**	Sw_{irr} **[frac.]**
1	0.090	0.262	0.624	0.023	0.076	0.123	0.110	0.256
2	0.068	0.217	0.817	0.000	0.008	0.008	0.049	0.201
3	0.117	0.315	0.455	0.077	0.000	0.168	0.120	0.251
4	0.107	0.322	0.828	0.000	0.005	0.044	0.102	0.251
5	0.092	0.333	0.825	0.001	0.000	0.043	0.104	0.251
6	0.125	0.356	0.647	0.052	0.112	0.052	0.128	0.252
7	0.114	0.355	0.729	0.027	0.061	0.053	0.122	0.252
8	0.103	0.334	0.719	0.044	0.044	0.070	0.115	0.173
9	0.114	0.356	0.769	0.043	0.026	0.026	0.127	0.253
10	0.109	0.339	0.796	0.044	0.027	0.018	0.107	0.252
11	0.125	0.343	0.214	0.214	0.214	0.214	0.134	0.163
12	0.091	0.271	0.225	0.225	0.225	0.225	0.091	0.259
13	0.077	0.202	0.226	0.226	0.226	0.226	0.086	0.257
14	0.081	0.192	0.228	0.228	0.228	0.228	0.079	0.256

Table C.3: Initial and final set of properties used in static numerical simulations in Well **X**.

Nomenclature

a	:	Winsauer's factor in Archie's equation, []
AO10	:	Array induction 1-foot resistivity, [Ω.m]
AO30	:	Array induction 1-foot resistivity, [Ω.m]
AO30_Simul.	:	Simulated array induction 1-foot resistivity, [Ω.m]
AO60	:	Array induction 1-foot resistivity, [Ω.m]
AO90	:	Array induction 1-foot resistivity, [Ω.m]
AO90_Simul.	:	Simulated array induction 1-foot resistivity, [Ω.m]
BF_{cutoff}	:	Theoretical *T2* cutoff that separates bound fluid and clay fluid, [ms]
BF_T	:	Portion of the rock related to total bound fluid, [%]
Cal	:	Diameter of the borehole, [in]
D	:	Effective fluid diffusivity coefficient, [cm^2/s];
DTC	:	Compressional sonic slowness, [μs/ft]
e_{nw}	:	Experimental exponent for k_{rnw} equation, []
e_p	:	Pore-size distribution exponent, []
e_w	:	Experimental exponent for k_{rw} equation, []
FF	:	Portion of the rock related to free fluid, [frac.]
FF_{cutoff}	:	Theoretical *T2* cutoff that separates free fluid and bound fluid, [ms]
FV_{Ri}	:	Fractional pore volume of the homogeneous rock, [frac.]
G	:	Static magnetic field gradient, [G/cm]
GR	:	Natural gamma-ray, [GAPI]
GR_{final}	:	Natural gamma-ray measured in the final phase, [GAPI]
GR_{int}	:	Natural gamma-ray measured in the intermediate phase, [GAPI]
GR_*Simul.*	:	Simulated natural gamma-ray, [GAPI]

HI	:	Hydrogen index, []
k	:	Permeability, [mD]
k_{CORE}	:	Permeability of core samples measured in laboratory, [mD]
k_{Dyn}	:	Estimated permeability in dynamic simulations, [mD]
k_{est}	:	Estimated permeability, [mD]
k_{Gauss}	:	Permeability estimated with Gaussians, [mD]
k_{GM}	:	Geometric mean permeability, [mD]
k_{PLUG}	:	Permeability of plugs measured in the laboratory, [mD]
k_{Ri}	:	Permeability of each homogeneous sample, [mD]
k_{rnw}	:	Non-wetting phase relative permeability, []
k_{rw}	:	Wetting-phase relative permeability, []
$k_{Tim\text{-}Coat}$	:	Permeability estimated with Timur-Coates' equation, [mD]
$k_{Tim\text{-}Tix}$	:	Permeability estimated with Timur-Tixier's equation, [mD]
m	:	Archie's porosity exponent, []
M2R1	:	Array induction 2-feet resistivity, [Ω.m]
M2R1_Simul.	:	Simulated array induction 2-feet resistivity, [Ω.m]
M2R2	:	Array induction 2-feet resistivity, [Ω.m]
M2R2_Simul.	:	Simulated array induction 2-feet resistivity, [Ω.m]
M2R3	:	Array induction 2-feet resistivity, [Ω.m]
M2R6	:	Array induction 2-feet resistivity, [Ω.m]
M2R6_Simul.	:	Simulated array induction 2-feet resistivity, [Ω.m]
M2R9	:	Array induction 2-feet resistivity, [Ω.m]
M2RX	:	Array induction 2-feet resistivity, [Ω.m]
M2RX_Simul.	:	Simulated array induction 2-feet resistivity, [Ω.m]
n	:	Archie's saturation exponent, []

$NPHI_{SS}$	:	Neutron porosity in sandstone units [psi]
$NPHI_{SS}\_Simul.$	:	Simulated neutron porosity in sandstone units [psi]
$p(x)$	:	Probability density function of a variable x []
p_W	:	Probability density function of the wetting phase []
p_{NW}	:	Probability density function of the non-wetting phase []
PEF	:	Photoelectric factor, [b/e-]
$PEF\_Simul.$	:	Simulated photoelectric factor, [b/e-]
P_c^0	:	Coefficient for P_c equation, [psi.darcy$^{1/2}$]
r	:	Pore radius, [μm]
$RHOB$	:	Bulk density, [g/cm^3]
$RHOB\_Simul.$	:	Simulated bulk density, [g/cm^3]
RQI	:	Reservoir quality index, []
RT	:	Rock type, []
R_T	:	True formation resistivity, [Ω.m]
R_{T_Archie}	:	Resistivity calculated with Archie's equation, [Ω.m]
S	:	Fluid saturation, [frac.]
So_r	:	Residual oil saturation, [frac.]
Sw	:	Connate water saturation, [frac.]
Sw_{Archie}	:	Water saturation calculated with Archie's equation, [frac.]
Sw_{irr}	:	Irreducible water saturation, [frac.]
Sw_{NMR}	:	Connate water saturation estimated from the NMR log, [frac.]
Sw_{-plug}	:	Water saturation measured in the laboratory, [frac.]
Sw_T	:	Total water saturation, [frac.]
$Sw_{T\_INITIAL}$	:	Initial total water saturation in the system, [frac.]
S/V	:	Surface-to-volume ratio of the pore [μm^{-1}]

$T1$	:	Longitudinal relaxation time, [ms]
$T1_B$	:	Bulk longitudinal relaxation time, [ms]
$T2$	:	Transverse relaxation time, [ms]
$T2_B$	:	Bulk transverse relaxation time, [ms]
$T2Dist$	:	NMR $T2$ distribution, [ms]
$T2Dis\_Simul.$	:	Simulated NMR $T2$ distribution, [ms]
TE	:	Inter-echo time, [ms]
γ	:	Gyromagnetic ratio for a hydrogen proton, []
μ	:	Mean value of the log-Gaussian distribution, []
σ	:	Standard deviation of the log-Gaussian distribution, []
ϕ_{CORE}	:	Total porosity of cores measured in the laboratory, [frac.]
ϕ_E	:	NMR effective porosity, [frac.]
ϕ_{FF}	:	NMR free fluid porosity, [frac.]
ϕ_{ICON}	:	Interconnected porosity, [frac.]
ϕ_{PLUG}	:	Total porosity of plugs measured in the laboratory, [frac.]
ϕ_{Ri}	:	Porosity of each individual sample, [frac.]
ϕ_{SON}	:	Sonic porosity, [frac.]
ϕ_T	:	Total porosity, [frac.]
$\phi_{T\text{-}NMR}$	:	Total porosity estimated from the NMR log, [frac.]
ρ_1	:	Longitudinal surface relaxivity, [cm/s]
ρ_2	:	Transverse surface relaxivity, [cm/s]

Acronyms

cP	:	Centipoise
CPMG	:	Carr-Purcell-Meiboom-Gill
CSF	:	Common Stratigraphic Framework
DC	:	Direct Current
ECS	:	Elemental Capture Spectroscopy
GR	:	Gamma Ray Log
mD	:	Millidarcy
NMR	:	Nuclear Magnetic Resonance
OBM	:	Oil-Base Mud
PEF	:	Photoelectric Factor Log
ppm	:	Parts Per Million
STP	:	Standard Temperature and Pressure
XRD	:	X-Ray Diffraction Measurement

References

Aguilera, R., 2004, Integration of geology, petrophysics, and reservoir engineering for characterization of carbonate reservoirs through Pickett plots, *AAPG Bulletin*, v. 88, no. 4, pp. 433–446.

Amaefule, J. O., Altunbay, M., Tiab, D., Kersey, D. G., and Keelan, D. K., 1993, Enhanced reservoir description: using core and log data to identify hydraulic (flow) unit and predict permeability in uncored intervals/wells, *SPE Annual Technical Conference and Exhibition*, Houston, Texas, USA, October 3-6.

Archie, G. E., 1952, Classification of carbonate reservoir rocks and petrophysical considerations, *AAPG Bulletin*, v. 36, no. 2, pp. 278–298.

Babadagli, T., and Al-Salmi, S., 2002, Improvement of permeability prediction for carbonate reservoirs using well log data, *SPE Asia Pacific Oil and Gas Conference and Exhibition*, Melbourne, Australia, October 8-10.

Biehle, A. A., Crocker, C. M., 1987, Comparison of petrographic characteristics of selected carbonate rocks to their petrophysical log response - Smackover Formation (Upper Jurassic), *Gulf Coast Association of Geological Societies Transactions*, v. 37, pp. 25-34.

Brooks, R. H., Corey, A. J., 1964, Hydraulic properties of porous media, *Hydrology Papers*, Colorado State University, Fort Collins, Colorado, March.

Chombart, L. G., 1960, Well logs in carbonate reservoirs, *Geophysics*, v. 25, no. 4, pp. 779–853.

Coates, G. R., Miller, M., Gillen, M., and Henderson, C., 1991, The MRIL in Conoco 33-1: an investigation of new magnetic resonance imaging log, *SPWLA 32nd Annual Logging Symposium*, Midland, Texas, USA, June 16-29.

Dean, E. W., Stark, D. D., 1920, A convenient method for the determination of water in petroleum and other organic emulsions, *Journal of Industrial & Engineering Chemistry*, v. 12, no. 5, pp. 486-490.

Diniz-Ferreira, E. L., and Torres-Verdín, C., 2012, Improved estimation of pore connectivity and permeability in deepwater carbonates with the construction of multi-layer static and dynamic petrophysical models, *SPWLA 53rd Annual Logging Symposium*, Cartagena, Colombia, June 16-20.

Dunham, R. J., 1962, Classification of carbonate rocks according to depositional texture. In Ham, W. E. (ed.), Classification of carbonate rocks – a symposium, *AAPG Memoir*, pp. 108-121.

Gandhi, A., Torres-Verdín, C., Voss, B., Gros, F. S., and Gabulle, J., 2013, Correction of invasion effects on well logs in Camisea gas reservoirs, Peru, with the construction of static and dynamic multilayer petrophysical models, AAPG Bulletin, v. 97, no. 3, pp. 379-412.

Kenyon, W. E., Day, P. I., Straley, C., and Willemsen, J. F., 1988, A three-part study of NMR longitudinal relaxation properties of water-saturated sandstones, *SPE Formation Evaluation,* v. 3, no. 3, pp. 622-636.

Kenyon, W. E., 1997, Petrophysical principles of applications of NMR logging, *The Log Analyst,* v. 38, no. 2, pp. 21-43.

Leverett, M. C., 1941, Capillary behavior in porous solids, *Transactions of the AIME*, 142, pp. 159-172.

Lucia, F. J., 1999, Characterization of petrophysical flow units in carbonate reservoirs: discussion: *AAPG Bulletin*, v. 83, no. 7, pp. 1161-1163.

Lucia, F. J., 2007, Carbonate Reservoir Characterization: An Integrated Approach, 2nd ed., Springer, Berlin Heidelberg, New York, N.Y.

Mavko, G., and Mukerji, T., 1995, Seismic pore space compressibility and Gassmann's relation, *Geophysics*, v. 60, no. 6, p. 1743–1749.

Minh, C. C., and Sundararaman, P., 2011, Nuclear-magnetic resonance petrophysics in thin sand/shale laminations, *SPE Annual Technical Conference and Exhibition*, San Antonio, Texas, USA, September 24-27.

Olesen J. R., Dutta D., and Sundaram K .M., 2000, Carbonate reservoir evaluation with advanced well-log data, *AAPG International Conference and Exhibition*, Bali, Indonesia, October 15-18.

Pittman, E. D., 1992, Relationship of porosity and permeability to various parameters derived from mercury injection capillary pressure curves for sandstones, *AAPG Bulletin*, v. 76, no. 2, pp. 191- 198.

Timur, A., 1969, Pulsed nuclear magnetic resonance studies of porosity, movable fluid, and permeability of sandstones, *Journal of Petroleum Technology*, v. 21, no. 6, pp. 775-786.

Toumelin, E., Torres-Verdín, C., Sun, B., and Dunn, K. J., 2004, Numerical assessment of modern borehole NMR interpretation techniques, *SPE Annual Technical Conference and Exhibition*, Houston, Texas, USA, September 26-29.

Verwer, K., Eberli, G. P., and Weger, R. J., 2011, Effect of pore structure on electrical resistivity in carbonates, *AAPG Bulletin*, v. 95, no. 2, pp. 175-190.

Voss, B., Torres-Verdín, C., Gandhi, A., Alabi, G., and Lemkecher, M., 2009, Common Stratigraphic Framework to simulate well logs and to cross-validate static and dynamic petrophysical interpretations, *SPWLA 50th Annual Logging Symposium*, The Woodlands, Texas, USA, June 21-24.

Wright, V. P., 2012, Lacustrine carbonates in rift settings: the interaction of volcanic and microbial processes on carbonate deposition, *Geological Society*, London, Special Publications, v. 370.

Wyllie, M. R. J., Gregory, A. R., and Gardner, L. W., 1956, Elastic waves velocities in heterogeneous and porous media, *Geophysics*, v. 21, no. 1, pp. 41-70.

Vitae

Elton Luiz Diniz Ferreira was born on October 12, 1979, in Curitiba, Paraná, Brazil, as the oldest child of Bernadete Diniz Ferreira and Celso Luiz Diniz Ferreira. In 2006 he married Amanda Caroline Reichert. They have a daughter, Helena Diniz Ferreira.

He graduated from Colégio Tecnológico Industrial and graduated from Universidade Federal do Paraná, in Curitiba, in 2006, with a B.S. in Physics. In 2011 he entered the graduate program in the Department of Petroleum and Geosystems Engineering, where he studied under Dr. Carlos Torres-Verdín. During his time at The University of Texas at Austin he received the Osmar Abib Memorial Endowed Presidential Scholarship in Petroleum Engineering.

He worked as a Petrophysicist at Petrobras, in Rio de Janeiro, Brazil, from 2006 to 2014. Upon completion of his Master's degree, Elton will join ConocoPhillips, in Houston, to work in formation evaluation as a Senior Petrophysicist.

Permanent e-mail address: eltongeof@gmail.com

This thesis was typed by Elton Luiz Diniz Ferreira.